Impact of Retarded Spark Timing on Engine Combustion, Hydrocarbon Emissions, and Fast Catalyst Light-Off

by

Brian E. Hallgren

B.S., Mechanical Engineering
Binghamton University, 1998

S.M., Mechanical Engineering
Massachusetts Institute of Technology, 2000

Submitted to the Department of Mechanical Engineering in Partial Fulfillment of the Requirements for the Degree of

DOCTOR OF PHILOSOPHY

at the

MASSACHUSETTS INSTITUTE OF TECHNOLOGY

February 2005

Signature of Author .....
Department of Mechanical Engineering
October 18, 2004

Certified by .....
John B. Heywood
Professor of Mechanical Engineering
Thesis Supervisor

Accepted by .....
Lallit Anand
Chairman, Department Committee on Graduate Students

In memory of my father

Impact of Retarded Spark Timing on Engine Combustion, Hydrocarbon Emissions, and Fast Catalyst Light-off

by

Brian E. Hallgren

Submitted to the Department of Mechanical Engineering on
October 18, 2004 in partial fulfillment of the requirements
for the Degree of Doctor of Philosophy

ABSTRACT

An experimental study was performed to determine the effects of substantial spark retard on engine combustion, hydrocarbon (HC) emissions, feed gas enthalpy, and catalyst light-off. Engine experiments were conducted at cold engine conditions for various ignition timings and air/fuel ratios. Chemical and thermal energy of the exhaust gas was tracked from cylinder-exit to the catalytic converter inlet using a variety of experimental techniques. Time-resolved exhaust port and exhaust runner hydrocarbon concentrations were converted to an exhaust HC mass flow rate and compared to time-averaged downstream HC levels. Quenching experiments quantified cylinder-exit HC emissions by rapidly cooling exhaust gas at the valve seats, effectively freezing HC oxidation reactions.

Combustion stability was observed to decrease as the phasing of the 50% mass fraction burned location occurred later in the expansion stroke. A thermodynamic burn rate analysis indicated combustion was complete by exhaust valve opening with spark timings as late as 20° after top-dead-center (ATDC). Engine operation with a relative air/fuel ratio 10% lean of stoichiometric resulted in the lowest observed tailpipe-out HC emissions. Retarded spark timings increased exhaust system oxidation, with port HC oxidation ranging from 15% to 37% with additional HC reductions (40-50%) in the runner for ATDC spark timings. Catalyst light-off times were reduced by 5 seconds and cumulative catalytic converter-in HC emissions were reduced by 44% prior to light-off.

A phenomenological model of exhaust system oxidation was developed to provide insight into HC burn-up with late combustion phasing. A detailed chemical kinetic mechanism was coupled with an exhaust flow model and exhaust thermal model. The hydrocarbon tracking and exhaust gas quenching experiments provided initial conditions for a reacting plug flow model. The predicted exhaust HC reaction rates were found to be strongly coupled with exhaust gas temperature and the hydrocarbon species used to represent unburned fuel. The analysis showed that most of the oxidation occurred early in the exhaust period when gas temperatures exceeded 1300K.

Thesis Supervisor: John B. Heywood
Title: Professor of Mechanical Engineering

TABLE OF CONTENTS

LIST OF FIGURES

LIST OF TABLES

NOMENCLATURE

ABBREVIATIONS:

ABDC	after bottom-dead-center
A/F	air/fuel ratio
ATDC	after top-dead-center
BBDC	before bottom-dead-center
BDC	bottom-dead-center
BTDC	before top-dead-center
CA	crank angle
CMCP	charge motion control plate
COV	coefficient of variation
CVI	closed valve injection
DAQ	data acquisition
DOHC	dual overhead camshafts
ECM	engine control module
ECU	engine control unit
EGR	exhaust gas recirculation
EOC	end of combustion
EV	exhaust valve
EVC	exhaust valve closing
EVO	exhaust valve opening
FFID	fast flame ionization detector
FID	flame ionization detector
FNDIR	fast non-dispersive infrared
FTP	federal test procedure
HC	hydrocarbons
IAC	idle air control
IMEP	indicated mean effective pressure
MAP	manifold air pressure
MBT	maximum break torque
MDS	modular development system
MFB	mass fraction burned
NDIR	non-dispersive infrared
NO_x	oxides of nitrogen
OSC	oxygen storage capacity
PC	personal computer
PFI	port fuel injected
ppm_{C1}	parts per million - single carbon atom
PVC	positive crankcase ventilation
RPM	revolutions per minute
SI	spark-ignition
TDC	top-dead-center
UEGO	universal exhaust gas oxygen
ULEV	ultra-low-emission vehicle
WOT	wide open throttle

SYMBOLS:

Cd	discharge coefficient
Cp	specific heat at constant pressure
$\Delta\theta_{sp}$	relative spark timing modification
θ	crank angle
γ	ratio of specific heats
h_c	convective heat transfer coefficient
λ	relative air/fuel ratio
mol	mole
ms	millisecond
Nu	Nusselt number
Ω	ohm
Pd	Palladium
Pr	Prandtl number
Pt	Platinum
Re	Reynolds number
Rh	Rhodium
ρ	density
Sp	spark
wt	weight

CHAPTER 1

INTRODUCTION

1.1 OVERVIEW

1.1.1 BACKGROUND AND MOTIVATION

Use of catalytic converters for aftertreatment is an effective means of reducing tailpipe-out hydrocarbon (HC) emissions from spark-ignition engines (SI). However, a sizeable amount (70 - 90%) of the total hydrocarbon emissions during the Federal Test Procedure (FTP) cycle are emitted during the first several seconds of operation before the catalyst reaches light-off temperature (~300° C), Fig. 1.1. During a cold-start, fuel evaporation is poor and fuel enrichment is necessary to ensure a robust combustion event. Exhaust aftertreatment is not effective until light-off temperatures are achieved. Furthermore, light-off temperatures for aged catalysts can increase by 50° C [1]. Significant HC emissions reductions can be attained by reducing tailpipe-out hydrocarbons before catalyst activation and reducing the time required for light-off.

Numerous sources of hydrocarbon emissions exist for SI engines; mass trapped in crevice volumes, wall quenching during flame propagation, outgasing of HC from in-cylinder deposits and oil layer, and liquid wetting of in-cylinder surfaces. As the flame propagates outward from the ignition source, in-cylinder pressure rises increasing the mass fraction of unburned fuel trapped in crevice volumes. Boundary layers also form on the cylinder liner, piston top, and cylinder head due to heat transfer from the high temperature unburned mixture to the combustion chamber surfaces, quenching chemical reactions and leaving a thin layer of unburned reactants. During the expansion stroke, post-flame oxidation can consume hydrocarbons as crevice volumes and fuel trapped in deposits are released and mix with the high temperature burnt gases. Additional in-cylinder and exhaust system oxidation occurs as the bulk gases are expelled during the exhaust process.

Engine operation with aggressively retarded spark timings from maximum brake torque (MBT) timings has proven effective in achieving both of these requirements. Phasing the combustion process later in the expansion stroke decreases the amount of useful work extracted

from the burnt gases, resulting in higher exhaust gas temperatures and increased post-flame oxidation rates. Additionally, lower in-cylinder peak pressures reduce the mass of unburned mixture trapped in crevices that escape oxidation during flame propagation and exit as HC emissions. However, there are limitations to late combustion phasing; with substantial spark retard, flame propagation occurs in a rapidly expanding volume, increasing cycle-to-cycle variations and reducing engine efficiency. Excessively high exhaust gas temperatures, greater than 1050° C, can lead to thermal deactivation and degraded catalyst performance [2].

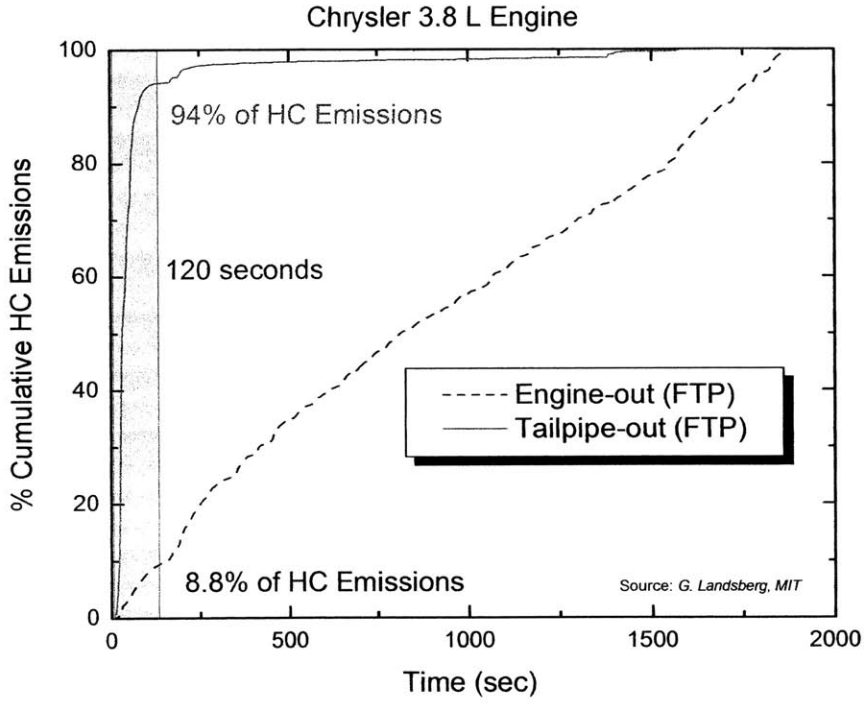

Figure 1.1 Cumulative engine-out and tailpipe-out HC emission over an FTP-75 for a six-cylinder SI engine.

1.1.2 PREVIOUS WORK

Post-flame hydrocarbon oxidation in the exhaust system of spark ignition engines has been the focus of previous research. Caton *et al.* [3] performed exhaust port temperature quenching experiments to determine the impact of relative air/fuel ratios, speed, load, spark advance, and compression ratio on HC oxidation. By rapidly cooling the exhaust gas close to the exhaust valve, hydrocarbon oxidation reactions were frozen and the resulting HC concentration was quantified. Exhaust port oxidation ranged from 2% to 70% depending upon exhaust gas

temperatures, port residence time, and oxygen concentration. Similar research by Russ *et al.* [4,5] quantified combustion and emission characteristics under cold engine conditions with retarded spark timings. The primary cause of cycle-to-cycle variations with late spark ignition was late combustion phasing, quantified by the location of the 50% mass fraction burned. With close to stoichiometric operation, flame quenching, misfires, and prior cycle effects were not observed [5].

1.2 RESEARCH OBJECTIVES

1.2.1 OVERVIEW

Exhaust system oxidation under cold engine conditions is not well understood. Limited experimental data exists that tracks the thermal and chemical energy from cylinder-exit to the first brick of the catalyst. The trade-off between cold start tailpipe-out HC emissions and heating of the catalyst is done empirically. Therefore, experiments were designed to quantify the effect of cold engine conditions on engine combustion, HC emissions, and catalyst light-off with late spark timing. The work described herein quantifies and provides additional insight into processes that occur with spark timings aggressively retarded from MBT. With increased interest in reducing HC emissions following startup, engine experiments focused on ambient (20° C) engine conditions. A variety of experimental techniques and equipment was utilized to quantify engine exhaust emission. Fast-response exhaust gas analyzers, exhaust gas quenching and secondary air injection experiments provided a detailed understanding of the thermal and chemical energy of the feed gas from cylinder-exit to the inlet of the catalytic converter.

1.2.2 EXPERIMENTAL

Numerous HC tracking experiments were conducted over a range of spark timings and relative air/fuel ratios under ambient engine conditions. Time-resolved and time-averaged HC measurements provided exhaust system HC flow rates at various exhaust locations. Likewise, quenching experiments injected carbon dioxide at the exit plane of the exhaust valves, rapidly cooling the exhaust gas and effectively freezing HC reaction rates. These experiments yielded valuable information regarding the extent of HC emissions exiting the cylinder with late combustion phasing. Additionally, secondary air injection into the exhaust system was also

explored. The engine was operated rich of stoichiometric and air was introduced into the exhaust system to promote oxidation. Exothermic reactions coupled with the increased mass flow rate of feed gas to the catalyst resulted in reduced converter-in HC emissions and increased enthalpy rates supplied to the catalyst. These experiments guided the modeling effort and were used to verify sub-models.

1.2.3 MODELING

The hydrocarbon oxidation in the engine exhaust system was modeled as a 1-D quasi-steady reacting flow. Engine experiments and various diagnostic tools provided exhaust gas thermodynamic properties and compositions. A phenomenologically based model of the HC oxidation and catalyst feed gas enthalpy was developed, providing an interpretive tool for assessing exhaust system behavior during engine warm-up period. The model was coupled with a heat transfer subroutine and a time-dependent reacting plug flow model with inputs from an engine cycle simulation and experimental results. The chemical kinetic mechanism was selected from literature and found to provide agreement when compared to the experiments. The model provided quantitative information on the extent of exhaust oxidation and the state of the feed gas supplied to the catalyst.

CHAPTER 2

EXPERIMENTAL APPARATUS AND PROCEDURES

2.1 SINGLE-CYLINDER ENGINE

2.1.1 ENGINE-DYNAMOMETER

Steady-state experiments were performed using a single-cylinder Ricardo Hydra MKIII spark ignition engine fitted with a modified Volvo B5254 head. The head was port fuel injected (PFI) with 4-valves and a pent-roof combustion chamber geometry. The engine crankshaft was coupled to a Eaton dynamometer (6000 series) with absorbing and motoring capability.

Table 2.1 Single-cylinder engine specifications.

Single Cylinder Engine Specifications	
Displacement Volume (cc)	487
Clearance Volume (cc)	54
Bore (mm)	83
Stroke (mm)	90
Connecting Rod (mm)	158
Wrist Pin Offset (mm)	1
Compression Ratio	10:1
Valve Train	4v DOHC
Valve Timing	IVO 0° BTDC | IVC 60° ABDC
	EVO 44° BBDC | EVC 8° ATDC

2.1.2 ENGINE CONTROL UNIT

Fuel injection and spark timing were controlled by a MoTeC M4 engine control unit (ECU). The system utilized speed-density tables allowing for precise control of fuel injector pulse width and coil discharge. A standalone personal computer linked to the ECU allowed for the real-time adjustment of spark timing and fueling.

2.1.3 CYLINDER PRESSURE MEASUREMENTS

The engine was equipped with an in-cylinder piezoelectric pressure transducer (Kistler 6125A) coupled to a charge amplifier (Kistler 5010B) yielding a voltage output. The transducers gain was statically calibrated at several pressures utilizing a dead weight tester. Referencing of in-

cylinder pressure was obtained by an absolute pressure transducer (Omega PX176 Series) located in the intake plenum. The acquired in-cylinder pressure data was averaged over 20° CA around bottom-dead-center (BDC) during the compression stroke and scaled to reflect an absolute pressure. Proper crank angle phasing and transducer linearity was checked periodically by motoring the engine at WOT and plotting cylinder pressure and cylinder volume on a log-log scale.

The pressure transducer was side mounted between the exhaust and intake valves. The transducer was found to have problems related to thermal shock (a phenomena caused by the deformation of the transducer diaphragm when heat transfer occurs from the flame front to the transducer face resulting in thermal strain). This resulted in erroneous measurements noted late in the expansion process and required the use of a flame arrestor over the exposed tip to decrease measurement error.

2.1.4 Intake Charge Motion Control Plate (CMCP)

Engine combustion stability was improved by use of an intake charge motion control plate (CMCP). The charge motion control plate (CMCP) was installed in the plane of the intake port, downstream of the fuel injector, Fig. 2.1. The asymmetrical CMCP reduced the port cross sectional area by approximately 67%, but did not impede the fuel spray targeting footprint of the injector. The plate increased the in-cylinder tumble torque moment by a factor of 4 compared to flow levels generated without the port area reduction [6]. The intake CMCP was found to have a negligible impact on in-cylinder swirl. Burning velocity was increased and the crank angle location of the spark retard ignition timing limit was extended.

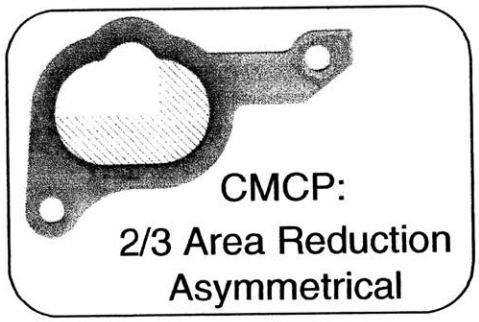

Figure 2.1 Intake charge motion control plate (CMCP) with 67% asymmetrical area reduction for the single cylinder engine.

2.1.5 DATA ACQUISITION SYSTEM

All signals were acquired using a National Instruments data acquisition (DAQ) board (PCI-6024E) capable of 8-channels of differential voltage input. The data acquisition system was triggered from an 1° incremental encoder coupled to the crankshaft. A superimposed 5-volt spike on the pressure data was used to mark BDC of the compression stroke. A dedicated PC running LabView software was used to create a virtual instrument (VI) for data scaling, processing, and logging. Post processing of data was carried out using custom scripts written in MatLab software.

2.1.6 EXPERIMENTAL CONDITIONS

The engine was operated at 1500 RPM and a net indicated mean effective pressure (Net-IMEP) of 3.0 bar. Spark timing and relative air/fuel ratio sweeps were performed under steady-state conditions with fixed fluid (coolant and oil) temperatures of 20°, 40°, and 90° C. The coolant temperature was that of the cylinder head and liner. The exhaust system was not externally cooled and was allowed to reach a hot stabilized temperature. All engine testing was conducted with reference gasoline, Indolene (UTG-96), Table 2.2.

2.1.7 HYDROCARBON EMISSIONS MEASUREMENTS

Hydrocarbon emissions were measured via a Cambustion HFR-400 fast-response flame ionization detector (FID) with a time response (10-90%) of approximately 1 millisecond. Heated transfer sample lines (TSL-H) with a hole diameter of 0.026" were located at the exit of the exhaust port and runner, at distances of 7 cm and 37 cm, respectively, from the exhaust valve seats, Fig. 2.2. The TSL-H had a transient time of approximately 3 milliseconds. The runner probe location was located at a distance similar to the catalytic converter inlet on a modern multi-cylinder engine. The fast-response FID instrument was setup as follows for all exhaust system investigations; heated line controller for the sampling probes (TSL-H): 180° C, fast FID sampling head temperature (HSM): 300° - 350° C, CP VAC: 100 mmHg, ΔP FID: 330 mmHg. The instrument was calibrated before and after each experiment using 1500 ppm_{C3} (4500ppm_{C1}) propane (C_3H_8) span gas and zeroed with nitrogen (N_2) gas.

Table 2.2 Indolene fuel properties (UTG-96) [7].

UTG-96

Property	Typical Value	Specification	Test Method
Copper Corrosion, 3 h at 50 °C	1	1 max	ASTM D 130
API Gravity at 60 °F	59.8	58.7 – 61.2	ASTM D 1250
Specific Gravity at 60/60 °F	0.740	0.734 – 0.744	ASTM D 4052
Oxidation Stability	1440+	1440 min	ASTM D 525
Carbon Density	2420	2401 – 2441	Calculated
Existent Gum, mg/100 mL	1.0	5 max	ASTM D 381
Lead Content, g/gal	0.001	0.05 max	ASTM D 3237 Modifie
Sulfur Content, wt %	0.005	0.1 max	ASTM D 3120
Phosphorus, g/gal	0.001	0.005 max	ASTM D 3231
Total Alcohol Content, vol %	0.00	0.00 max	EPA Procedure 10
Reid Vapor Pressure at 100 °F, psia	9.0	8.7 – 9.2	ASTM D 323
Research Octane Number	96.1	96.0 min	ASTM D 2699
Motor Octane Number	87.0		ASTM D 2700
Sensitivity	9.0	7.5 min	Calculated
Distillation Range at 760 mmHg, °F			ASTM D 86
Initial Boiling Point	91	75 – 95	
10%	128	120 – 135	
50%	220	200 – 230	
90%	309	300 – 325	
End Point	409	415 max	
Composition, vol %			ASTM D 1319
Olefins	5	10 max	
Aromatics	28	35 max	
Saturates	67	Remainder	
Heat of Combustion, Net, Btu/lb	18400		ASTM D 3338
Carbon Content, wt %	86.5		
Hydrogen Content, wt %	13.5		
Anti-Knock Index, (R+M)/2	92.0		Calculated

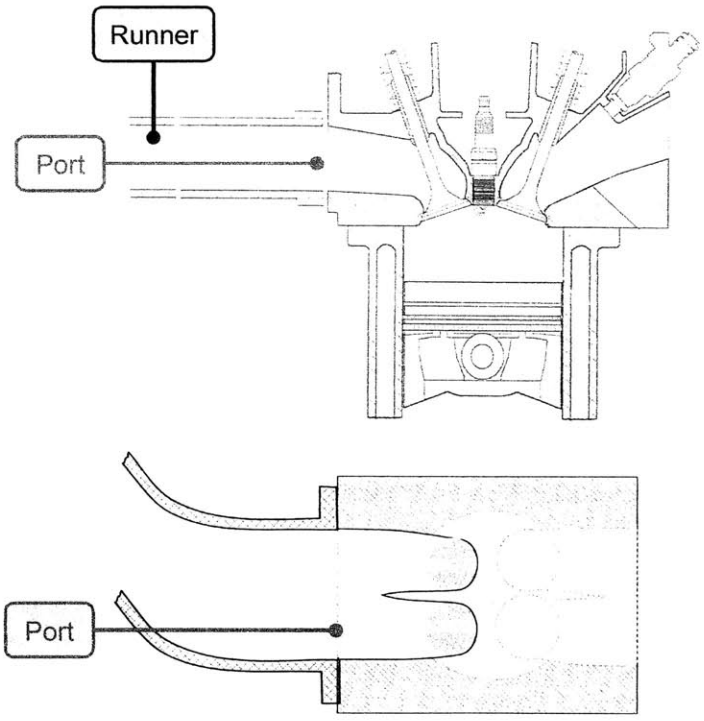

Figure 2.2 Fast-response HC analyzer probe sampling locations for single-cylinder experiments. Exhaust port and runner probes 7 cm and 37 cm from exhaust valves, respectively.

Time-averaged downstream HC emissions were sampled from a well-mixed, large volume, pulse-damping tank located 120 cm from the exhaust valves and quantified with a second FID (Rosemount Analytical Inc., Model 402) having a response time of several seconds. The FID was calibrated with 1500ppm$_{C3}$ (4500ppm$_{C1}$) propane and zeroed with nitrogen. The analyzer's oven temperature and heated sampling line were both set to 190° C to eliminate condensation before reaching the FID chamber.

2.1.8 Relative Air/Fuel Ratio

Exhaust gas relative air/fuel ratio was recorded using a universal exhaust gas oxygen (UEGO) sensor (Horiba MEXA-110) approximately 60 cm downstream from the exhaust valves. The Horiba UEGO had response time of approximately 100 ms and was calibrated in atmospheric air prior to engine testing.

2.1.9 Air and Fuel Mass Flow Rates

Intake air was measured by a Ricardo viscous flow meter (laminar flow element) equipped with a differential pressure transducer (Omega PX-176). The mass flow rate was then calculated from the volume flow rate based on ambient temperature and pressure. Fuel flow rates were obtained by flow testing the injector at various pulse widths and fuel rail pressures. Agreement within 2% was achieved between the UEGO measured air/fuel ratio and the calculated air/fuel ratio from fuel flow and air flow measurements.

2.1.10 Temperature Measurements

Time-averaged exhaust gas temperatures were measured with chromel-alumel (type-K) exposed junction thermocouples (0.8-mm bead diameter). The junctions were shielded with stainless steel sheaths to eliminate errors due to radiant heat transfer. The shielded thermocouples had a response time (10-90%) of approximately 1 second. Additional thermocouples were used to record exhaust system component temperatures, including the port manifold flange and runner outer walls. Temperatures of the fuel, coolant, oil, and inlet air were also monitored and recorded during engine testing.

2.1.11 EXHAUST GAS QUENCHING SETUP

An adaptor plate was installed between the exhaust manifold and cylinder head that allowed for the installation of four small tubes (outer diameter: 0.125", inner diameter 0.105") adjacent to the exit plane of the exhaust valves. A 35 mm section of jet holes (2 mm in diameter) discharged quench gas in a lateral flow field at the cylinder-exit plane, Fig. 2.3. Pulse flow control of quench gas was regulated by two solenoid valves triggered by an external control system. Upstream and downstream pressure and temperature histories were monitored and recorded by the DAQ system. High-pressure bottled gas injection ensured flow interruption did not occur during the exhaust blow down process. However, due to the required quench gas flow rate, an accumulator tank and heated gas regulators were needed to prevent icing, Fig. 2.4.

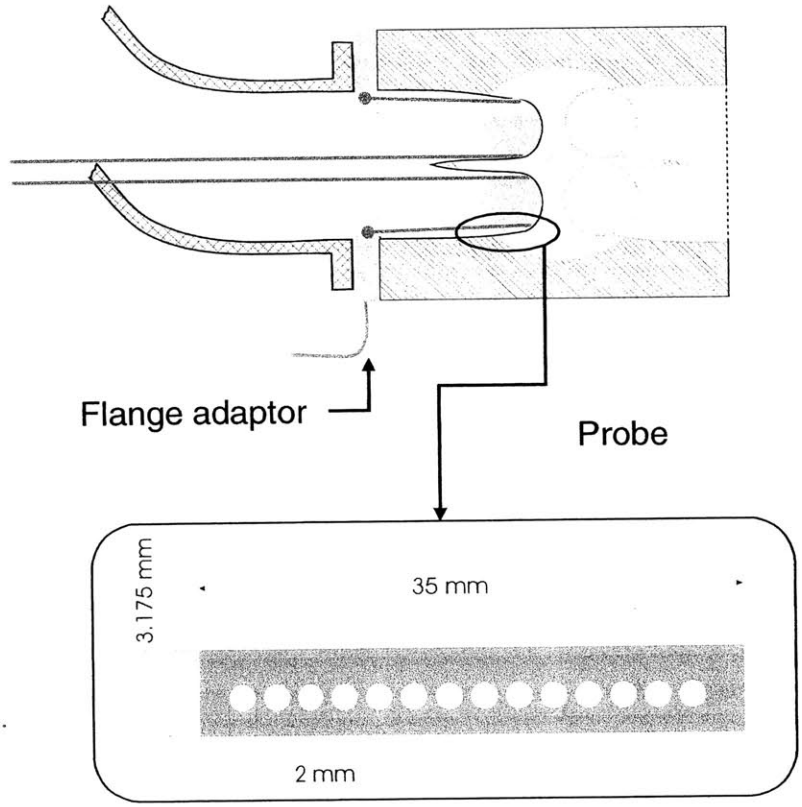

Figure 2.3 Schematic of probes located at the exhaust valve seats utilized for quenching and secondary air injection experiments.

During quenching experiments, carbon dioxide was utilized due to its high specific heat and ability to be quantified using an exhaust gas analyzer. Carbon dioxide (CO_2) levels in the exhaust were measured far down stream from the exhaust valves (120 cm) using a non-dispersive infrared (NDIR) detector (Rosemount 440). Water vapor was removed from the exhaust gas and the instrument was calibrated with 10% and 20% CO_2 and zeroed with nitrogen. However, subsequent dilution of the exhaust gas with nitrogen (N_2) was required to achieve readings within the CO_2 analyzer's range. The oxides of nitrogen (NO_x) were also monitored using a chemiluminnescence detector (Thermo Environmental Instruments Model 10A) and calibrated with 998ppm nitrogen oxide (NO) and nitrogen gas.

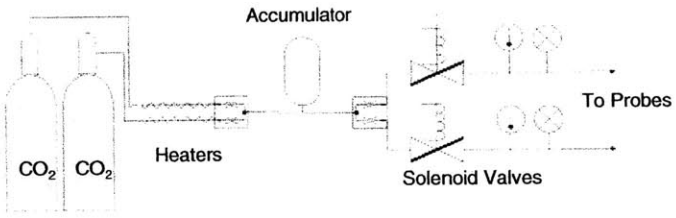

Figure 2.4 Overview of gas delivery system equipment used for quench gas and secondary air experiments.

2.1.12 Secondary Air Injection Setup

In order to investigate methods to increase feed gas sensible enthalpy and decrease converter-in HC emissions, experiments using the single-cylinder engine were conducted at fuel rich engine air/fuel ratios with secondary air injected at the exhaust valve seats. The same experimental setup outlined in Sec. 2.1.11 was used and CO_2 was replaced by compressed dry air.

2.2 Multi-Cylinder Engine

2.2.1 Engine-Dynamometer

A 2003 model year, 2.2 liter L61 Ecotec (GMX357) engine was chosen to investigate exhaust system oxidation during the first 20 seconds of operation following a cold-start. The engine was coupled to an eddy current, absorbing only, dynamometer (Froude Consine AE-80).

This test setup used the engine's starter motor for "crank" and "run" operation with full control over the engine control module (ECM). Additional engine details are given in Table 2.3.

2.2.2 EXHAUST SYSTEM OVERVIEW

The multi-cylinder engine's exhaust system consisted of a cast iron manifold, a three-way catalytic converter, muffler, and gate valve set to achieve a desired exhaust back pressure (350 kPa at WOT, 5600 RPM). The exhaust manifold and cylinder head were equipped with passages for secondary air operation, but this air system was not utilized in the experiments. Three catalysts were supplied with the engine; an inert catalyst (substrate only, no precious metals or oxygen storage capacity) and two active Ultra-Low-Emission Vehicle (ULEV) catalysts. The active catalysts were dyno-aged 100 hours to simulate 50,000 vehicle miles.

Each converter had a total volume of 82 cubic inches and was 4.2 inches in diameter with 600 cells per inch. The inert and active catalyst, XX9901JP, had a substrate wall thickness of 0.0043 inches, the other active catalyst, XX9901JQ, had a substrate thickness of 0.0035 inches. The active catalysts were composed of two bricks; the first was 2 inches in length and loaded with 3.5 grams of Palladium (Pd). The second brick was 4 inches in length and loaded with 1.5 grams of Platinum (Pt) and 0.31 grams of Rhodium (Rh). The second brick also contained a washcoat with oxygen storage capacity (OSC). The active catalyst XX9901JP was used to investigate light-off times for four different spark timing strategies. A thermocouple was embedded mid-brick and along the centerline of the catalyst and an additional thermocouple measured the catalyst shell temperature. Pre-catalyst and post-catalyst gas samples were acquired approximately 4.8 inches from the bricks.

2.2.3 ENGINE SUB-SYSTEMS AND INSTRUMENTATION

The engine coolant system was a closed looped system driven by an internal water pump that circulated fluid through the block and cylinder head. The thermostat was removed and the heater core was modified to eliminate the recirculation of coolant within the cylinder head and block. Coolant exited the head and flowed to an external water pump installed in the engine's cooling circuit. This allowed for maximum heat rejection rates when the engine was not in operation. The pump outlet was connected to an external head exchanger and to a coolant reservoir

tank before being routed back to the engine. Coolant temperature was varied via a setpoint controller that actuated a valve allowing for plant water to flow through an external heat exchanger. The engine's oil was not externally cooled and its temperature was measured in the oil pan.

Table 2.3 Multi-cylinder engine specifications.

Ecotec Engine Specifications	
Displacement Volume (cc)	2189
Firing Order	1-3-4-2
Clearance Volume (cc)	65
Bore (mm)	86
Stroke (mm)	94.6
Connecting Rod (mm)	146.5
Wrist Pin Offset (mm)	0.8
Compression Ratio	10:1
Valve Train	16v DOHC
Valve Timing	IVO 7° BTDC | IVC 56° ABDC
	EVO 68° BBDC | EVC 16° ATDC

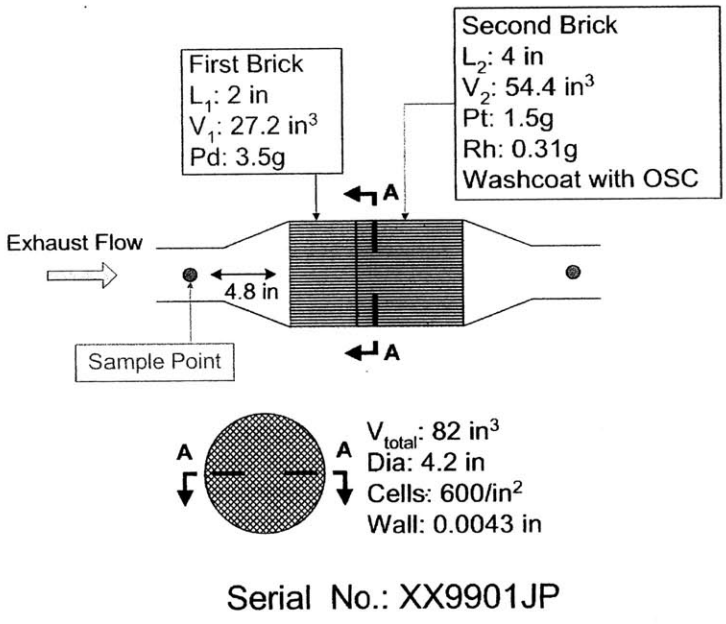

Figure 2.5 Active three-way catalyst (serial no: XX901JP) specifications.

The engine was operated with the positive crankcase ventilation (PCV) system in place and did not use an external exhaust gas recirculation (EGR) system. The engine had a returnless fuel injection system which required a constant fuel rail pressure of 52 psig. Fuel was supplied by external fuel pump with an inline filter, accumulator, and pressure regulator. The line return from the fuel regulator was directed through an external heat exchanger and back to the fuel tank. The regulator outlet was connected to the fuel injector rail. Fuel flow was estimated from the pulse width durations.

The intake system was modified to contain a damping tank and a thermal mass flowmeter (EPI, Series 8000 MP) to measure inducted air flow. Throttle position was varied using a stepper motor (Pacific Scientific SinMax 1.8° motor with 5230 indexer/driver) connected via a cable to the engine's throttle body. Incremental movement of the throttle was adjusted by two momentary contact switches with a selectable stepping rate.

Exhaust air/fuel ratio was monitored with a UEGO sensor (Horiba MEXA-700) located at the manifold collector. A pressure transducer (OMEGA PX-176) was installed in the intake plenum that provided better transient response compared to the OEM MAP transducer used for the ECM. All gas temperatures were measured with chromel-alumel (type-K), 0.8-mm exposed junction thermocouples with custom radiation shielding. Other thermocouples were installed throughout the engine setup to measure various fluid and metal temperatures.

2.2.4 Data Acquisition System

The data acquisition (DAQ) system utilized two DAQ boards from National Instruments installed in a personal computer. The first card (PCI-6071E) acquired 32 differential channels of high speed signals. The second card (PCI-6024E) was used with a multiplexing chassis (SCXI-1000) and a 32 channel thermocouple module (SCXI-1102) to capture temperature data from type-K thermocouples. The two boards were operated at different speeds; high speed data was captured once per engine crank angle degree, while temperature data was acquired once per engine revolution (at top-dead-center of cylinders no. 1 and no. 4). Both DAQ cards were triggered from signals provided by an incremental encoder (BEI Series H25E) coupled to the engine's crankshaft. A dedicated PC computer using LabView software was used to create a virtual instrument for data

scaling, processing, and logging. Post processing of data was carried out using custom MatLab scripts.

2.2.5 Modular Development System Hardware

The Delco Modular Development System (MDS) was used to control and modify the engine control module (ECM). Specific ECM operations were monitored and recorded by the MDS. This system provided the user control of parameters including the change of calibration data by read only memory (ROM) emulation. A PC was connected to the MDS stack that allowed for internal and external data logging. The stack was composed of several units. The main instrument unit (MIU) was the core of the MDS system and contained two main processors. The computer interface buffer internal logging (CIBIL) provided MDS communication with a computer. The analog conversion module (ACM) contained 8-BNC outputs and 2 instantaneous switches scaled from 0 to 5 volts. A 1MB GMPX Pod was connected to the X-pod that interfaced with the ECM and allowed the ECM's EPROM to be flashed for standalone ECM operation. The shell program allowed the user to have full access to lookup tables and relevant environmental variables. Real-time monitoring and modification of several parameters (RPM, MAP, spark timing, air/fuel ratio, idle air control (IAC) valve position) was accomplished by using the MDS's external display unit (DU).

2.2.6 Modular Development System Software

Full control of the engine was possible using the Delphi Electronics Instrument Tool Suite (ITS) running the Saturn Legacy Software. File handling between the computer and MDS unit was achieved using the ITS software. The program CalTools was used to modify ECM parameters and lookup table variables. For more detailed information regarding the MDS software refer to the Sec. B.1 in the Appendix.

2.2.7 In-cylinder Pressure Measurements

Each cylinder was fitted with an in-cylinder pressure transducer (Kistler 6125A). The cylinder head passage sleeve incorporated an eight-hole flame arrester to minimize the occurrence of thermal shock. The transducers were periodically cleaned of carbon deposits and re-calibrated

after 10-15 hours of service to minimize erroneous readings. Proper crank angle phasing and transducer linearity was checked periodically by disabling the cylinder's fuel injector and motoring the cylinder of interest, while firing the remaining three cylinders. Transducer calibration and pressure referencing was conducted as outlined in Sec. 2.1.3.

2.2.8 Engine Test Conditions and Procedure

Vehicle data provided by General Motors indicated that during the park idle period of the FTP test (0-15 seconds), the baseline calibration produced a Gross-IMEP of 3.0 bar and 1000 RPM (0.40-0.45 bar MAP and 6° BTDC spark timing). Therefore, the target load and speed for all experiments with the multi-cylinder engine was 2.3 bar Net-IMEP and 1000 RPM.

All engine tests were conducted with Indolene (Table 2.2) at approximately 20° C conditions. Engine speed and load were not regulated by the dynamometer controller (Digalog Series 1022A) due to the unstable transient control of the dyno-engine system during startup RPM flare. The required engine idle load was achieved by utilizing engine accessories with the dynamometer coupled but not absorbing power from the engine. A hydraulic power steering pump and alternator were added to the engine setup to simulate park idle load conditions observed during the first 15 seconds of the FTP test. The power steering pump was throttled to 800 psig by use of a needle valve. The low pressure line was routed through a heat exchanger before returning oil to the reservoir tank. The regulated 14.7 volt output from the alternator was isolated from the 12 volt battery bus by a zener diode and connected to bank of power watt resistors totaling 0.2 Ω (three 0.6 Ω resistors in parallel). After each engine startup test, metal temperatures throughout the engine and exhaust system were force cooled to ambient temperatures before another experiment was performed.

2.2.9 Fast-Response Emissions Analyzers

The fast-response FID was utilized to measure HC emissions in the exhaust port of cylinder no. 4 and at the inlet and outlet of the catalytic converter. The instrument was calibrated and setup according to the specifications outlined in Sec. 2.1.7.

In order to provide additional insight into exhaust system oxidation, a fast-response non-dispersive infrared (NDIR) detector (Cambustion NDIR-500) was used to evaluate exhaust gas CO

and CO_2 concentrations. The instrument used two independent sampling heads and heated probes; CO and CO_2 concentrations were simultaneously measured from one sample head. The NDIR-500's miniaturized sample chamber operated at sub-atmospheric pressure. Sample gas from the engine's exhaust system passed through narrow heated capillaries directly into the sample chamber where the gas was subjected to IR radiation. An IR detector was located below the emitter, with optical filters mounted on a chopping wheel that supplied a reference signal, Fig. 2.6. The system corrected for slight changes in temperature and IR emitter/detector signal strength. The optical windows of the emitter and detector were cleaned following 3 to 4 ambient starts. The fast-NDIR system had an overall response time (10-90%) of approximately 20 ms.

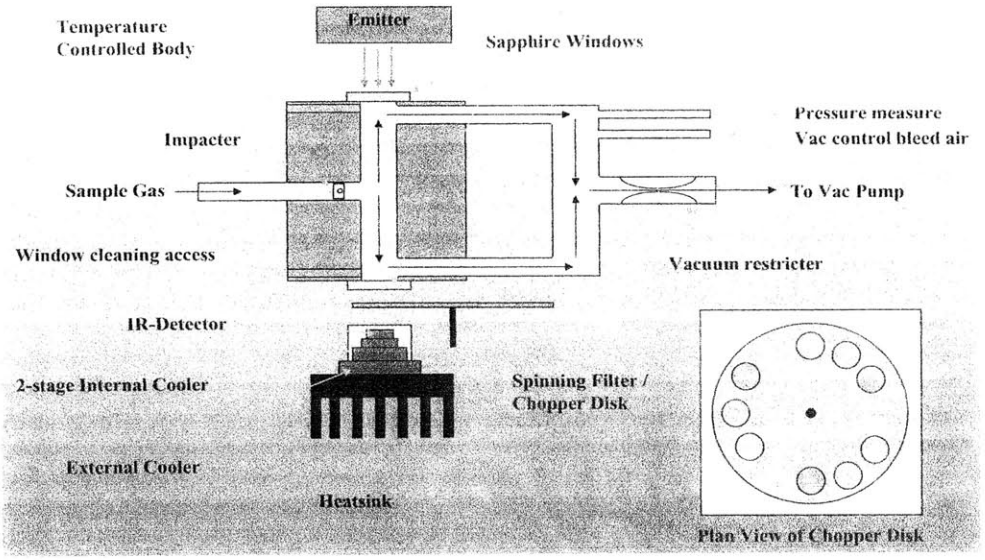

Figure 2.6 Schematic of fast-response NDIR sampling head from Cambustion [8].

CHAPTER 3

SINGLE-CYLINDER EXPERIMENTAL RESULTS

3.1 COMBUSTION CHARACTERISTICS

3.1.1 COMBUSTION STABILITY

As combustion was phased later in the cycle, spark retard was limited by combustion stability, quantified by the coefficient of variation (COV) in net indicated mean effective pressure (Net-IMEP). Cycle-to-cycle variations in the combustion process were caused by several factors: variations in relative air/fuel ratio around the spark plug, mixture motion variations, and residual gas fraction [16]. With aggressive spark retard, slower burning cycles result in a loss of efficiency as combustion occurred in a rapidly expanding volume. Figure 3.1 shows COV in the Net-IMEP as a function of various spark timings and relative air/fuel ratios with and without the charge motion control plate (CMCP) installed in the intake port.

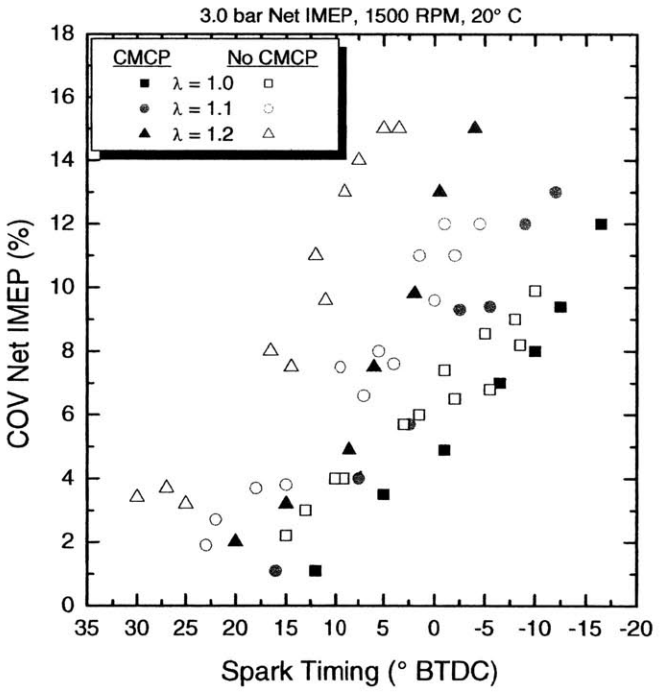

Figure 3.1 COV of Net-IMEP as a function of spark timing with and without intake charge motion control plate (CMCP) for three relative air/fuel ratios. Data shown for 3.0 bar Net-IMEP, 1500 RPM, and 20° C fluids.

The data shown in Fig. 3.1 was analyzed for 400 cycles with no recorded misfires or partial burns. Significant improvements in combustion stability were achieved for all stoichiometries with the use of the charge motion control plate. Typically, under fuel lean conditions, increased charge mixture variations and slower flame speeds worsen combustion stability. However, additional charge motion provided by the intake CMCP was observed to extend the misfire spark retard limit of the engine under lean, 20° C fluid conditions. A similar plate geometry was used by Takahashi *et al.* to alter charge motion with spark timing retardation based upon the combustion stability limit [22]. Combustion stability improved allowing for addition spark retarded further reducing HC emissions and increasing exhaust gas temperature. The CMCP was also thought to cause redistribution of liquid fuel in-cylinder. Liquid fuel has been shown to increase HC emissions by a factor of 3 to 7 per unit mass of fuel depending upon the location of liquid in-cylinder [23]. Enhanced in-cylinder motion has also been observed to increase post-flame oxidation transport rates [22].

3.1.2 Burn Rate Analysis Overview

A single-zone thermodynamic burn rate analysis incorporating the effects of residuals, heat transfer, and crevices was used to quantify combustion characteristics with late spark timings [9]. The burn rate analysis used a single zone energy model of the in-cylinder contents to determine the energy released from acquired in-cylinder pressure data, Eq. (3.1). The ratio of specific heats (γ) during the compression and expansion stroke was a linear function of temperature, equivalence ratio, and residual gas fraction. During combustion the ratio of specific heats was an averaged constant with 10° CA transition period at the start and end of combustion. Total crevice volume was estimated to be equal to 2% of the clearance volume. Heat transfer was handled by the Woschni correlation with the C1 coefficient equal to 1.7 and the gas expansion velocity constant, C2, fixed at 1.0. For more information on the Woschni correlation refer to the Sec. A.2 of the Appendix.

$$\frac{\partial Q_{Chemical}}{\partial \theta} = \frac{\gamma - 1}{\gamma} p \frac{\partial V}{\partial \theta} + \frac{1}{\gamma - 1} V \frac{\partial p}{\partial \theta} + \frac{\partial Q_{Crevice}}{\partial \theta} + \frac{\partial Q_{HT}}{\partial \theta} \tag{3.1}$$

where:

$Q_{Chemical}$	*fuel chemical energy*
θ	*crank angle*
γ	*ratio of specific heat*
p	*cylinder pressure*
V	*cylinder volume*
$Q_{Crevice}$	*energy in crevices*
Q_{HT}	*heat transfer*

In-cylinder pressure data, cumulative mass fraction burned (MFB), and instantaneous MFB data for three different spark timings (15°, -1°, and -16° BTDC) at 3.0 bar Net-IMEP, 1500 RPM, $\lambda = 1.0$, without charge motion (CMCP) and 20° C fluids for 15 consecutive cycles is shown in Fig. 3.2. Due to the occurrence of thermal shock observed in the pressure data, cumulative MFB profiles had an upward sloping tail noted after the end of the main flame propagation. As a result, the crank angle location at the end of combustion (EOC) was used as a reference point in reporting combustion phasing and combustion duration. The EOC point was determined when the instantaneous MFB rate fell below a threshold value (10^{-4} per crank angle). The location of EOC is noted in Fig. 3.2

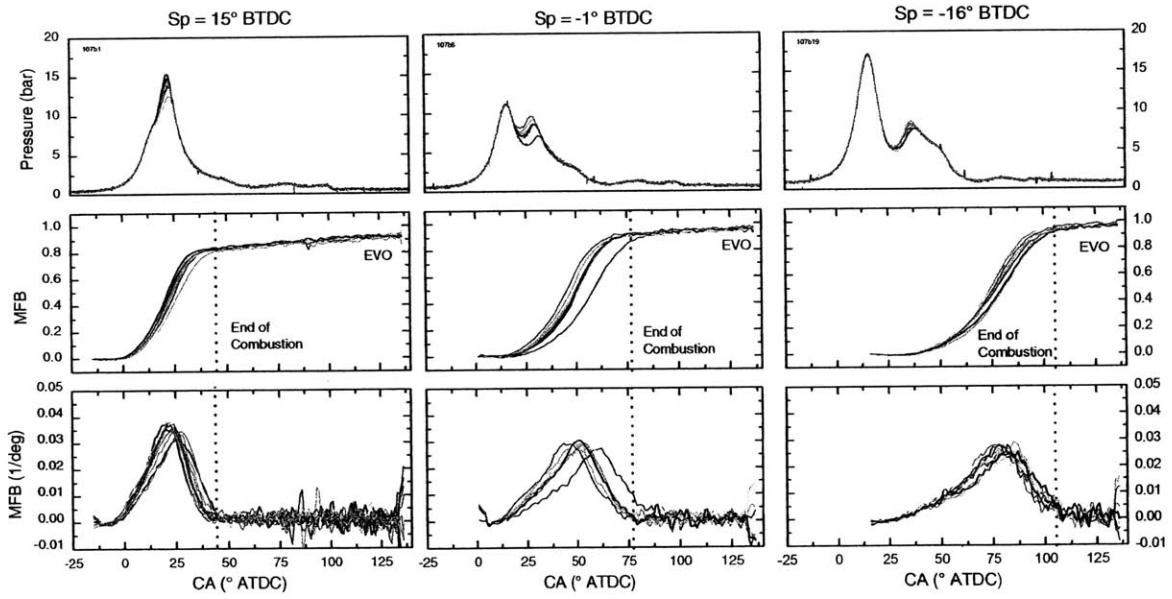

Figure 3.2 In-cylinder pressure, cumulative mass fraction burned (MFB) and instantaneous MFB rate as a function of crank angle for three spark timings. Operating conditions: 3.0 bar Net-IMEP, 1500 RPM, $\lambda = 1.0$, with charge motion (CMCP) and 20° C fluids.

3.1.3 COMBUSTION DURATION AND PHASING

The flame-development angle (0-10% energy-release fraction), rapid-burning angle (10-90% energy-release fraction), and location of the 50% energy-released fraction were investigated with and without the charge motion charge plate (CMCP) at various fluid temperatures, retarded spark timings, and stoichiometries, Figs. 3.3 - 3.6. Increased charge motion (CMCP) was found to decrease the crank angle location of the 50% MFB and shorten the 10-90% burn duration, as shown in Figs. 3.4 and 3.6, respectively. Under all test conditions, combustion was found to be complete before exhaust valve opening (EVO).

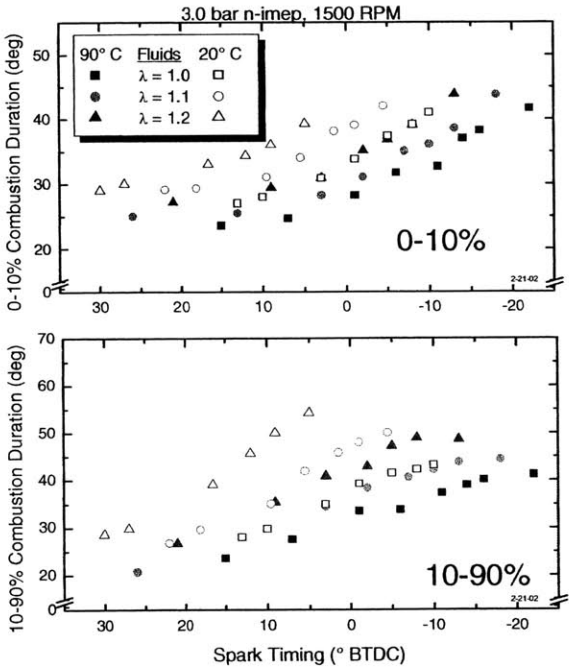

Figure 3.3 Combustion durations as a function of spark timing for different relative air/fuel ratios and fluid temperatures without charge motion control plate (CMCP) at 3.0 bar Net-IMEP and 1500 RPM.

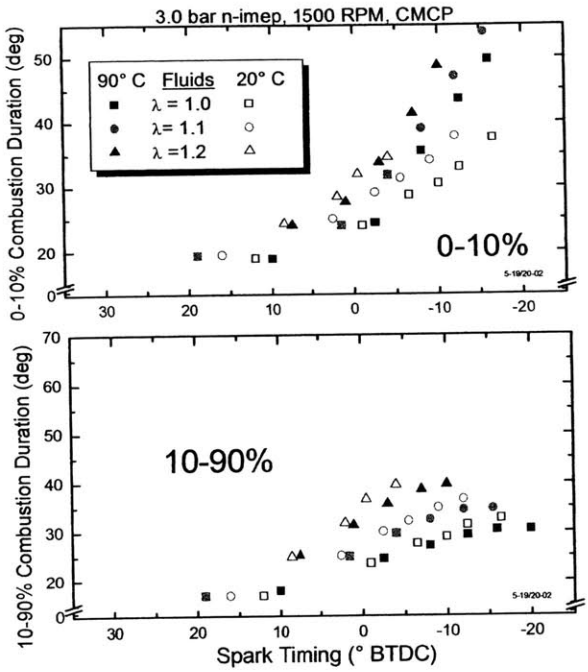

Figure 3.4 Combustion duration as a function of spark timing for different relative air/fuel ratios and fluid temperatures with charge motion control plate (CMCP) at 3.0 bar Net-IMEP and 1500 RPM.

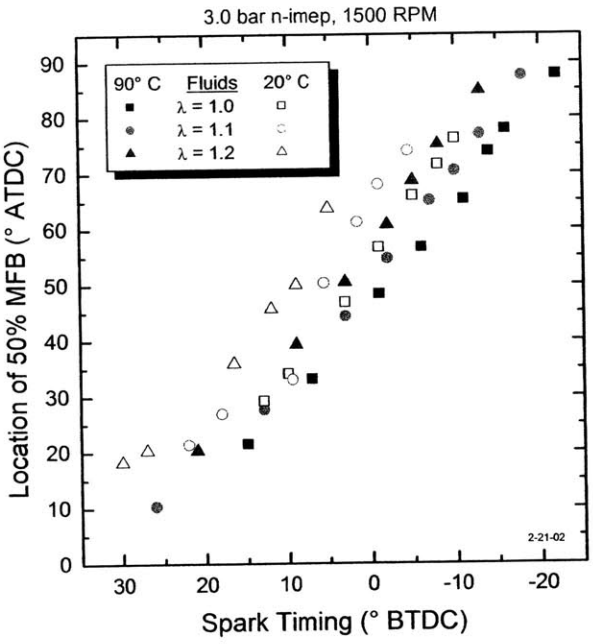

Figure 3.5 Location of 50% MFB as a function of spark timing without charge motion control plate (CMCP) for various relative air/fuel ratios and fluid temperatures at 3.0 bar Net-IMEP and 1500 RPM.

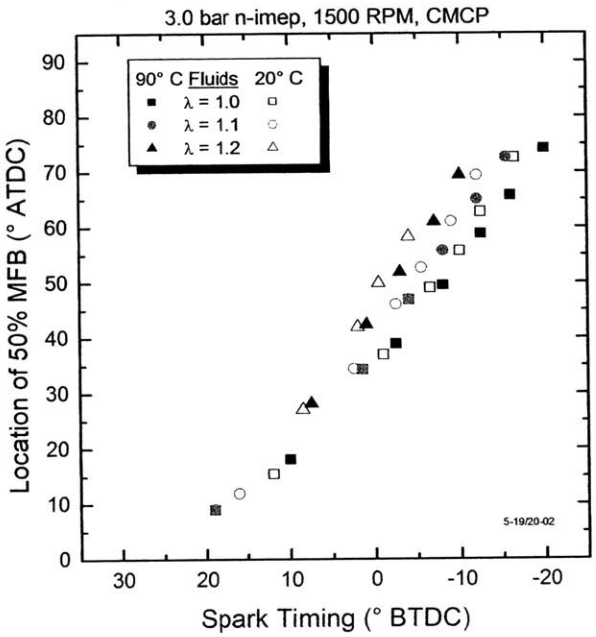

Figure 3.6 Location of 50% MFB as a function of spark timing with charge motion control plate (CMCP) for various relative air/fuel ratios and fluid temperatures at 3.0 bar Net-IMEP and 1500 RPM.

3.2 Exhaust Gas Temperatures

Exhaust gas temperatures were measured at port exit and compared to the 50% MFB location as shown in Fig. 3.7. Data was acquired for various relative air/fuel ratios with and without intake charge motion (CMCP) at 20° C fluids. Gas temperatures were observed to increase linearly with combustion phasing (location of 50% MFB). At an equivalent phasing, a stoichiometric air/fuel ratio had the highest burn gas temperature. In addition, the CMCP decreased gas temperature between 30-100K for an equivalent combustion phasing, which was attributed to the increased in-cylinder heat transfer during combustion.

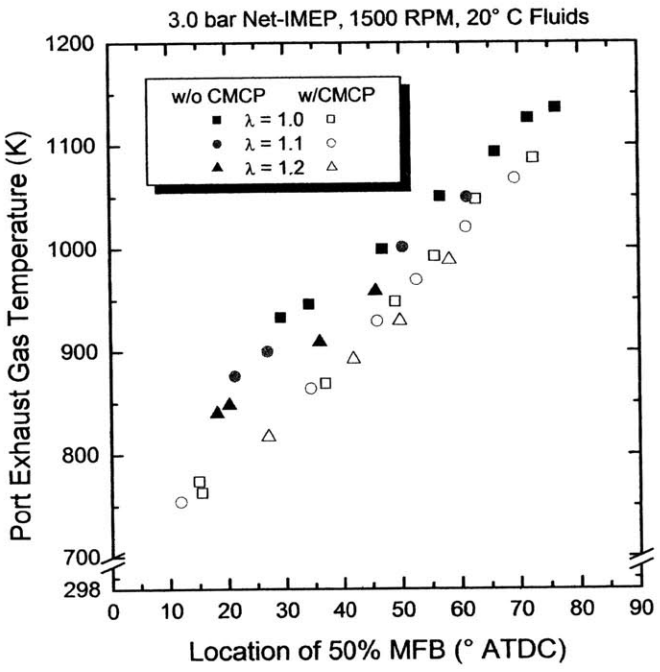

Figure 3.7 Thermocouple measured port exit exhaust gas temperature as a function of 50% MFB location for various relative air/fuel ratios with and without the charge motion control plate (CMCP) at 3.0 bar Net-IMEP, 1500 RPM, and 20° C fluids.

Feedgas sensible enthalpy rate (kJ/s) as a function of the coefficient of variation (COV) in the Net-IMEP was also investigated, Fig. 3.8. Tailpipe-out HC emissions can be dramatically reduced if the catalytic converter can reach light-off temperature faster following engine startup. Under stoichiometric engine operation and equivalent combustion stability (a COV in Net-IMEP of approximately 10%) the CMCP allowed for additional spark retard which increased the sensible enthalpy rate more than 60% (3 kJ/s to 5 kJ/s).

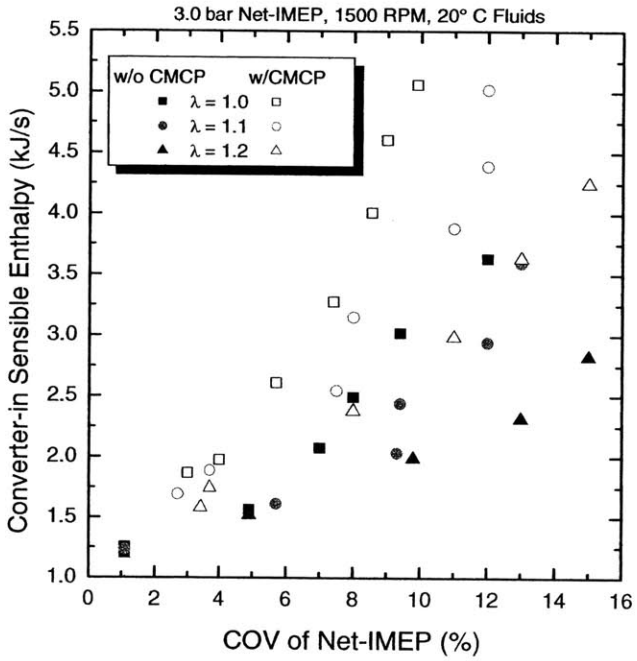

Figure 3.8 Converter-in sensible enthalpy rate as a function of COV of Net-IMEP for different relative air/fuel ratios with and without the charge motion control plate (CMCP).

3.3 Downstream Time-Averaged Hydrocarbon Emissions

To achieve the same engine load (Net-IMEP) with late spark timing, the engine's mass flow rate was increased to offset the reduced work extracted per cycle. Therefore, the meaningful representation of the HC emissions is the total engine-out hydrocarbon flow rate. Fig. 3.9 shows HC emissions with the CMCP and 20° C fluids. Engine-out HC levels were observed to reach a minimum for $\lambda = 1.0$ and $\lambda = 1.1$. Several mechanisms were responsible for the trends shown in Fig. 3.9. As spark was slewed from MBT to after-top center timings, rising burned gas temperatures increased the rate of post-flame hydrocarbon oxidation. Lower in-cylinder peak combustion pressures reduced the mass fraction of HC trapped in crevice volumes that escaped oxidation during flame propagation. However, over the range of spark timings tested, manifold air pressure (MAP) was varied from 0.3 bar to wide open throttle (WOT), in order to maintain constant Net-IMEP, changing the mass and temperature of trapped residual gases. As spark retard is increased, blowdown pressures and mass flow rates increase, resulting in reduced exhaust port

residence times. Higher intake port pressures diminish back-flow during the valve overlap period and impeded fuel vaporization with 20° C fluids. Mixture preparation was adversely affected and resulted in additional liquid fuel entering the cylinder, increasing HC emissions. Slightly lean of stoichiometric (λ = 1.1) resulted in the lowest observed HC mass flow rate, corresponding to exhaust conditions in which additional molecular oxygen was present while maintaining high burned gas temperatures.

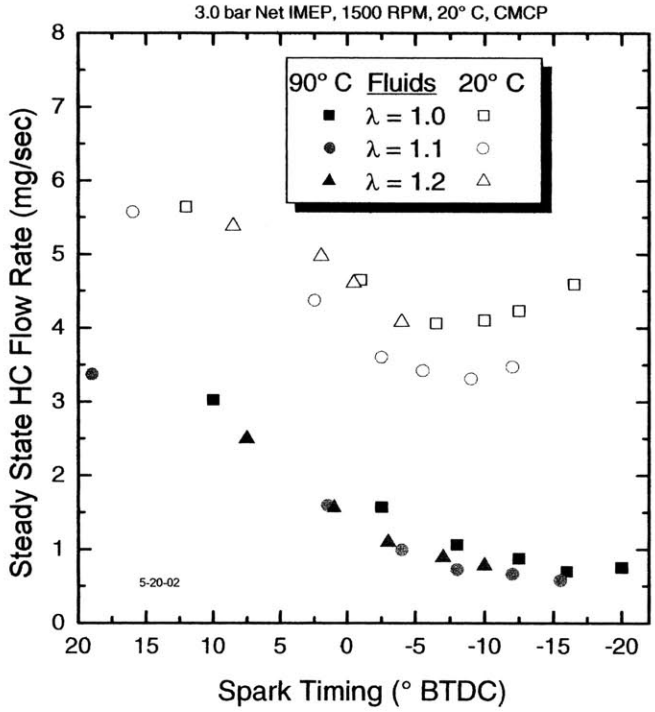

Figure 3.9 Steady-state hydrocarbon mass flow rate as function of spark timing for different relative air/fuel ratios and fluid temperatures. Data shown for 3.0 bar Net-IMEP and 1500 RPM with charge motion (CMCP).

Tailpipe-out HC mass flow rate (mg/sec) and the HC emission index (g_{HC}/kg_{Fuel}) are shown with respect to combustion phasing (crank angle location of 50% MFB) in Fig. 3.10. This figure shows the observed changes in HC emissions due to variation in fluid temperatures and relative air/fuel ratios. At a fluid temperature of 20° C and at the most aggressive retarded spark timing, approximately 1% of the fuel mass injected exited the tailpipe as HC emissions. Under

fully warmed-up conditions (90° C) approximately 0.2% of the injected fuel exited the tailpipe as HC emissions.

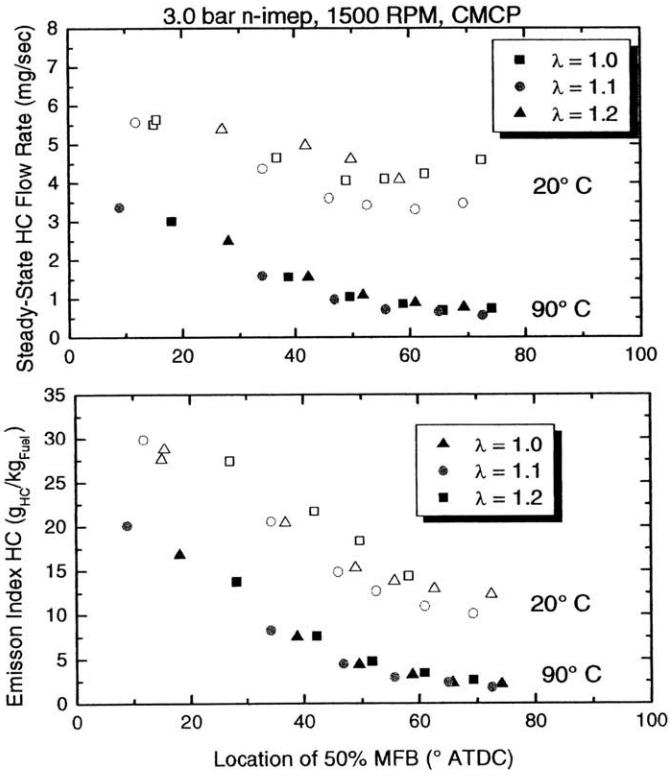

Figure 3.10 Steady-state HC flow rate and emission index HC emissions as a function of 50% MFB location for various relative air/fuel ratios and fluid temperatures at 3.0 bar Net-IMEP, 1500 RPM, with charge motion (CMCP).

3.4 Time-Resolved Hydrocarbon Concentration

3.4.1 Overview

To better understand exhaust system oxidation, crank angle-resolved HC concentrations were recorded at the exit of the exhaust port and in the exhaust runner. Figure 3.11 shows a typical crank angle-resolved HC concentration measured in parts per million of carbon atoms (ppm_{C1}) at the exit of the exhaust port, 7 cm from the exhaust valves (EV). At the time of exhaust valve opening (EVO), an initial peak was observed during the blow-down phase as head gasket, spark plug, and valve seat crevice gases were exhausted. As the blow-down process continues, there was a rapid decrease in concentration as the bulk of the burnt gases were expelled. As in-cylinder

pressure equilibrates during exhaust displacement, an increase in HC levels was observed. This feature was attributed to several possible mechanisms: a period of flow reversal, release of HC from the piston top land crevice, and out-gassing of HC from lubricant on the liner and in-cylinder deposits. Near the end of the exhaust stroke, the cylinder-wall HC boundary layer was shed, resulting in a vortex that was expelled near the end of the exhaust process, increasing the observed HC concentration. This was followed by a brief period of back-flow during valve overlap prior to exhaust valve closing (EVC) [10].

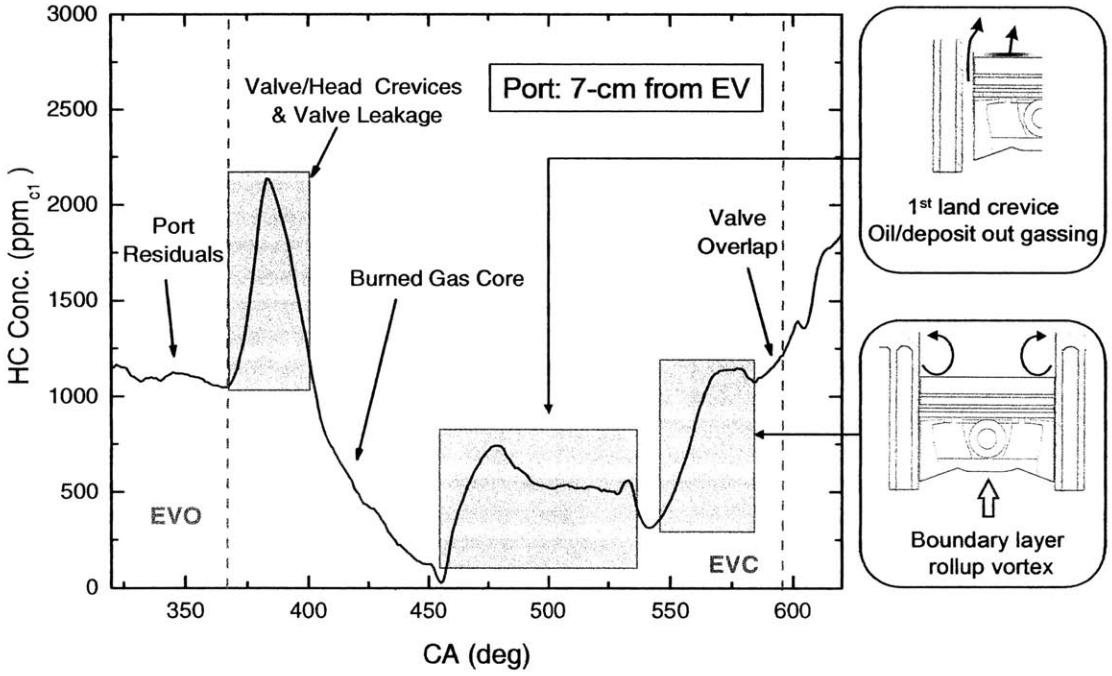

Figure 3.11 Typical time-resolved HC concentration profile measured in the exhaust port, 7 cm from the exhaust valves. Major features shown and noted during gas exchange, from exhaust valve opening (EVO) to exhaust valve closing (EVC).

3.4.2 Effect of Retarded Spark Timing

Figure 3.12 shows cylinder pressure measurements and crank angle-resolved HC concentration measured at the exit of the exhaust port, 7 cm from the exhaust valves (EV). Each column of graphs represents specific spark timings under stoichiometric (λ = 1.0) and ambient fluid (20° C) conditions. Grayed areas in Fig. 3.12 show the exhaust flow period from exhaust valve opening (EVO) to exhaust valve closing (EVC). The first row of graphs represents measured

in-cylinder pressure acquired over several cycles. Notice that with top-center-center (TDC) spark timing two distinct peaks are evident, the first due to piston motion and the second due to combustion. Fixed engine load testing required additional mass flow, resulting in greater compression stroke and exhaust blowdown pressures as ignition was retarded.

The second row of graphs shows HC concentrations (ppm_{C1}) measured in the exhaust port at a distance 7 cm from the exhaust valve seats. The grayed area again represent the period of exhaust flow. However, there was a phase delay due to the transport time within the exhaust and sampling system, in addition to a characteristic response time associated with the FFID. Note that the exhaust transport delay became smaller with increasing spark retard as the mass flow rate and in-cylinder pressures at EVO increase. For each of the three different spark timings, there was a general trend in the time history of HC concentration measured in the exhaust port. During the period of no exhaust flow, relatively high (5000 - 7000 ppm_{C1}) HC concentrations were observed for all spark timings and were attributed to stagnant residuals from a previous cycle.

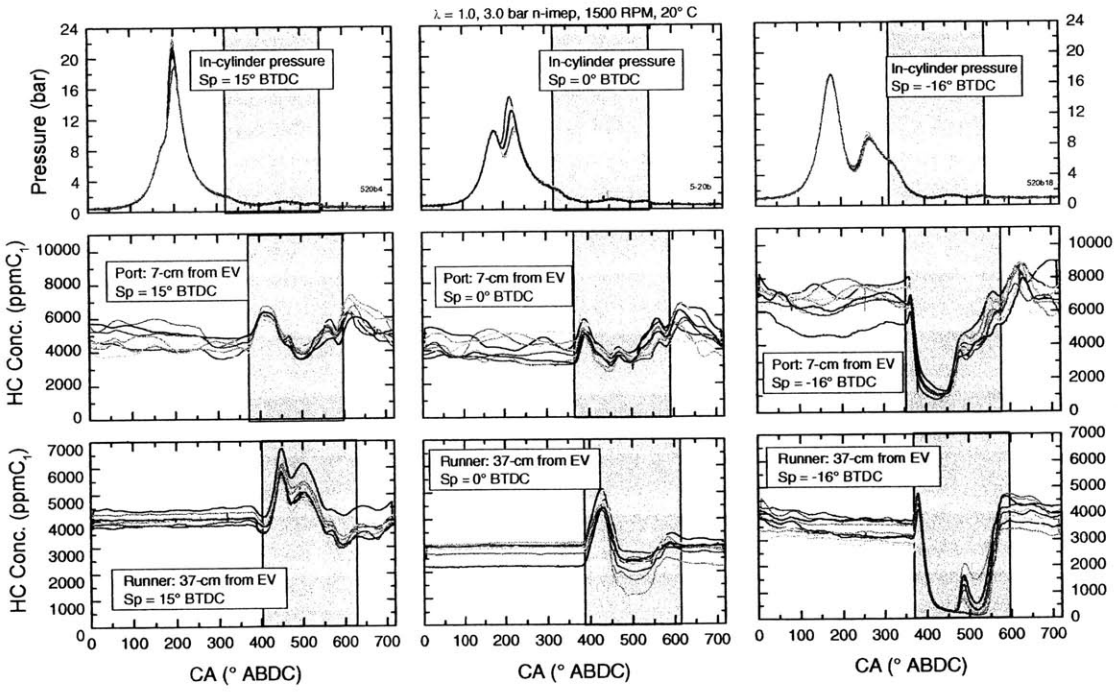

Figure 3.12 In-cylinder pressure and exhaust port and runner time-resolved HC concentration measurements for three different spark timings (Sp = 15°, 0°, -16° BTDC) at 3.0 bar Net-IMEP, λ = 1.0, CMCP, and 20° C fluids.

The last row in Fig. 3.12 shows HC concentration measured in the exhaust runner at a distance of 37 cm from the exhaust valve seats. Stagnant residual HC emissions were observed to decrease with spark retardation. During the exhaust process, depicted within the grayed areas, the HC signature was different from the signal measured in the exhaust port due to gas phase reactions within the exhaust system. As the majority of the burned gases were expelled, a single peak in the HC concentration was detected.

As spark timing was retarded, shown in the second and third columns of Fig. 3.12, the exhaust transport delay decreased as additional charge mass was required to achieve the fixed Net-IMEP. As combustion was phased later in the cycle, peak in-cylinder combustion pressures were reduced, decreasing the mass loading of HC in crevice volumes. The trend was observed in the first HC peak measured in the exhaust port, the magnitude of which decreased with spark retardation.

3.4.3 Effect of Fluid Temperatures

Additional experiments with the fast-response FID were conducted at three different fluid temperatures, 20°, 40°, and 90° C at a fixed spark timing (-1° BTDC) and Net-IMEP (3.0 bar), Fig. 3.13. In all three cases, the exhaust system was not externally cooled and was at a hot stabilized operating temperature which was approximately equal for all engine tests. The lowest HC concentrations were observed in the port and runner under fully warmed-up conditions (90° C fluids).

3.5 Analysis of Time-Resolved HC Measurements

3.5.1 Overview

As described in Section 3.4, time-resolved measurements provided insight into HC concentration levels at various exhaust locations with spark retardation. However, in order to achieve the same Net-IMEP as combustion was phased later in the cycle, the engine's mass flow rate was increased to offset the reduction in work extracted from the burnt gases. Changes in exhaust mass flow rate were addressed to better interpret the results from the time-resolved HC concentrations. To accomplish this, a simple plug flow model was developed that calculated the

mass flow rate of HC at the exit of the exhaust port and in the exhaust runner, Fig. 3.14. In order to perform the analysis at each engine operating condition, burn rate information was required and obtained from in-cylinder pressure data. Next, an engine and exhaust simulation model was developed using the results from the burn rate analysis. The simulation provided exhaust gas conditions that were required by the plug flow model. Data from the fast-response FID was then combined with the plug flow model, yielding a HC mass flow rate.

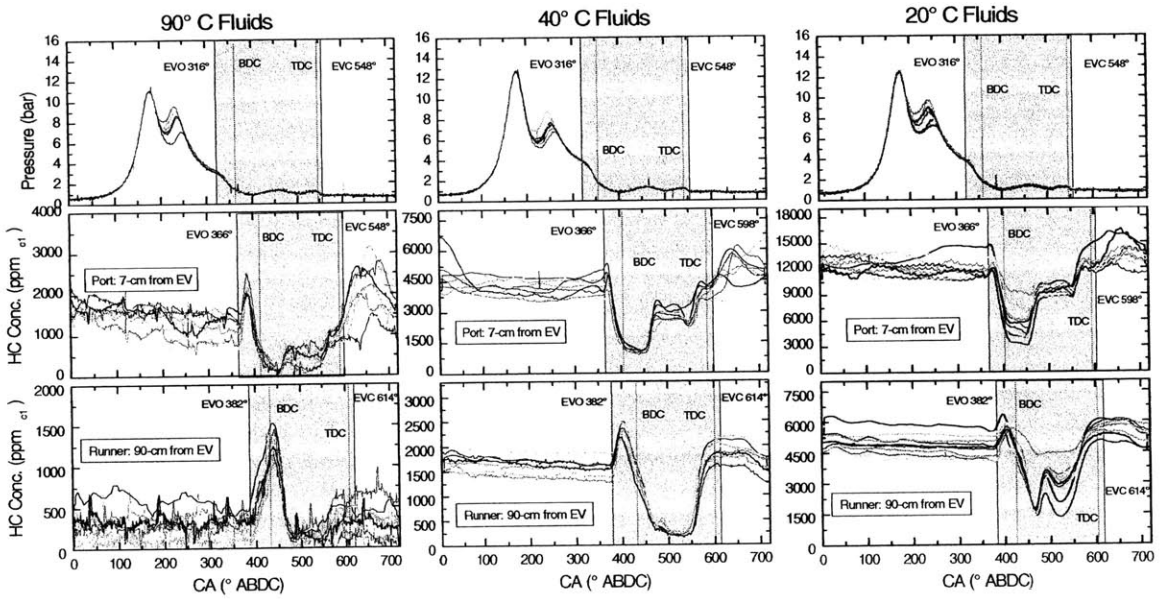

Figure 3.13 In-cylinder pressure and time-resolve HC concentration measured in the port and runner for 90°, 40°, 20° C fluid temperatures, spark timing = -1° BTDC, $\lambda = 1.0$, and without charge motion (CMCP).

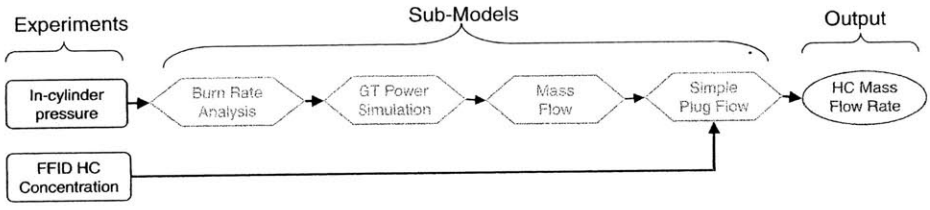

Figure 3.14 Overview of mass plug flow model used for analysis of time-resolved HC concentrations.

3.5.2 ENGINE SIMULATION MODEL

GT-Power, engine simulation software from Gamma Technologies, was applied to model the engine and exhaust system. The cycle simulation was based upon one-dimensional gas dynamics incorporating the effects of fluid flow and heat transfer. In-cylinder contents were modeled in a two-zone thermodynamic state (burned and unburned) with a variable volume. The model included the effects of heat transfer to the cylinder boundaries, work transfer to the piston, and mass trapped in crevice volumes. The cycle simulation required user inputs such as 10-90% combustion duration, 50% MFB location, RPM, MAP, relative air/fuel ratio, and engine surface temperatures.

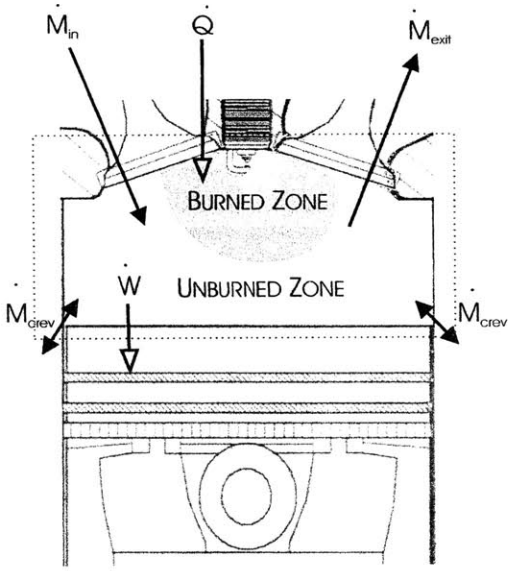

Figure 3.15 Engine cycle simulation thermodynamic model of open system, including crevices, work transfer to piston, and heat transfer to cylinder boundaries.

The engine exhaust system was modeled as a series of pipes and junctions, Fig. 3.16. The 1-D flow code simultaneously solved the continuity, momentum, and energy equations, Eqs. (3.2), (3.3), and (3.4). Pipe and junction elements were discretized into numerous volumes with boundary conditions that were used to obtain a flow solution. Each pipe element was scaled with a friction multiplier, heat transfer multiplier, and pressure loss coefficient. Friction losses were based upon the Reynolds number and the surface roughness of the walls. Established heat transfer coefficients were dependent upon fluid velocity, thermo-physical properties, and the wall surface

finish. Intake and exhaust valve discharge coefficient and lift profile were inputted by the user. For more information regarding GT-Power's engine simulation, refer to Gamma Technologies user's manuals.

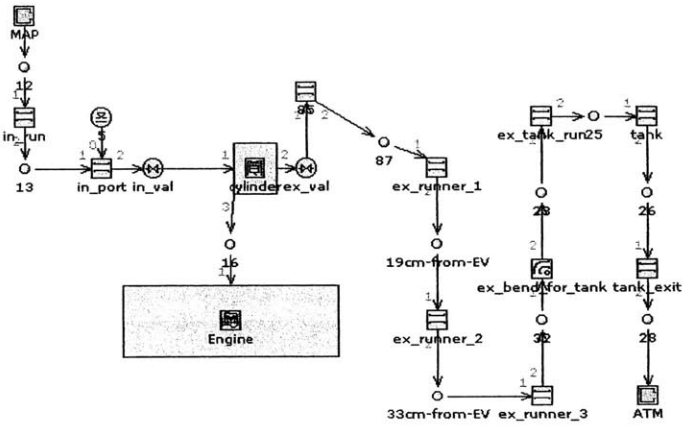

Figure 3.16 GT-Power model of single-cylinder engine with intake and exhaust system.

$$\frac{dm}{dt} = \sum_{boundaries} mflx \tag{3.2}$$

$$\frac{d(me)}{dt} = p\frac{dV}{dt} + \sum_{boundaries}(mflx * H) - h_g A(T_{gas} - T_{wall}) \tag{3.3}$$

$$\frac{d(mflx)}{dt} = \frac{dpA + \sum_{boundaries}(mflx * u) - 4C_f \frac{\rho u^2}{2}\frac{dxA}{D} - C_p\left(\frac{1}{2}\rho u^2\right)A}{dx} \tag{3.4}$$

where:

$mflx$	*boundary mass flux*
m	*mass of volume*
V	*volume*
p	*pressure*
ρ	*density*
A	*flow area*
e	*internal energy*
H	*total enthalpy*
h_g	*heat transfer coefficient*
U	*velocity at center of volume*
u	*velocity at boundary*
C_f	*skin friction coefficient*
C_p	*pressure loss coefficient*
D	*equivalent diameter*
dx	*thickness of mass element*
dp	*pressure differential across dx*

From the simulation, the exhaust temperature, mass flow rate, and velocity were determined and shown in Fig. 3.17. Highest exhaust gas temperatures were observed during the blowdown phase of the exhaust process. The mass flow rate was observed to be highest during the initial blowdown period and gradually decreased until a period of back-flow was observed due to the single cylinder exhaust dynamics. The outflow of exhaust gas continued during the displacement process with a slight flow reversal noted during the valve overlap period.

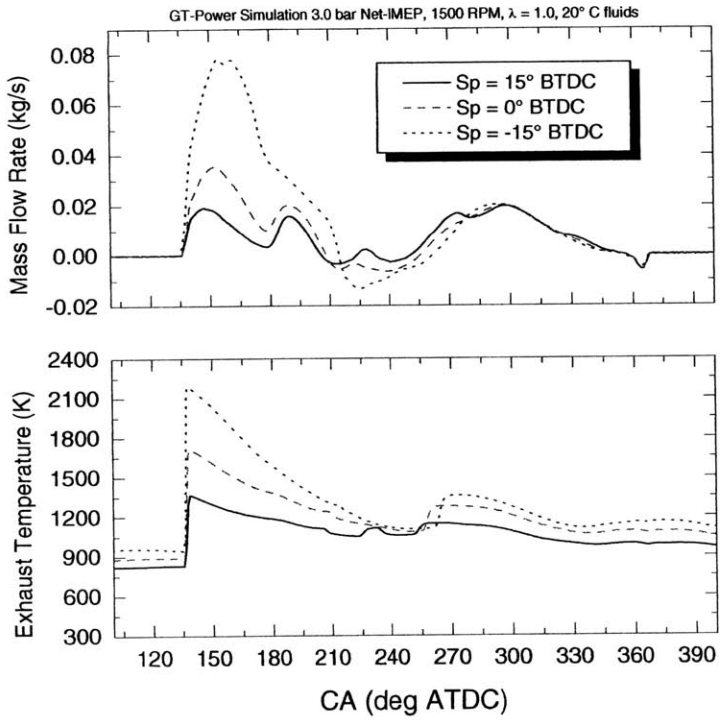

Figure 3.17 Port exit exhaust mass flow rate and exhaust gas temperature predicted by the engine model at the exit of the exhaust valves versus crank angle for various spark timings at 3.0 bar Net-IMEP, 1500 RPM, $\lambda = 1.0$, and 20° C fluids.

3.5.3 TIME-RESPONSE HC MEASUREMENTS

Due to the fast time transient response of the FFID, a small sample of gas was required to determine HC concentrations. To ensure the point measurement was representative of the entire cross section, additional experiments were performed to ensure spacial HC uniformity at the farthest upstream sampling location, 7 cm from the exhaust valves. Four different sample locations were investigated along the exit plane of the exhaust port for 10 consecutive cycles, Fig. 3.18.

Cyclical and spacial variations were not observed during the period of exhaust flow and all fast-response FID measurements were assumed to be representative of the entire cross section.

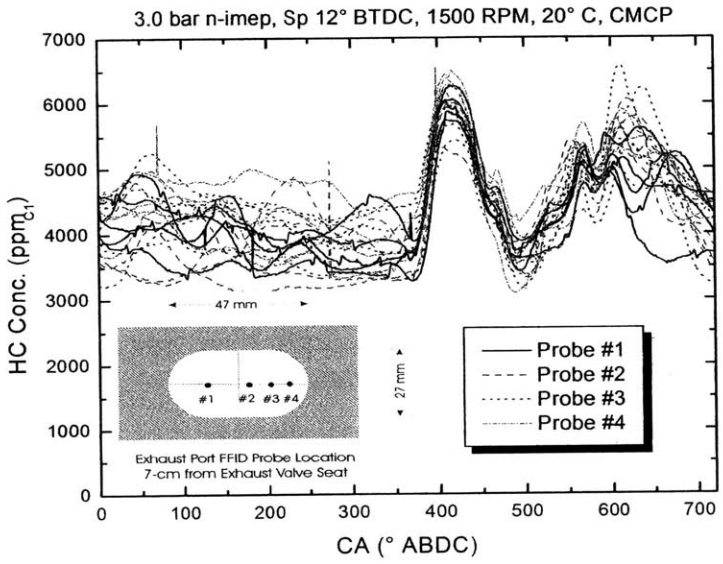

Figure 3.18 Spatial and cyclic variations of the time-resolved HC measurements in the exhaust port, 7 cm from exhaust valves at several port-exit locations.

3.5.4 PORT AND RUNNER HC MASS FLOW RATE

Results from the cycle simulation were analyzed in conjunction with the time-resolved HC measurement to obtain instantaneous HC mass flow rates in the exhaust port and runner. Figure 3.19 contains four sub-charts: in-cylinder pressure measured experimentally and calculated by the cycle simulation, exhaust port and runner instantaneous mass flow rate from the simulation, measured exhaust port and runner time-resolved HC concentrations, and calculated exhaust port and runner instantaneous HC flow rate. The time-resolved HC measurements were time (crank angle) aligned for transport and time response delays. Overall HC measurement delays varied from 25° to 85° CA due to changes in exhaust blowdown pressures as spark timing was retarded and engine mass flow rates increased.

A simple flow model was developed in MatLab assuming pure displacement plug flow of the exhaust mass. The mass of HC contained in each mass element was calculated from experimental and computational data yielding an instantaneous HC mass flow rate during the

period of exhaust flow. Steady-state HC flow rates were obtained by integrating the instantaneous HC flow from EVO to EVC.

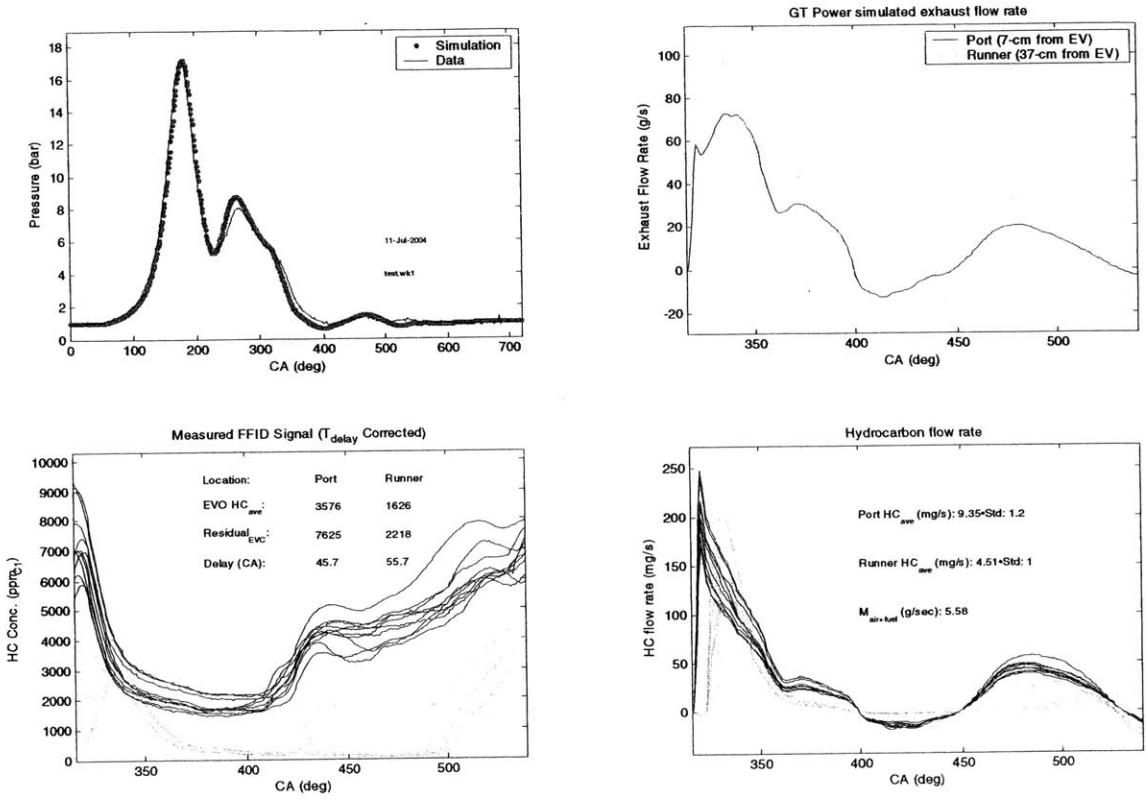

Figure 3.19 Model results from analysis of HC measurements. GT-Power simulation results of in-cylinder pressure and exhaust mass flow rate at the port exit and runner. Measured HC concentration and resulting HC mass flow rate computed by a plug flow model.

Exhaust port exit and runner HC emissions are shown in Figs. 3.20-3.23 for two relative air/fuel ratios and various combustion phasings. Time-averaged HC emissions measured in the exhaust tank (120 cm from EV) are shown for comparison. Hydrocarbon levels calculated in the port and runner by the FFID measurements agreed quantitatively with the time-averaged measurements; the highest emissions were observed at the port exit and decreased with distance from the exhaust valves. The fraction of hydrocarbons oxidized in the exhaust port reached a maximum with top-center spark timings. HC oxidation rates in the runner were modest (10%) with 15° and 0° BTDC spark timings and became significant (40-50%) with additional spark retardation (-15° BTDC). Total exhaust system oxidation increased with later spark timings, and

reached a maximum (68%) for -15° BTDC spark timing and stoichiometric engine operation. Exhaust runner oxidation was not observed to be significant until after TDC spark timings, Figs, 3.26 and 3.28. However, when port exit HC emissions were expressed as a percentage of the fuel injected, HC emissions remained constant at approximately 3%, independent of combustion phasing and stoichiometry.

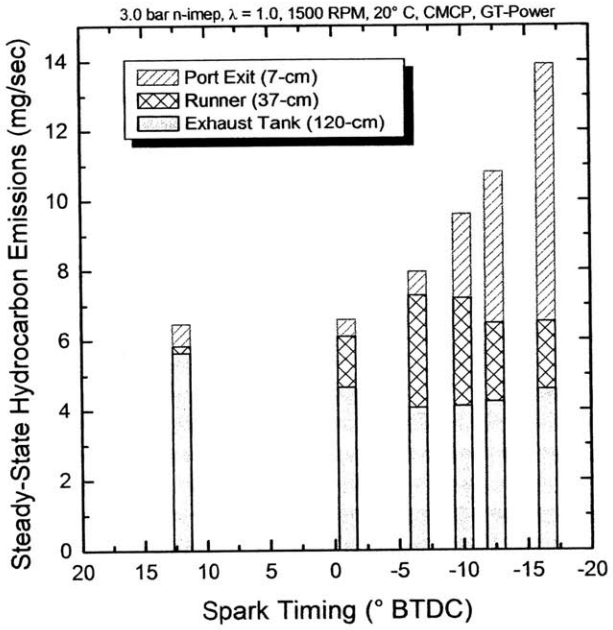

Figure 3.20 Steady-state HC emissions as a function of spark timings measured in three locations under $\lambda = 1.0$, 20° C fluids.

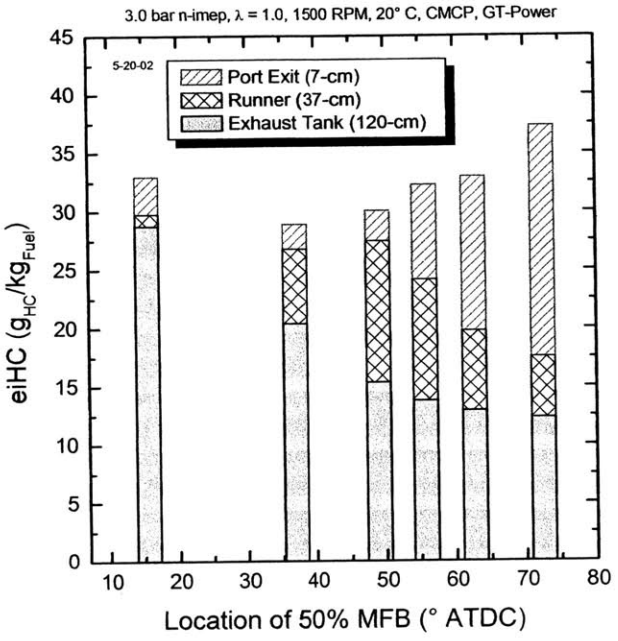

Figure 3.21 Emission index HC emissions as a function of location of 50% MFB for different exhaust locations under $\lambda = 1.0$ and 20° C fluids.

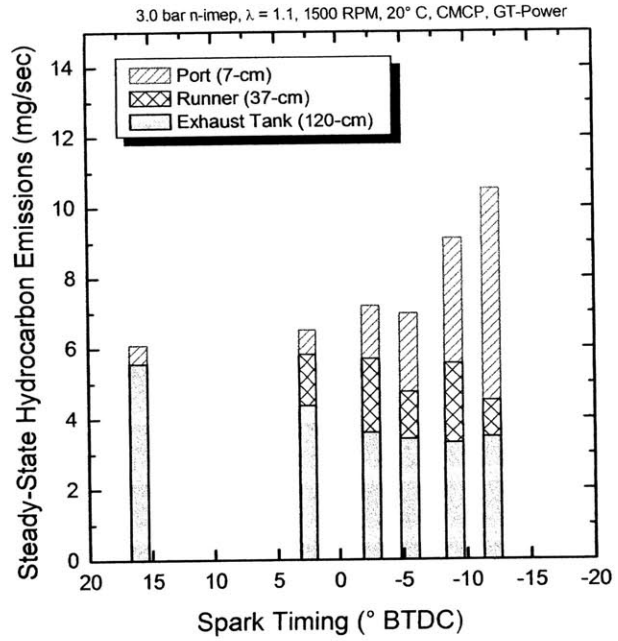

Figure 3.22 Steady-state HC emissions as a function of spark timing for three different locations under $\lambda = 1.1$ and 20° C fluids.

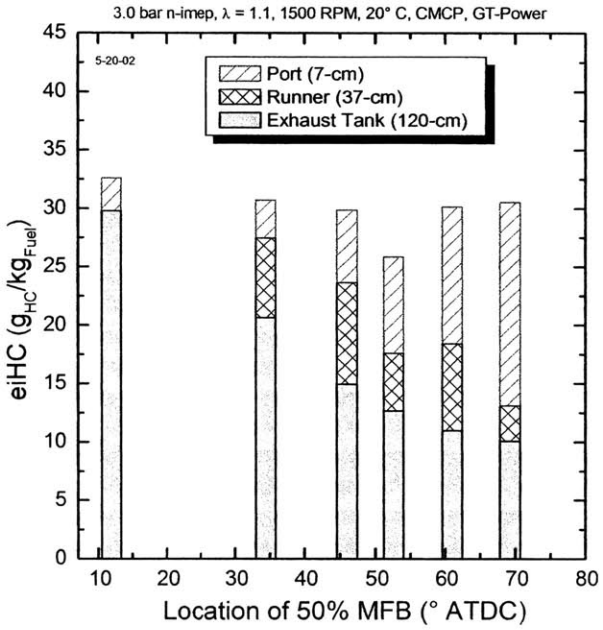

Figure 3.23 Emission index HC emissions as a function of the location of 50% MFB for three different locations under $\lambda = 1.1$ and 20° C fluid.

3.6 Quenching Experiments

In order to determine the extent of HC oxidation within the exhaust port, cylinder-exit HC emissions were investigated using exhaust quenching experiments. Hydrocarbon reactions were frozen by rapidly reducing exhaust gas temperatures at the exit plane of the exhaust valves with CO_2. Timed injection of quench gas prevented artificial cooling of the exhaust port and valves, reduced exhaust back pressure, and minimized changes to residual gas temperature and composition. However, response times of the solenoid valves controlling the injection of CO_2 was limited, and the quench gas could not be phased directly with the exhaust event, Fig. 3.24. As a result, the mass of quench gas per cycle ($mCO_{2Quench}$) included the mass injected while the exhaust valves were closed (displacing gas in the exhaust system) and the mass injected during the exhaust process (mixing with burnt gases exiting the cylinder). Experiments were performed using fixed CO_2 injection durations and timings that were optimized for a stable and repeatable injection event. Although the engine was operated at high intake manifold pressure, back-flow of CO_2 into the cylinder during valve overlap was a concern. Increased residual gas dilution with CO_2 would

raise the specific heat of the residual gas, reducing peak combustion temperatures and lowering NO_x emissions. Therefore, NO_x emissions were monitored under quenching and non-quenching conditions to assess any back-flow impact.

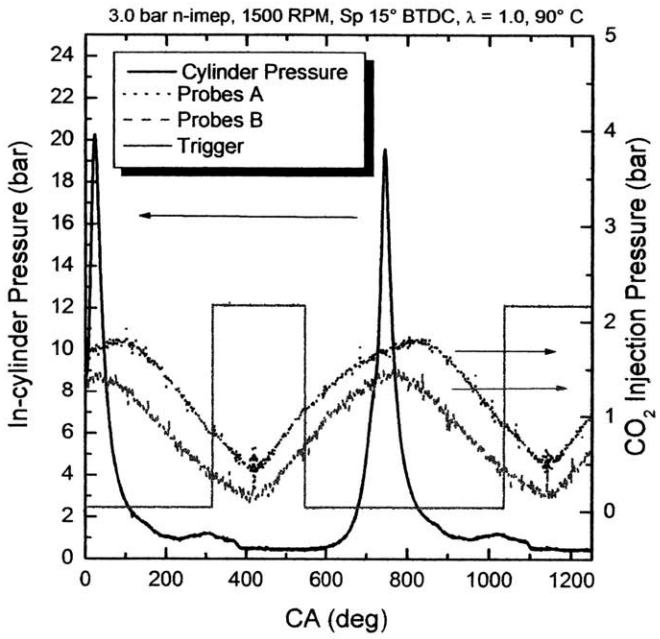

Figure 3.24 Phasing of quench gas injection as a function of crank angle. Data shown with in-cylinder pressure and solenoid trigger signal for 3.0 bar Net-IMEP, 15° BTDC spark timing, and $\lambda = 1.0$.

Cylinder-exit HC and NO_x emissions with quenching were normalized with equivalent non-quenching values. Figure 3.25 shows quenching experiments conducted for three spark timings under stoichiometric and 20° C fluid conditions. Results were expressed as a ratio of the mass of CO_2 injected to the mass of fuel and air entering the cylinder. The amount of quenching gas was increased until cylinder-exit HC emissions were found to reach a plateau. In all cases, this cylinder-exit HC emissions plateau was obtained while altering NO_x levels by less than 10%.

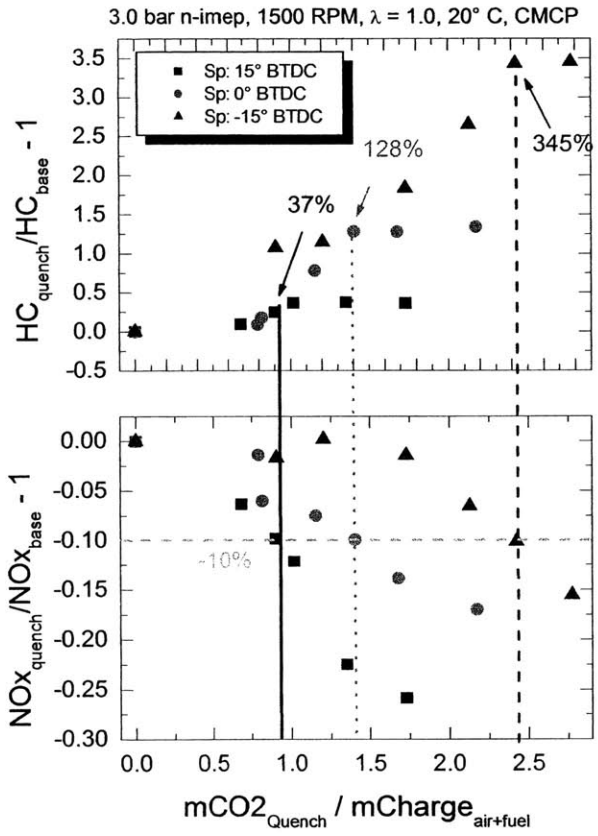

Figure 3.25 Change in HC and NO_x emissions as a function of the ratio of mass of quench gas to mass of charge ($mCO2Quench/mCharge_{air+fuel}$) for three spark timings with $\lambda = 1.0$ and 20° C fluids.

Results from the quenching experiments provided cylinder-exit HC emissions and hydrocarbon tracking information reported as both steady-state HC flow rate and emission index, at the four exhaust locations; cylinder-exit, port exit, runner, and exhaust tank can be found in Figs. 3.26 and 3.27, respectively, for stoichiometric ($\lambda = 1.0$) operation. Additional exhaust HC tracking information for $\lambda = 1.1$ is shown in Figs 3.28 and 3.29.

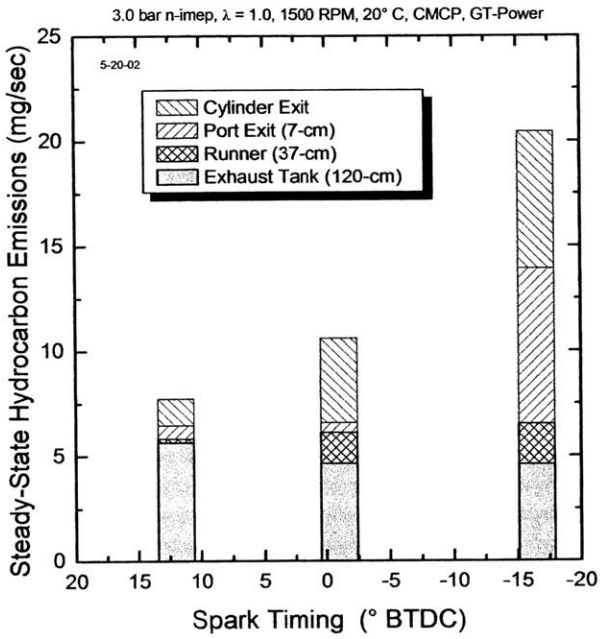

Figure 3.26 Steady-state HC emissions as a function of spark timing at four locations (cylinder exit, port exit, runner, and mixing tank) under $\lambda = 1.0$ and 20° C fluids.

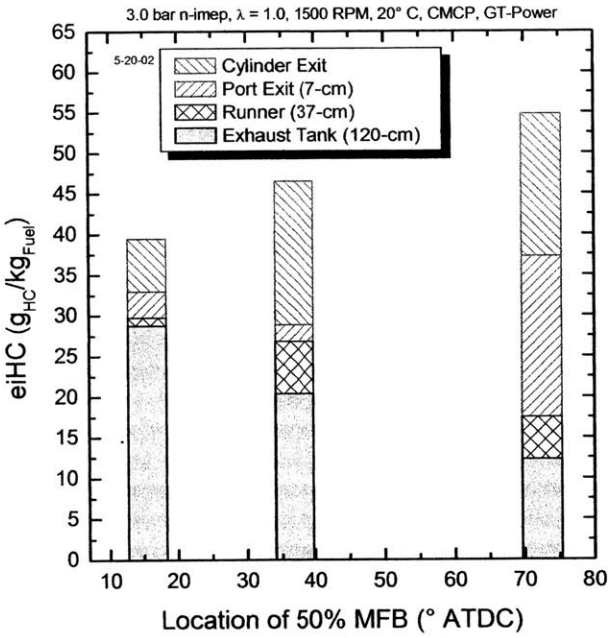

Figure 3.27 Emission index HC emissions as a function of 50% MFB location at four locations under $\lambda = 1.0$ and 20° C fluids.

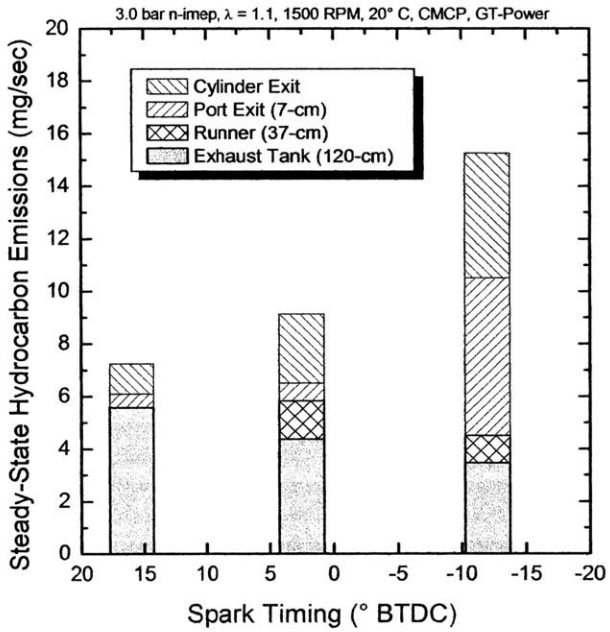

Figure 3.28 Steady-state HC emissions as a function of spark timings at four locations under $\lambda = 1.1$ and 20° C fluids.

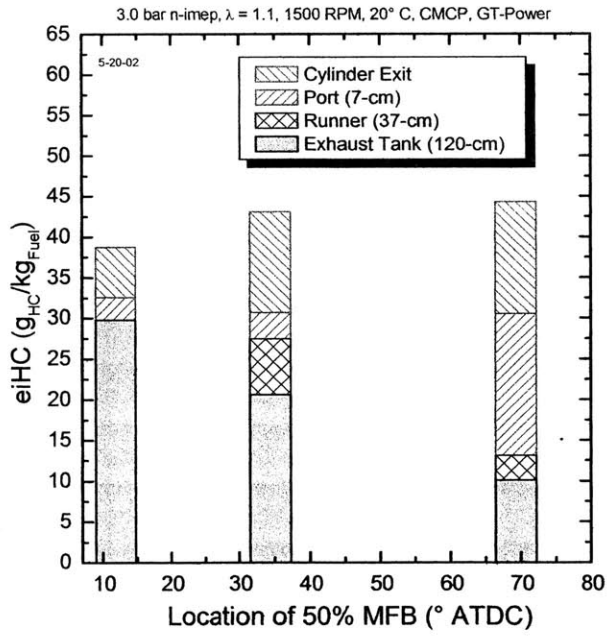

Figure 3.29 Emission index HC emissions as a function of 50% MFB location at four locations for $\lambda = 1.1$ and 20° C fluids.

3.7 SECONDARY AIR INJECTION

3.7.1 OVERVIEW

Several technologies exist that assist in reducing engine-out HC levels and improve catalyst light-off times. One such strategy involves the use of secondary air injection (SAI) into the exhaust port to accelerate converter warm-up. This mode of operation requires the engine to be operated under fuel-rich conditions forming reactive partially oxidized products in the exhaust gas: hydrogen (H_2), carbon monoxide (CO) and hydrocarbons (HC). When mixed with air in the exhaust port, exothermic reactions occur, raising gas temperatures and reducing converter-in emissions. Fuel-rich engine operation also results in a more robust and stable combustion, allowing for additional spark retardation from MBT. Previous studies have investigated the importance of proper air delivery systems and exhaust manifold designs [11-13]. Mixing rates and residence times within the exhaust system have a dramatic impact on converter-in HC emissions and catalyst light-off times [12]. Large heat losses per unit length of exhaust reduces exhaust gas temperatures and results in longer ignition delays of the reactive components.

3.7.2 FIXED ENGINE RELATIVE AIR/FUEL RATIO

Experiments were conducted at the same fixed engine torque (3.0 bar Net-IMEP), and fixed engine relative air/fuel ratio ($\lambda_{engine} = 0.85$), with the secondary air injected at the exhaust valve seats. The setup was not equipped with a catalytic converter. Therefore, a distance of 37 cm from the exhaust valve seats was selected to represent the flow length of the catalyst inlet on a modern multi-cylinder engine. Exhaust relative air/fuel ratio ($\lambda_{exhaust}$) was varied experimentally as CO and HC emissions and exhaust gas temperatures were quantified. In Fig. 3.30, air was continuously injected at the valve seats as exhaust stoichiometry was varied. Port temperatures decreased due to burnt gases mixing with the injected air. Exothermic reactions at the runner location raised the exhaust gas temperature, as the secondary air oxidized CO, H_2, and HC. A trade-off existed between exhaust gas temperature and HC emissions. Excessive secondary air over-cooled the mixture, quenched reactions rates, and resulted in higher HC emissions and lower exhaust gas temperatures.

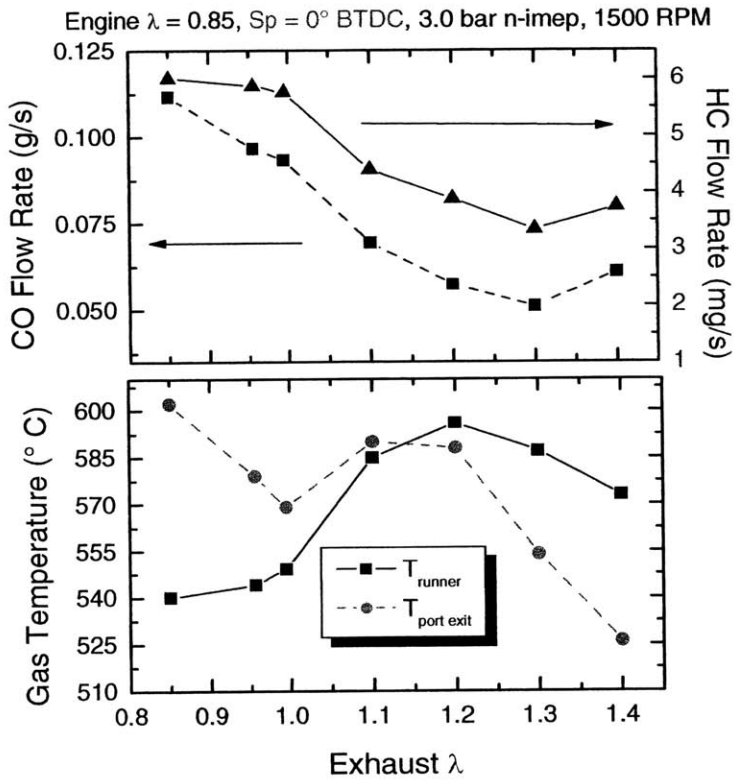

Figure 3.30 Exhaust secondary air injection experiments conducted at an engine relative air/fuel ratio of 0.85 (λ_{engine}) as a function of with exhaust relative air/fuel ratio. Data shown for 3.0 bar Net-IMEP, 1500 RPM, 0° BTDC spark timing, and 20° C fluids.

3.7.3 TIMED SECONDARY AIR INJECTION

Comparisons of different pulsed air injection events and continuous air injection was investigated for a single engine operating condition and a fixed mass of secondary air ($\lambda_{exhaust}$ = 1.2, spark timing 0° BTDC). Injection event "B", as illustrated in Fig. 3.31, was timed to be in phase with the exhaust blow-down process. The remaining pulsed injections were phased in increments of 180° CA with respect to the exhaust valve opening event. Continuous air injection, compared to phased injection, was found to yield the highest exhaust gas temperatures and lowest HC levels measured in the exhaust runner with the setup used in these experiments.

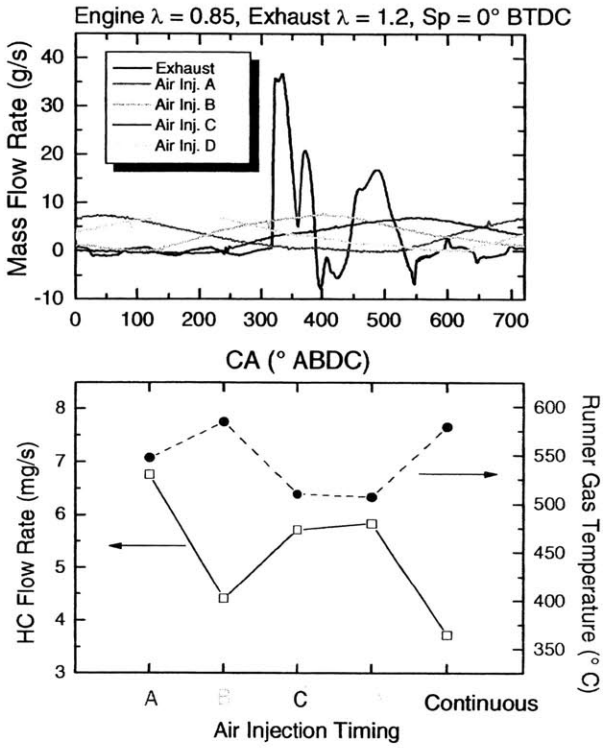

Figure 3.31 Hydrocarbon flow rate and runner exhaust gas temperatures as a function of various secondary air injection timings for a fixed engine (λ_{engine} = 0.85) and exhaust stoichiometry ($\lambda_{exhaust}$ = 1.2). Data shown for 3.0 bar Net-IMEP, 1500 RPM, and 20° C fluids.

3.7.4 TAILPIPE-OUT HC EMISSIONS AND FEED GAS SENSIBLE ENTHALPY

Relative magnitudes of well downstream HC emissions and sensible enthalpy flow rates with aggressive spark retardation were compared with SAI engine operation in Fig. 3.32. Results were shown relative to a stoichiometric base case with a 15° BTDC spark timing. For the SAI tests, exhaust stoichiometry was varied from a relative air/fuel ratio of 0.85 to 1.4. Use of SAI yielded the lowest HC emission and highest enthalpy rates for a fixed level of spark retardation. With aggressive (-15° BTDC) spark retard, SAI operation was observed to reduce HC flow rates approximately 60% while increasing the sensible enthalpy flow by a factor of 3.8 compared to the baseline conditions.

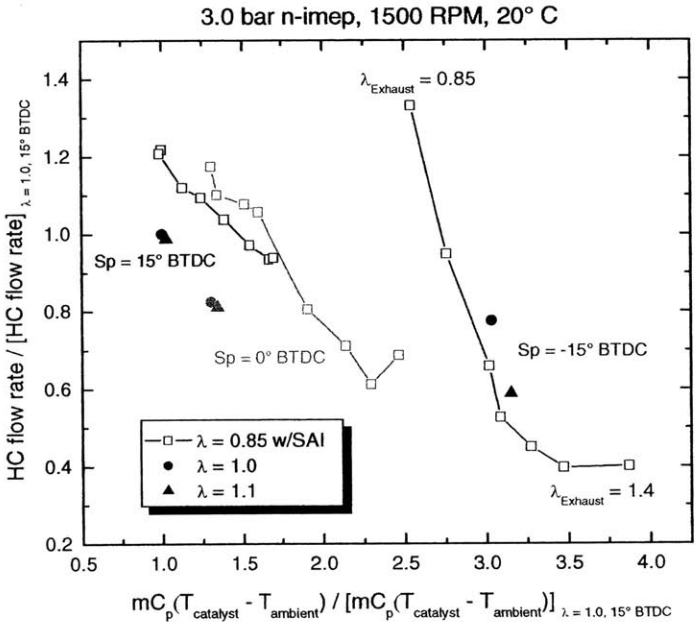

Figure 3.32 Normalized HC flow rate as a function of normalized sensible feed gas enthalpy rate for three spark timings. Data shown for λ = 1.0, 1.1, and secondary air injection (SAI) at a fixed engine relative air/fuel ratio (λ_{engine} = 0.85) with exhaust enleanment from $\lambda_{exhaust}$ = 0.85 to 1.4 Shown with respect to λ = 1.0 and 15° BTDC spark timing baseline condition, 3.0 bar Net-IMEP, 1500 RPM, and 20° C fluids

CHAPTER 4

MULTI-CYLINDER EXPERIMENTAL RESULTS

4.1 ENGINE STARTUP OVERVIEW

Ambient startup is a complicated process that requires delivery of an adequate relative air/fuel ratio around the spark plug gap for a robust combustion event during engine cranking. Upon the first cylinder firing, the engine accelerates, resulting in an RPM flare and a rapid decrease in intake manifold pressure. During this transient period, spark timing is advanced as engine speed and in-cylinder exhaust gas residuals increase. Several parameters (MAP, RPM, spark timing, and relative air/fuel ratio) were acquired during the first 20 seconds following an ambient startup and are shown in Fig. 4.1. Due to RPM flare and the complex nature of the startup event, emissions from the first second of engine operation (noted in the grayed areas of Fig. 4.1) was excluded from the analysis and no attempt was made at altering the first second "crank" and "run" fueling or timing strategy.

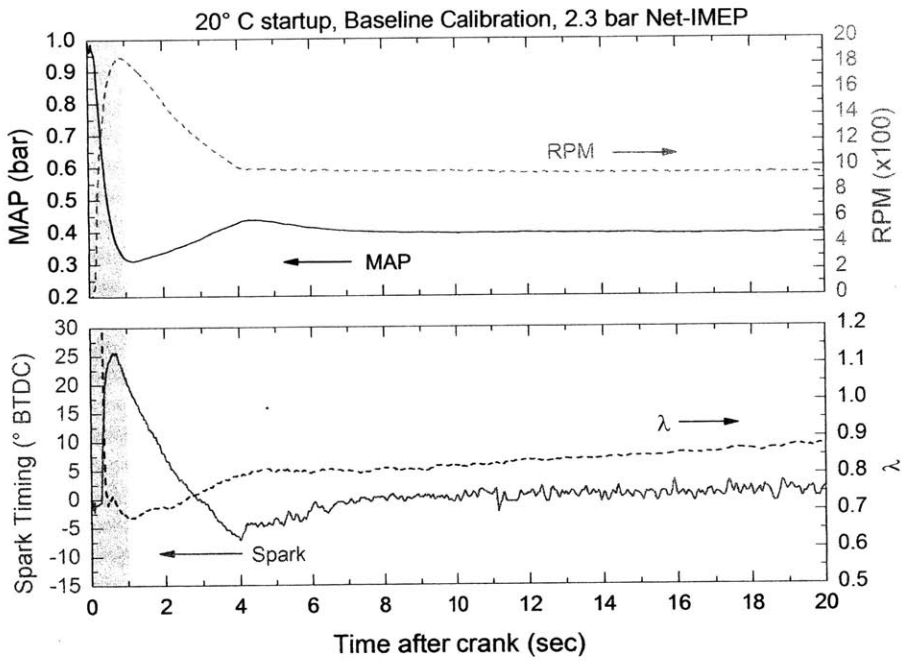

Figure 4.1 Baseline calibration MAP, RPM, spark timing, and relative air/fuel ratio as a function of time after crank. Data from an ambient startup under idle load and speed conditions.

During a typical 20° C (ambient) start, the baseline calibration resulted in an idle speed of approximately 1000 RPM and TDC (0° BTDC) spark timing, 5 seconds after engine cranking. Net-IMEP averaged 2.3 bar with 4% COV and an 8% Net-IMEP imbalance cylinder-to-cylinder. Multi-cylinder experiments focused on the initial 1-20 seconds of operation following an ambient start. During this transient warm-up period, combustion stability, HC, CO, and CO_2 emissions, and feed gas enthalpy were evaluated for four late spark timing strategies.

Spark timing "blend" and "run" tables were modified using Caltools software and uploaded to the ECM using the MDS. Spark timings during the engine cranking period were not modified, only the magnitude of spark timings during the "blend" and "run" period were altered and the trajectory remained the same. All calibration changes were referred to as spark modifications ($\Delta\theta_{sp}$) and were slewed relative to the baseline calibration spark timing, $\Delta\theta_{sp} = 0°$, observed in the stock ECM file, Fig. 4.2. Fueling "blend" and "fast choke" tables and the idle air control (IAC) stepper position tables were varied in order to maintain the same air/fuel ratio as the engine's mass flow was adjusted during open loop operation. Default air/fuel feedback control was established in 20 seconds (~200 engine cycles) after startup. Accelerated closed loop control was achieved in approximately 10 seconds by pre-heating the exhaust gas oxygen (EGO) sensor before startup and making appropriate changes to the calibration file, Fig 4.3. Test-to-test variations in air/fuel ratio was 14.6 ± 0.5.

4.2 COMBUSTION CHARACTERISTICS

4.2.1 COMBUSTION STABILITY

The extent of late combustion phasing was limited by the COV of the Net-IMEP. As spark timing was retarded from the baseline calibration, there was a noticeable decrease in idle quality and an increase in the engine's noise, vibration, and harshness (NVH). Therefore, at each of the four different spark modification, combustion stability was investigated during a quasi-steady idle period (second 4 to second 20 after startup) that contained approximately 130 engine cycles. Spark timings were modified ($\Delta\theta_{sp}$ = -5°, -10°, and -15°) with respect to the baseline ($\Delta\theta_{sp} = 0°$) ECM calibration tables. Under idle load conditions, the baseline spark timing yielded a COV of Net-IMEP of approximately 4% across all four cylinders. Combustion stability decreased as

combustion was phased later in the expansion stroke; a COV of 8% was observed with the most aggressive retarded spark timing modification, $\Delta\theta_{sp} = -15°$.

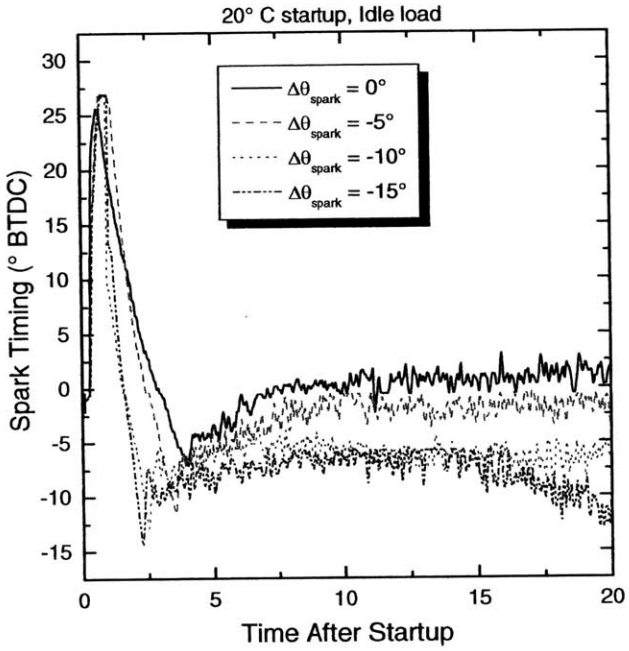

Figure 4.2 Spark timing as a function of time after startup for various spark modifications ($\Delta\theta_{spark}$).

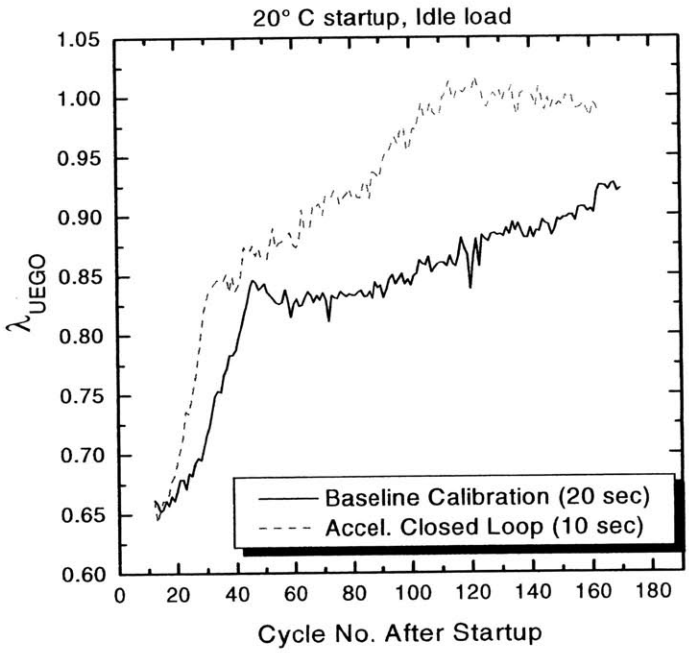

Figure 4.3 Measured UEGO relative air/fuel ratio (λ) as a function of cycle no. after startup. Data shown for accelerated closed loop control compared to baseline calibration.

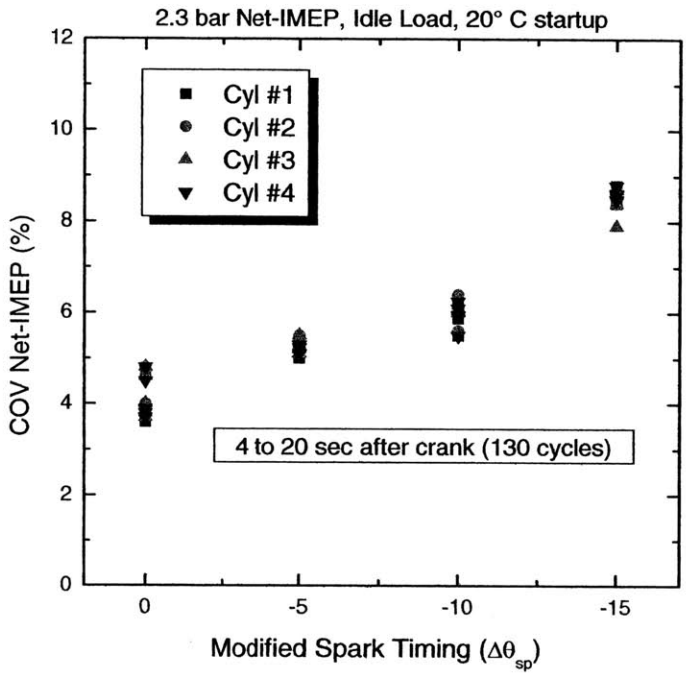

Figure 4.4 COV of Net-IMEP as a function modified spark timing, 4 to 20 seconds after crank (130 cycles). In-cylinder pressure data acquired from all four cylinders at idle speed and load conditions following an ambient start.

4.2.2 BURN RATE ANALYSIS

Burn rate analysis was conducted on from second 1 to second 20 following ambient startup. The location of the 50% MFB and 10-90% combustion duration were obtained from in-cylinder pressure data acquired from cylinder no. 4. During the quasi-steady idle period, after 60 engine cycles, the 50% MFB location increased with the level of spark retardation. With very late spark timings, large variations in the location of the 50% MFB was observed as combustion was phased later in a rapidly expanding cylinder volume, Fig. 4.5. As expected, the 10-90% combustion duration was observed to increase with increasing spark retardation, Fig. 4.6.

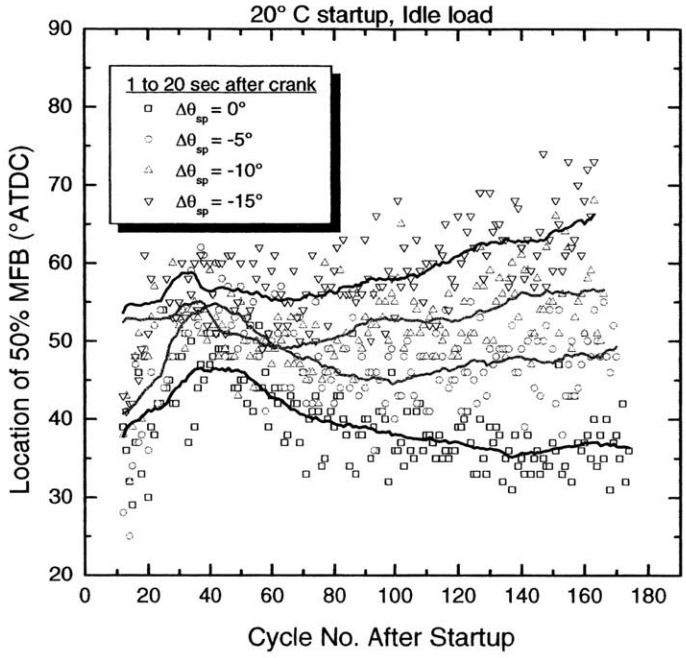

Figure 4.5 Location of 50% MFB as a function of cycle number after 20° C startup. Data shown for various spark timing modifications under idle speed and load conditions.

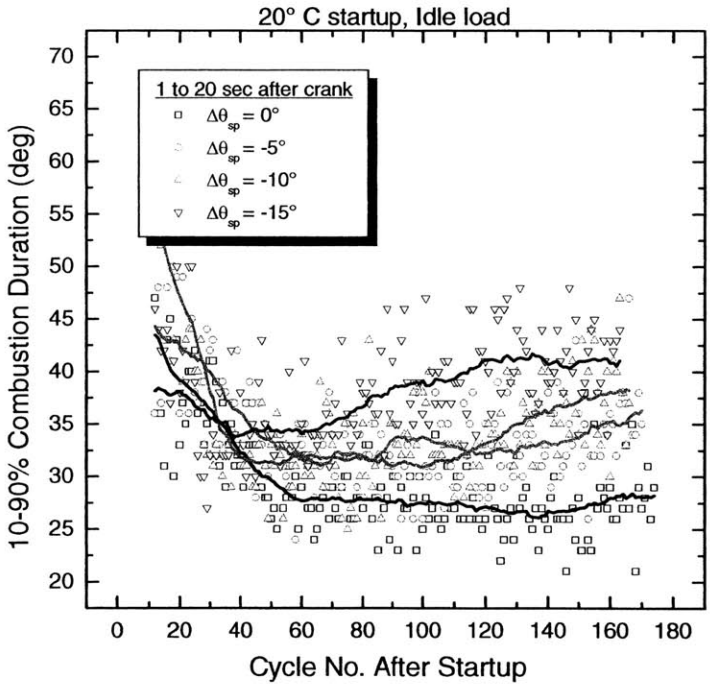

Figure 4.6 Combustion duration (10-90%) as a function of cycle number after 20° C startup. Data shown for various spark timing modifications under idle speed and load conditions.

4.3 EXHAUST EMISSIONS

4.3.1 TIME-RESOLVED CO AND HC EMISSIONS

Time-resolved cylinder no. 4 port exit and converter-in HC concentration measurements were taken for the first 20 second of engine operation, Fig. 4.7. Port HC levels were constituently higher than converter-in levels due to exhaust system oxidation and contribution from the other three cylinders.

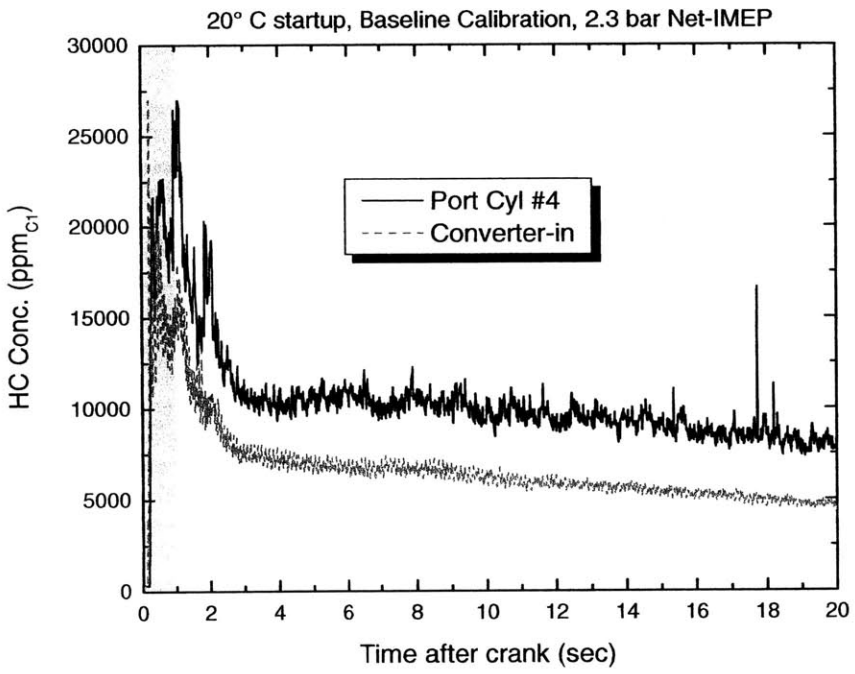

Figure 4.7 Cylinder no. 4 port exit and converter-in hydrocarbon concentrations (ppmC1) for the first 20 seconds following a 20° C start. Baseline timing and fueling calibration under idle load and speed conditions.

Experiments were conducted to evaluate HC and CO emission levels at the exhaust port exit of cylinder no. 4 for various spark timings. The engine was operated under idle speed and load conditions (1000 RPM and 2.3 bar Net-IMEP) following an ambient startup. In-cylinder pressure and emission levels from cycle 200 to 210 were investigated at three spark timings; 3°, -1°, and -6° BTDC under stoichiometric closed loop control. The results are shown in Fig. 4.8, all

concentrations were measured on a wet basis and the grayed areas represent the period of exhaust flow.

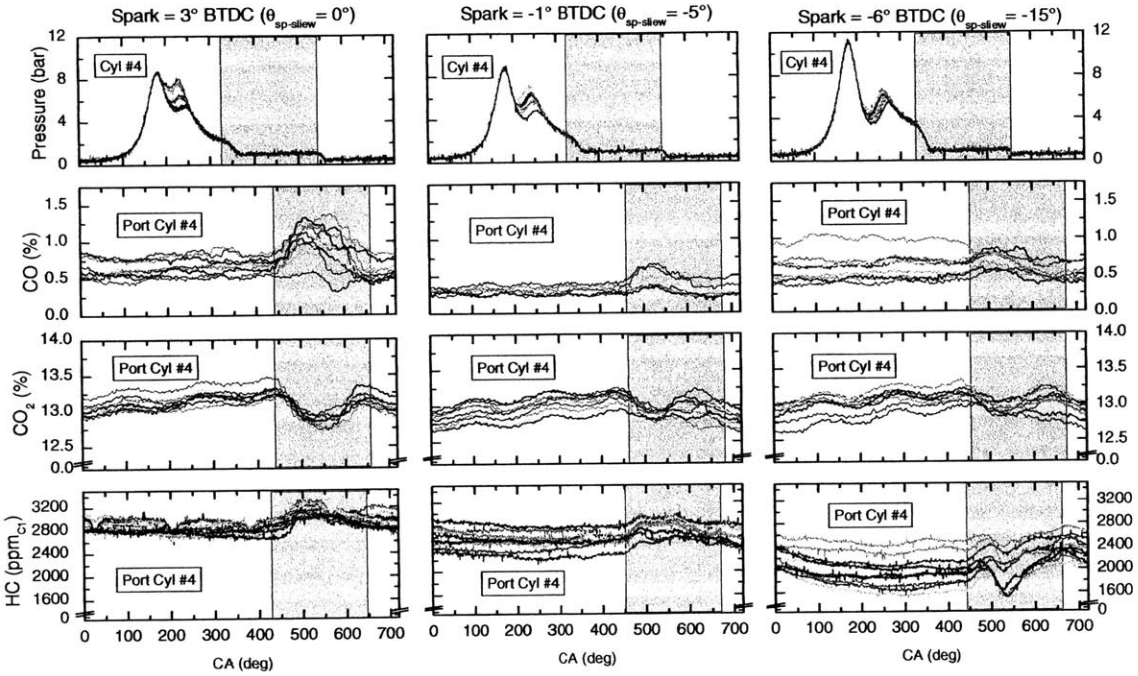

Figure 4.8 Cylinder no. 4 pressure, CO, CO_2, and HC time-resolved concentrations measured at the exhaust port exit of cylinder no. 4 as a function of crank angle (CA). Data shown for three different spark modifications (absolute spark timings: 3°, -1°, -6° BTDC) from cycle 200 to 210, stoichiometric closed loop control and idle speed and load conditions (2.3 bar Net-IMEP, 1000 RPM, λ = 1.0).Grayed areas show period of exhaust flow.

As the spark timing is retarded from the baseline value (3° BTDC), port exit CO concentrations decreased from a peak of 1.3% to 0.8% during the exhaust flow period. However, as the spark timing is further retarded, from -1° to -6° BTDC, CO levels observed at the port exit increase to approximately 1%. There are several plausible mechanisms for the changes in CO levels observed in Fig 4.8; port oxidation rates, port residence time, and in-cylinder air-fuel non-uniformities.

The last row of graphs in Fig. 4.8 depicts port exit HC concentrations decreasing as combustion was phased later in the engine cycle. Baseline spark timings yield HC concentrations on the order of 3000 ppm_{C1} and decline with increasing spark retard. However, recall that as spark timing was retarded, the mass flow rate through the engine increases to maintain the same torque output. Thus, a decrease in HC concentration could be offset by an increase in HC mass emissions.

4.3.2 CUMULATIVE CO AND HC MASS EMISSIONS

In order to investigate the impact of late combustion phasing, cumulative feed gas emissions were evaluated from the first second to the twentieth second following engine startup. Cumulative emissions were calculated based upon a simple plug flow model outlined in Sec. 3.5. Instantaneous mass flow rates and exhaust gas temperature predicted by the multi-cylinder engine simulation are shown in Figs. 4.9. Cumulative HC and CO mass emissions as a function of spark timing modifications is shown in Fig. 4.10. Port exit emissions from cylinder no. 4 were scaled by a factor of four for comparison to converter-in levels. Port exit CO emissions reached a minimum following the baseline calibration and then increased with additional spark retardation. Port exit HC emissions were also observed to increase linearly with spark retardation. Converter-in emissions contained emission levels from all four cylinders.

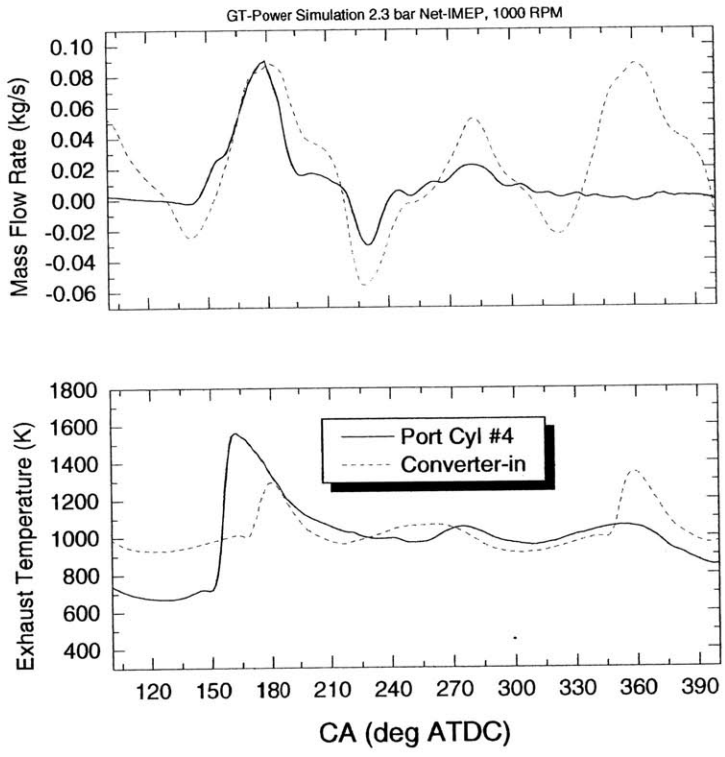

Figure 4.9 Cylinder no. 4 exhaust port and converter-in mass flow rates and exhaust gas temperatures as a function of engine crank angle (CA). Data predicted by the engine simulation for baseline timing and fueling calibration under idle load and speed conditions.

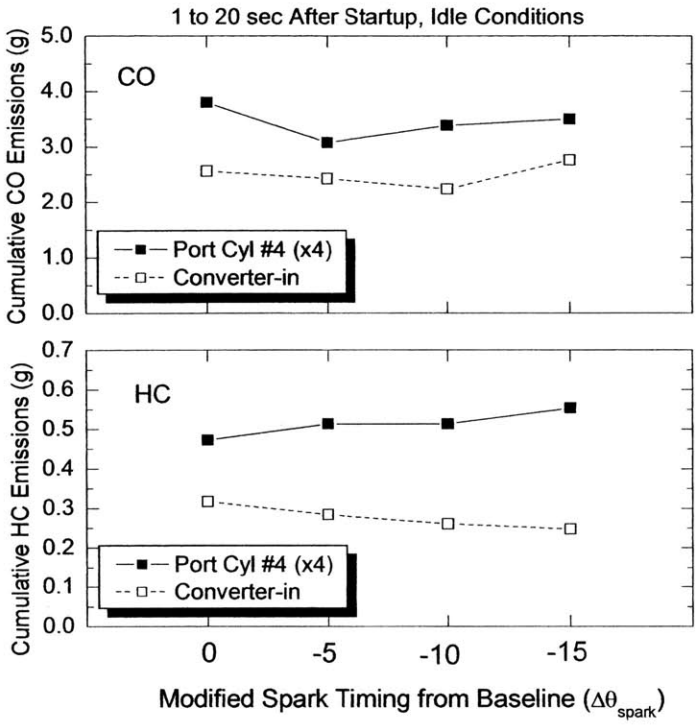

Figure 4.10 Cumulative, 1 to 20 seconds, ambient startup CO and HC mass emissions measured at the exhaust port exit of cylinder no. 4 and converter-inlet as a function of modified spark timing under idle speed and load conditions (Port exit emissions are scaled by a factor of 4 for comparison to converter-in levels).

4.3.3 CYLINDER-TO-CYLINDER MALDISTRIBUTION

The multi-cylinder engine was subject to cylinder-to-cylinder variations in air flow and fuel injection. These imbalances led to cylinder-to-cylinder fuel maldistriubtion and in-cylinder fuel stratification, resulting in higher HC and CO emissions. Incomplete mixing of fuel and air within each cylinder also led to differences in residual gas composition [14,15]. Equilibrium concentrations of the main exhaust gas species (CO, CO_2, H_2O, H_2, and O_2) is a function of air/ fuel ratio. For a stoichiometric mixture, CO_2 concentration reached a maximum with negligible concentrations of O_2 and CO. Rich of stoichiometric, CO concentration increases linearly with increasing equivalence ratio. Likewise, lean of stoichiometric, O_2 concentrations increase linearly with decreasing equivalence ratio. Therefore, fuel maldistriubtion was indicated by CO_2 concentration and the linear combination of CO and O_2 concentrations. Utilizing the fast-response NDIR instrument, exhaust port exit CO and CO_2 concentrations were quantified under

stoichiometric engine operation. Figure 4.11 shows in-cylinder pressure, CO, CO_2, and CO + CO_2 concentrations for cylinders no. 3 and no. 4 for a spark timing of 3° BTDC under idle speed and load conditions.

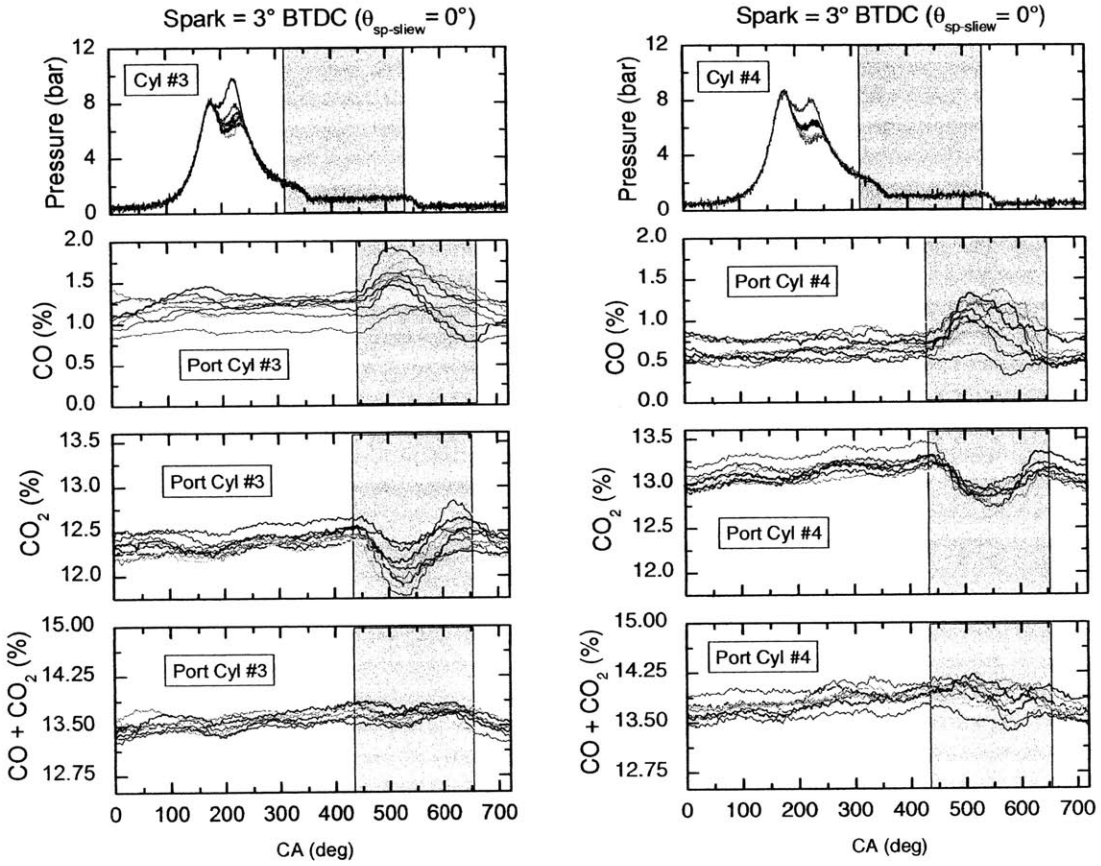

Figure 4.11 Cylinders no. 3 and no. 4 in-cylinder pressure, CO, CO_2, and CO + CO_2 time-resolved concentrations measured at the exhaust port as a function of crank angle (CA). Data shown from cycle 200 to 210 after startup, absolute spark timing 3° BTDC, stoichiometric closed loop control, and idle speed and load conditions (2.3 bar Net-IMEP, 1000 RPM, λ = 1.0).Grayed areas show period of exhaust flow.

The grayed areas of in Fig. 4.11 show the period of exhaust flow with an observed increases in CO concentrations from cylinder no. 3 compared to cylinder no. 4, CO + CO_2 was plotted for each cylinder to check the balance of carbon. Port exit HC emissions for cylinders no. 3 and no. 4 were observed to vary by approximately 500 ppm_{C1} during the exhaust flow period, Fig. 4.12.

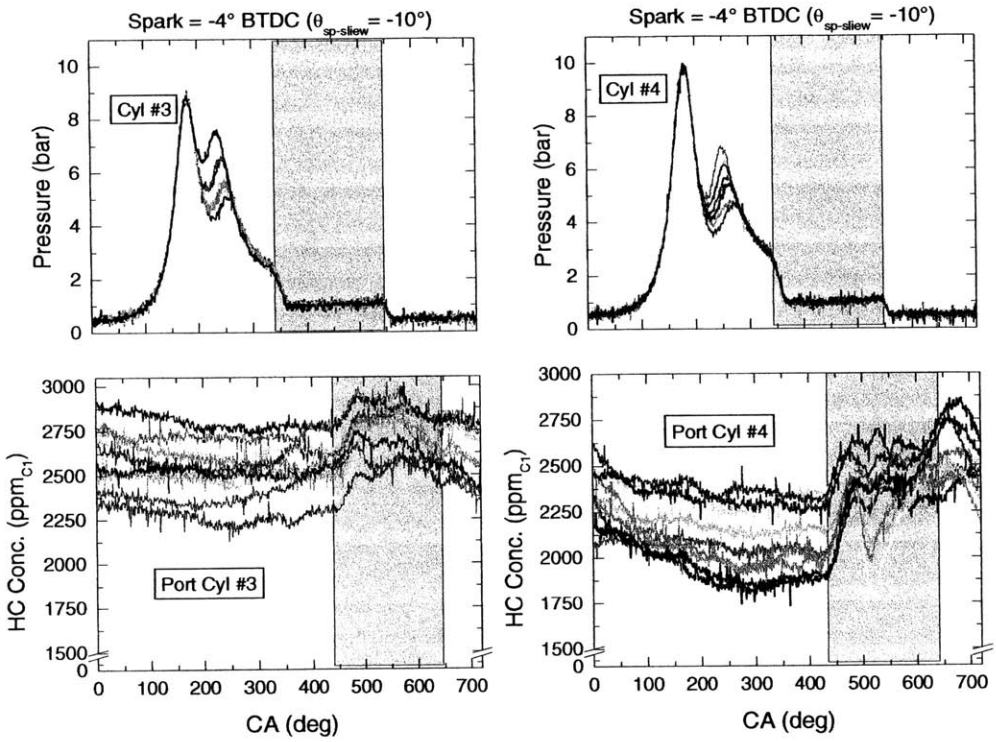

Figure 4.12 Cylinder no. 3 and no.4 in-cylinder pressure and port exit time-resolved HC concentrations as a function of crank angle (CA). Data shown from cycle 200 to 210 after startup, absolute spark timing -4° BTDC, stoichiometric closed loop control, and idle speed and load conditions (2.3 bar Net-IMEP, 1000 RPM, λ = 1.0).Grayed areas show period of exhaust flow.

Data from the time-resolved CO and CO_2 measurements was used to estimate cylinder-to-cylinder relative air-fuel ratio. Figure 4.13 shows cylinder no. 3 and no. 4 port exit exhaust gas temperature (EGT) and relative air-fuel ratio (λ) as a function of spark timing. Each cylinder's relative air-fuel ratio was calculated from exhaust gas equilibrium concentrations of CO and CO_2, see Fig. 4.14. Cylinder no. 4 was observed to runner slightly lean of stoichiometric and have the highest measured port exit EGT.

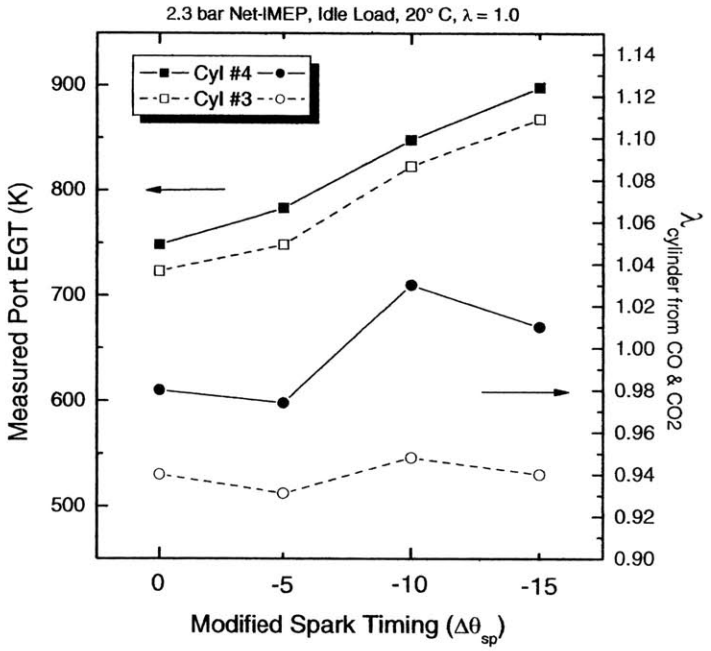

Figure 4.13 Port exit measured exhaust gas temperatures and relative air/fuel ratios (λ) calculated from time-resolved CO and CO_2 measurements for cylinders no. 3 and no. 4 as a function of modified spark timing. Data shown for idle load and speed conditions under closed loop stoichiometric control.

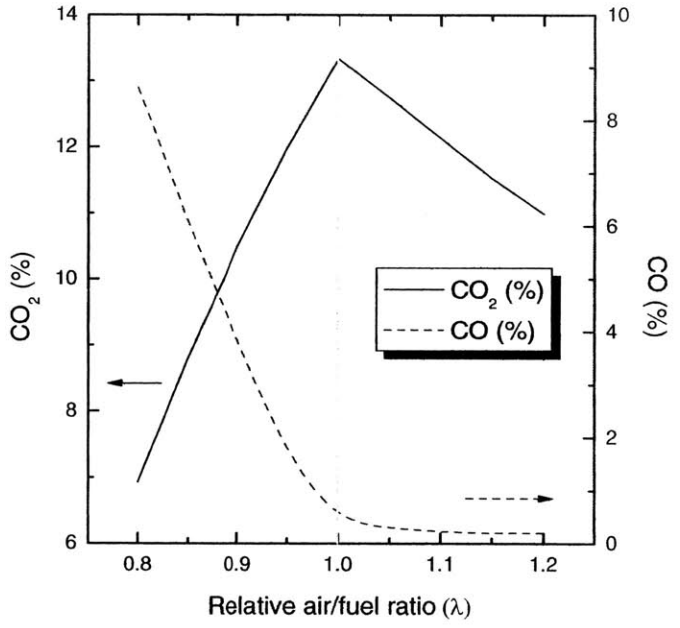

Figure 4.14 Spark-ignition engine exhaust gas CO_2 and CO concentration data as a function of relative air/fuel ratio.

Relative air-fuel ratio non-uniformities and HC emissions were investigated at the collector inlet as a function of manifold air pressure (MAP) under stoichiometric operation, Fig. 4.15. The fuel maldistriubtion parameter, CO + O_2, was corrected for hydrocarbons and was observed to increase with increasing MAP. Hydrocarbon emissions, expressed as a fraction of the fuel injected, decreased with increasing MAP. Figure 4.15 suggests that with increasing MAP (and increasing spark retardation) mixture preparation worsens and results in an increases in cylinder-to-cylinder air-fuel variations under idle speed and load conditions.

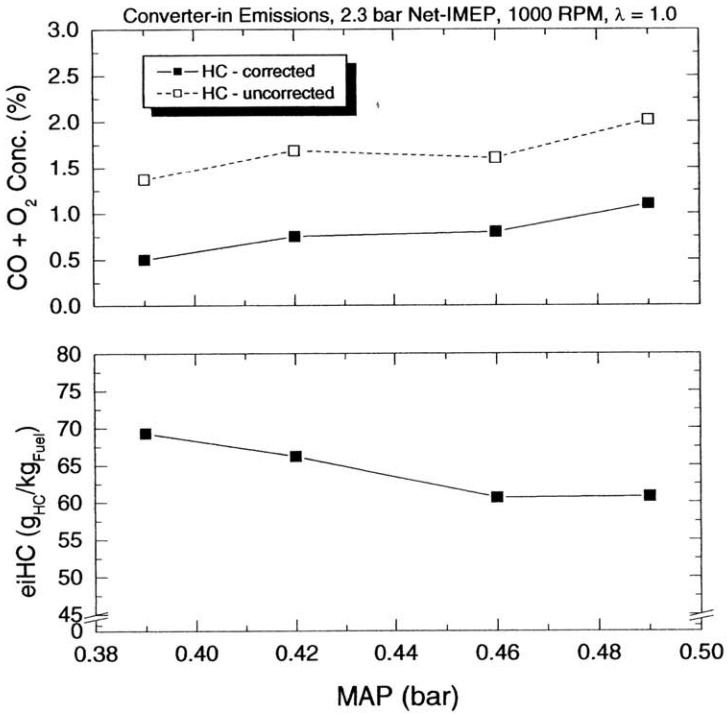

Figure 4.15 Converter-in CO + O_2 emissions and emission index HC levels as a function of intake MAP. Data shown for stoichiometric closed loop control and 20° C idle speed and load conditions (2.3 bar Net-IMEP, 1000 RPM, λ = 1.0). CO+O_2 concentration shown with and without oxygen concentration corrections due to HC emissions.

4.4 EXHAUST FEED GAS AND LIGHT-OFF

4.4.1 FEED GAS EMISSIONS AND ENTHALPY

Exhaust gas temperatures were measured at the exit of the exhaust port at all four cylinder, Fig. 4.16. In addition, converter-in and converter-out EGTs, brick temperatures, and skin temperatures were recorded for the first 20 seconds of engine operation. During this time period, metal skin and component temperatures were observed to vary less than 20° C.

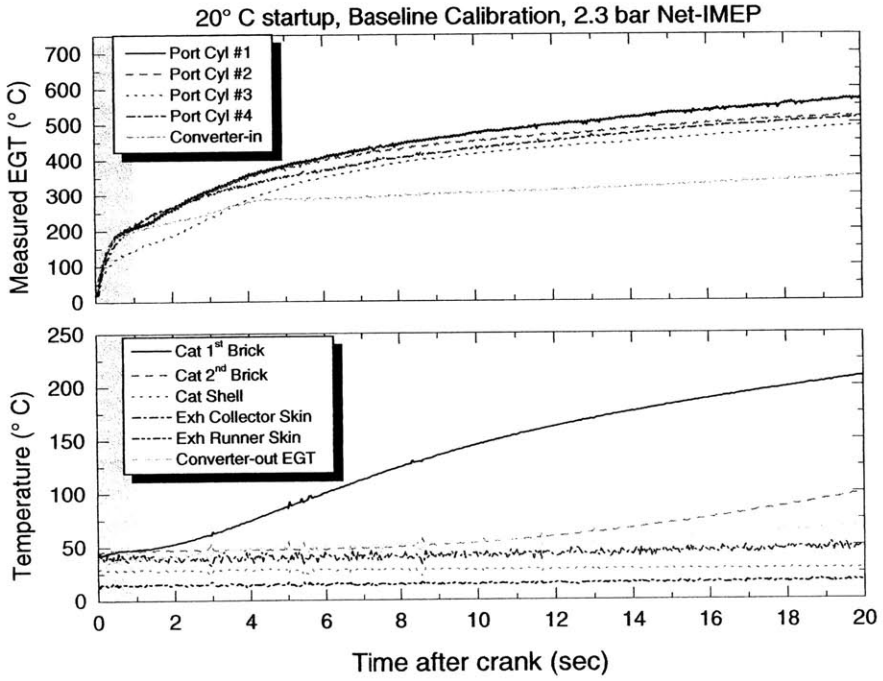

Figure 4.16 Measured exhaust gas and component temperatures as a function of time after crank. Data shown for baseline timing and fueling calibration under idle load and speed conditions.

Cumulative converter-in feed gas HC emissions as a function of cumulative sensible enthalpy for four different spark modifications was investigated from second 1 to 20 following an ambient (20° C) startup. With the most aggressive retarded spark modification ($\Delta\theta_{spark}$ = -15°), sensible enthalpy supplied to the catalyst was increased by a factor of three and HC emissions were reduced by 23%, Fig. 4.17.

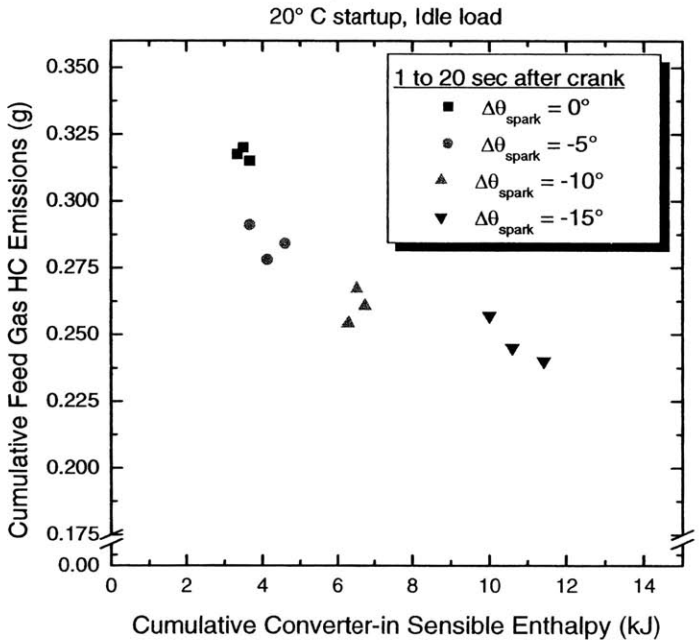

Figure 4.17 Cumulative converter-in feed gas HC emissions as a function of cumulative converter-in sensible enthalpy. Data shown for 1 to 20 seconds following an ambient startup for four spark timing modifications ($\Delta\theta_{sp}$) under idle speed and load conditions.

4.4.2 CATALYST LIGHT-OFF TIMES

A decrease in exhaust gas temperature can be offset by an increase in oxygen concentration of the feedgas which has a large impacts on the low-temperature activity of the catalyst. The 50% light-off temperature was observed to decreased greatly with late ignition timings. Lean relative air/fuel ratio reduces engine-out hydrocarbons but increases combustion instability. Increased oxygen concentration in the feedgas has been to have a favorable effect on lowering the catalyst light-off temperatures with catalysts having a high Pd content [22]. However, lean mixtures require advancement of ignition timing which results in lower exhaust gas temperatures.

Cumulative feed gas HC emissions versus catalyst light-off time was investigated for various late spark timings, Fig. 4.18. Catalyst light-off was defined as the 50% conversion efficiency of hydrocarbons (η_{HC} = 50%). Light-off experiments were conducted with a 50k mile aged ULEV catalyst (serial no: XX901JP). Hydrocarbon concentrations were monitored pre-

catalyst and post-catalyst utilizing the fast-response FID analyzer. Compared to the baseline spark timing ($\Delta\theta_{spark}$ = 0°), engine operation with aggressive spark retardation ($\Delta\theta_{spark}$ = 15°) reduced cumulative converter-in HC emissions, prior to catalyst light-off, by 40% and decreased light-off times by approximately 5 seconds.

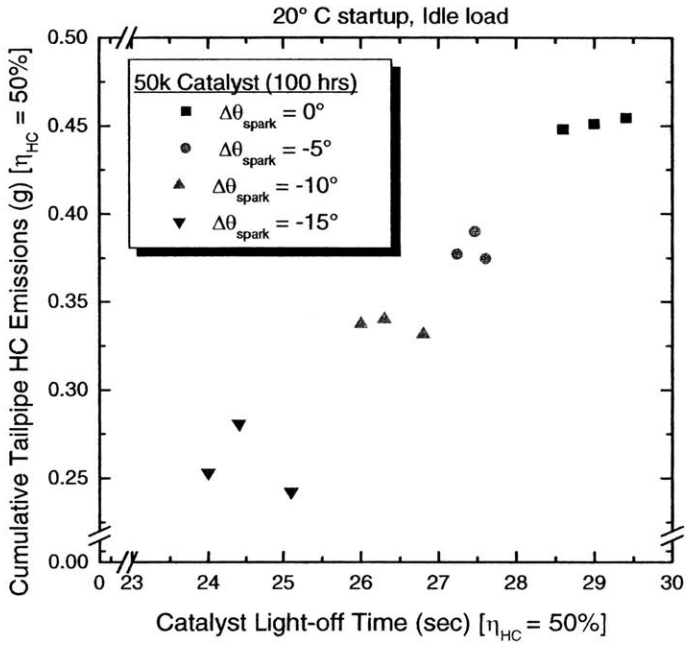

Figure 4.18 Cumulative HC mass emissions prior to catalyst light-off as a function of light-off time following an ambient start. Data shown for various spark modifications ($\Delta\theta_{sp}$) under idle speed and load conditions (Light-off defined as 50% reduction in HC emissions).

CHAPTER 5

EXHAUST SYSTEM MODEL

5.1 OVERVIEW

Time-resolved cylinder-exit exhaust gas temperature, velocity, and mass flow rate histories were required for the modeling investigation. The thermodynamic state of exhaust gas was difficult to measure experimentally therefore, a cycle simulation and exhaust flow simulation was used to determine the gas state. The exhaust system was modeled as 1-D quasi-steady compressible flow, additional details are provided in Sec. 3.5.2. Exhaust gas composition was estimated from stoichiometry and direct measurements of exhaust CO_2, CO, and HC concentrations. The predicted and measured parameters were used as inputs to drive a plug flow model of the exhaust system. Exhaust flow, heat transfer, and a detailed chemical kinetic mechanism were coupled to predict exhaust oxidation as a function spark timing and relative air/ fuel ratio, Fig. 5.1. The oxidation model employed a two zone, exhaust port and runner, system, each zone had a specific exhaust geometry and heat transfer correlation, Fig. 5.2.

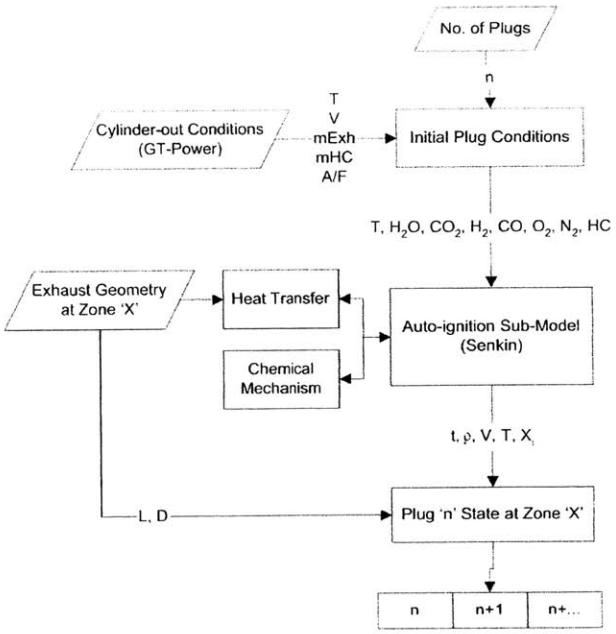

Figure 5.1 Plug flow exhaust oxidation sub-model flowchart with linked engine predicted cylinder-exit conditions, heat transfer, and chemical kinetic mechanism.

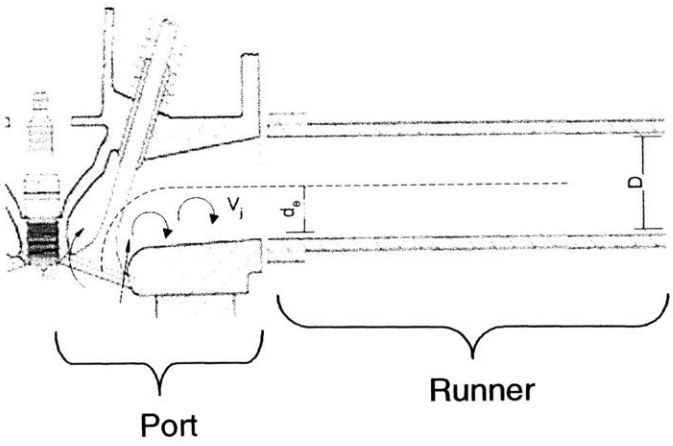

Figure 5.2 Diagram of exhaust port and runner zones.

5.2 PLUG FLOW SUB-MODEL

5.2.1 MASS ELEMENTS

Plug flow was used to model the transport and chemical reactions of exhaust gas from cylinder-exit to converter-in. The systems was characterized by linear flow rates without zones of recirculation. Cylinder-exit gas out flow was discretized into two constant mass elements, Fig. 5.3. The first element contained mass expelled during the compressible blowdown period (EVO to 25° ABDC) and the second mass element held mass from the incompressible displacement period (26° ABDC to EVC). Each element was an isolated moving control volume with infinitely fast mixing; uniform properties with no temperature, pressure, or concentration gradient. The center of mass and evolution of species were tracked and the linear distance traveled by each mass element was converted to time from bulk momentum averaged velocity measurements predicted by the engine simulation. As each mass segment evolved, heat transfer to the inner pipe wall was modeled, but no interactions were allowed between elements, Fig. 5.4.

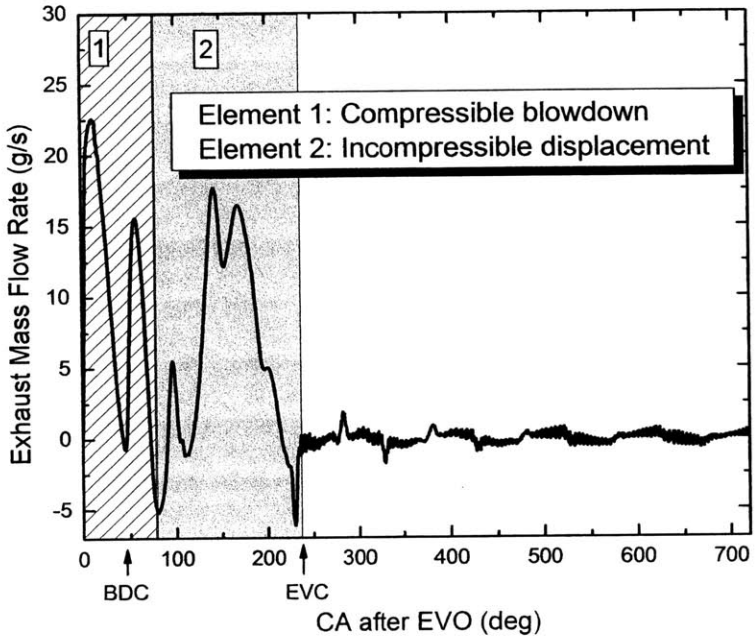

Figure 5.3 Simulation of single-cylinder exhaust mass flow versus crank angle after exhaust valve opening. Exhaust mass modeled using two elements; mass from compressible blown process and mass from incompressible displacement.

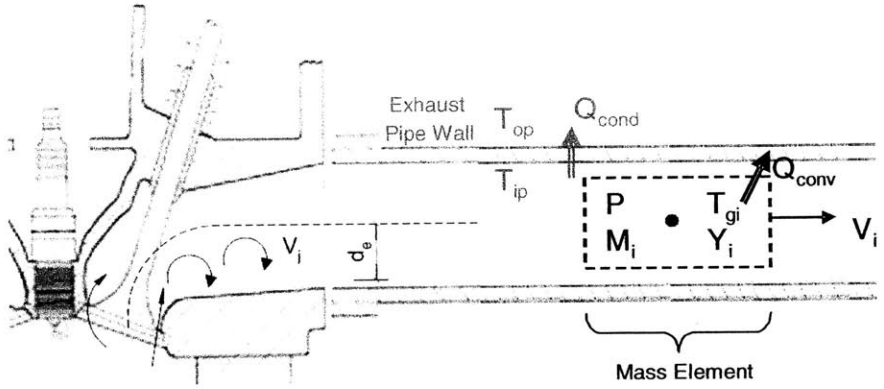

Figure 5.4 Mass element model details.

5.2.2 INITIAL CONDITIONS

An engine-exhaust simulation generated crank angle (time) histories of mass flow rate, velocity, and temperature for various engine conditions and exhaust locations. The results were discretized into two mass elements, Fig. 5.5. Each element had an enthaplic temperature (Eq.

F.1.2), momentum averaged velocity (Eq. F.1.3), and exhaust gas composition obtained from the HC tracking experiments and estimations based on stoichiometry and carbon monoxide (CO) and carbon dioxide (CO_2) measurements.

Exhaust quenching experiments quantified cylinder-exit HC emissions. However, unlike the time-resolved port and runner measurements, quenching experiments provided an integrated total. Therefore, cylinder-exit emissions were assumed to have the same profile, but different magnitude, of HC emissions as the time-resolved exhaust port measurements. Likewise, exhaust gas hydrogen (H_2) levels were estimated from CO concentrations, Fig. F.1.1. The highly diluted reactive mixture contained N_2, CO_2, H_2O, O_2, CO, H_2, HC, and combustion radicals, Fig. 5.6. These initial conditions and compositions were used to drive the exhaust plug flow oxidation model.

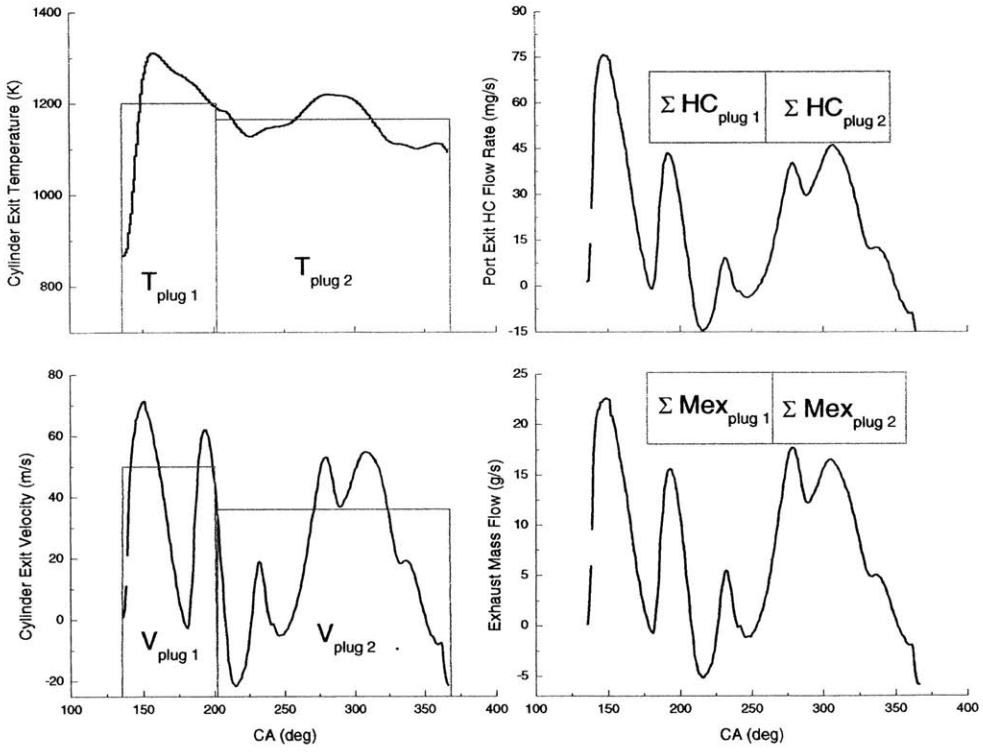

Figure 5.5 Cylinder-exit initial conditions for plug flow model. Data shown from engine simulation predictions and experimental results.

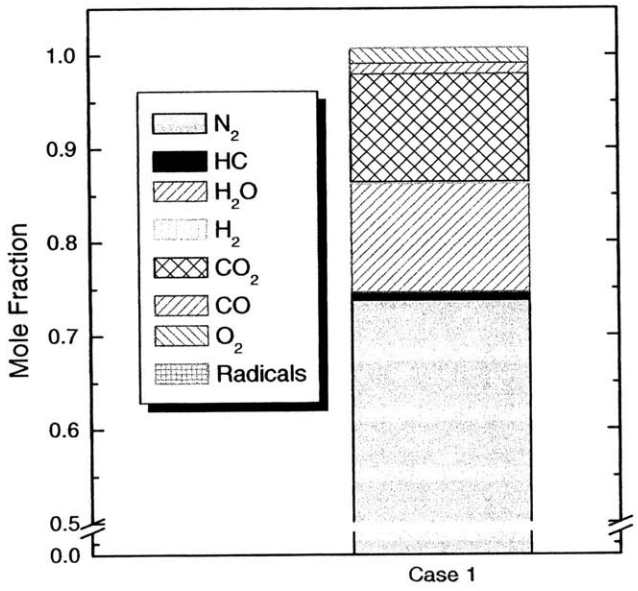

Figure 5.6 Mole fraction of exhaust gas composition for highly diluted reactive mixture of hydrocarbons.

5.3 EXHAUST SYSTEM HEAT TRANSFER SUB-MODEL

5.3.1 OVERVIEW

Heat transfer was separated into two zones exhaust port and exhaust runner region. The exhaust port contained regions of complex flows and heat transfer processes. In order to simplify the analysis, convective exhaust port heat transfer was approximated as quasi-steady and 1-D, Eq. F.2.5. Exhaust port and runner heat transfer was perpendicular to wall surfaces and circumferentially uniform. Exhaust component wall temperature fluctuations during the exhaust blowdown period were assumed to have a negligible impact. Therefore, time-averaged port and runner outer wall temperatures was measured, Fig. 5.7, and conductive heat transfer from the inner to outer pipe layer was calculated, Eq. F.2.6.

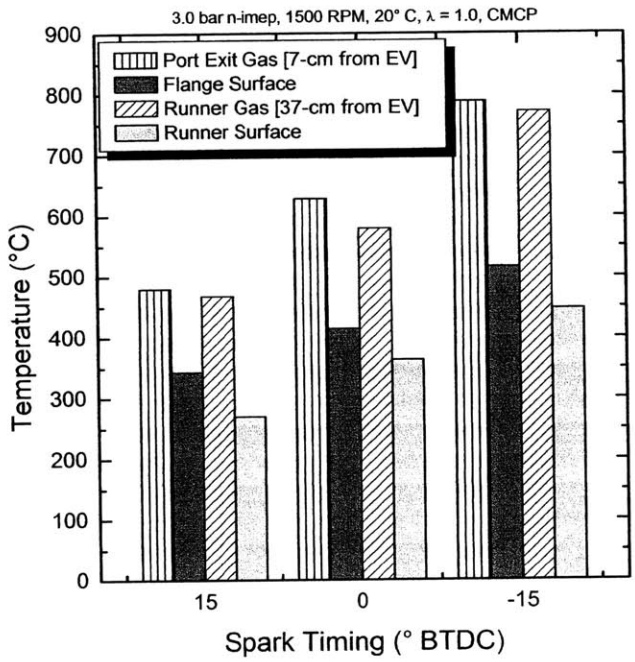

Figure 5.7 Thermocouple measured exhaust gas and component temperatures for 15°,0°, and -15° BTDC spark timings. Steady-state warmed-up exhaust system with 20° C fluids, 3.0 bar Net-IMEP, 1500 RPM, and $\lambda = 1.0$.

Depending upon the exhaust valve lift, different mechanisms governed the heat transfer process in the exhaust port. Caton *et al.* [26] noted exhaust port heat transfer for the blowdown process (low valve lift) was dominated by large scale motion and approximated as convergent, conical jet flow. High jet velocities produced large scale eddies in the exhaust port, that scaled approximately with half the port's diameter. [26]. The Nusselt number (Nu) was calculated from a simple power law empirical correlation using the Reynolds number (Re) based on half of the port's diameter and a Prandtl number (Pr) of 0.65. During the exhaust displacement period, the Nusselt number was established from turbulent pipe flow correlations (Pr = 0.65) with empirical constants C1 and C2 for developing flow and pipe roughness. A summary of exhaust port Nusselt number correlations used during the two exhaust periods is shown in Table 5.1.

Table 5.1 Nusselt number correlations for exhaust blowdown and exhaust displacement period [26].

Exhaust Port	
Exhaust Period	Nusselt No.
Blowdown	$Nu_1 = 0.4*Re_j^{0.6}$
Displacment	$Nu_2 = 1.0\{0.0194*C1*C2*Re_D^{0.8}\}$

5.3.2 EXHAUST RUNNER

Previous investigation observed that large scale motion was not a significant feature 3 valve diameters downstream from the exhaust valves [26]. Therefore, an empirical convective heat transfer coefficient for the exhaust runner was calculated using a Nusselt-Reynolds number correlation for turbulent, fully developed pipe flow. Effects of exhaust pulsations and pipe bends were accounted for by augmenting factors F_{pulse} and F_{bend}, respectively, and used to modify the Nusselt number, Table 5.2 [27].

Table 5.2 Nusselt number correlations for exhaust runner with argument factors pulses and pipe bends [26, 27].

Exhaust Runner
$Nu_{runner} = 1.0\{0.0194*C1*C2*Re_D^{0.8}\}$
$1.6 \leq F_{pulse} \leq 3.0$
$F_{bent} = \frac{Nu_{bent}}{Nu} = 1 + \frac{21d_i}{Re^{0.14}d_{bent}}$

5.3.3 AVERAGE EXHAUST HEAT TRANSFER COEFFICIENT

The average exhaust port and runner heat transfer coefficients for mass elements expelled during the blowdown and displacement process are given in Fig. 5.8. Port heat transfer coefficient was approximately twice that of the runner for TDC and after ignition timings. Higher engine mass flow rates with late combustion phasing, resulted in higher velocities and increased exhaust heat transfer coefficients.

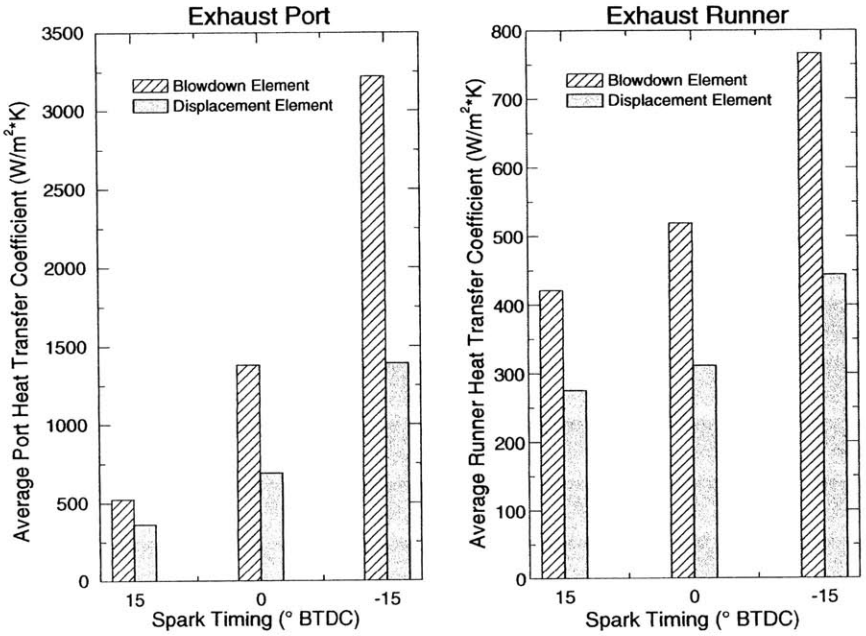

Figure 5.8 Average port (left) and runner (right) heat transfer coefficient as a function of spark timings. Data shown for mass elements from exhaust blowdown and displacement process.

5.3.4 EXHAUST HEAT TRANSFER MODEL VALIDATION

After modeling the cylinder-exit temperatures, energy released from exhaust HC burn-up was added as an internal heat source per unit length (W/m^2) to the port and runner, Fig. 5.9. Experimental thermocouple measurements provided time-averaged exhaust gas temperatures at the port exit and runner. Utilizing the engine-exhaust simulation's instantaneous enthalpic gas temperatures, the response of the thermocouple sensors were modeled, Fig. 5.10. An energy balance was derived for the model assuming lumped capacitance with convective heat transfer dominating, Eq. F.2.4. For the multi-cylinder engine undergoing a transient startup, the dominant heat transfer rate to the thermocouple was controlled primarily by the Reynolds number. The thermocouples were observed to have a first-order time constant with a response time (10-90%) of approximately 1 second. The response of the thermocouples was estimated from crank angle resolved enthalpic temperature data from the model. Port and runner exhaust system heat transfer multipliers, C1 and C2, and augmentation factors, F_{pulse} and F_{bend}, were adjusted until agreement within $\Delta T = 50$ K was achieved between temperatures predicted by the time-averaged

thermocouple sensor model and direct time-averaged temperature measurements from the experiments, Fig. 5.11.

There were several possible sources of error with the steady-state experimental temperature measurements including: radiation losses, end conduction losses, and kinetic energy gains. Only losses due to radiation were taken into account using the model simulation. The measured temperatures were obtained by utilizing radiation shielding, thus minimizing losses (ΔT = 10 K). Previous investigations by Caton *et al.* noted that heat transfer losses due to condition of the wires and kinetic energy can produce measurement errors, but the combined effect was found to be less than 10 K under similar engine operating conditions [26].

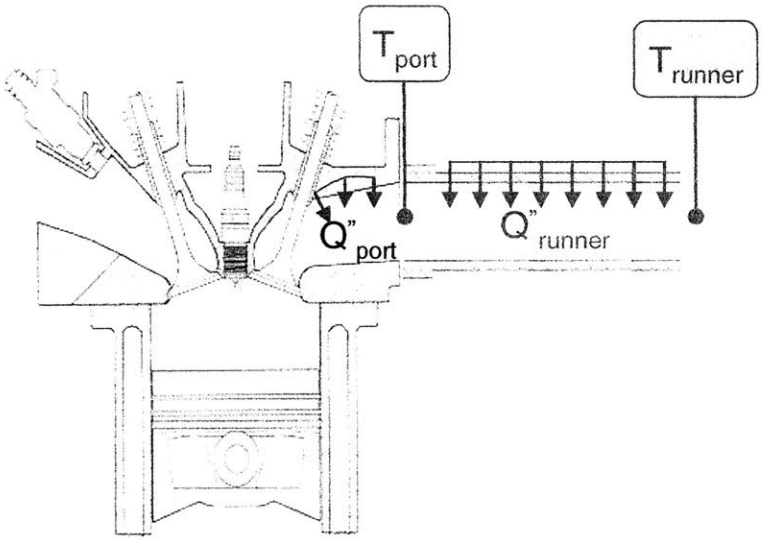

Figure 5.9 Schematic of exhaust port and runner temperature validation of heat transfer sub-model. Exhaust port and runner HC oxidation modeled as a heat addition per unit length. Thermocouple modeled exhaust gas temperature at port exit and runner.

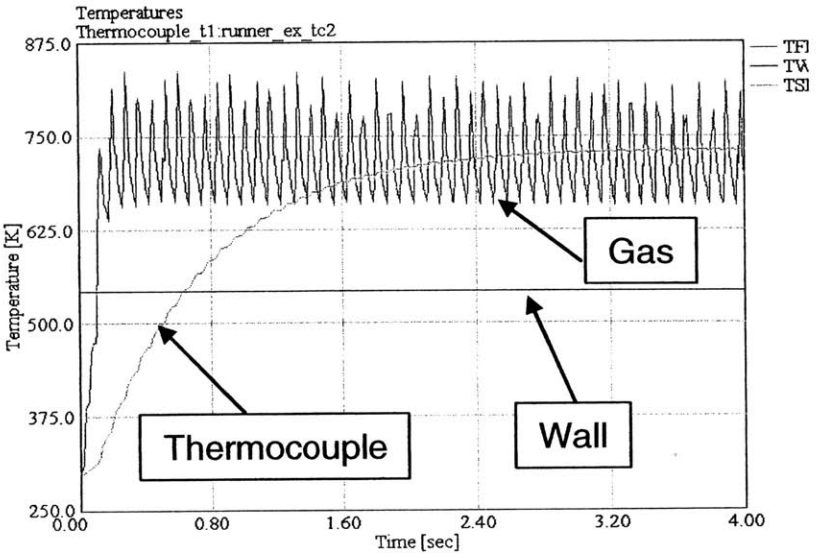

Figure 5.10 Instantaneous exhaust gas, runner wall and thermocouple temperature as a function of time. Thermocouple response data shown for hot exhaust component temperatures.

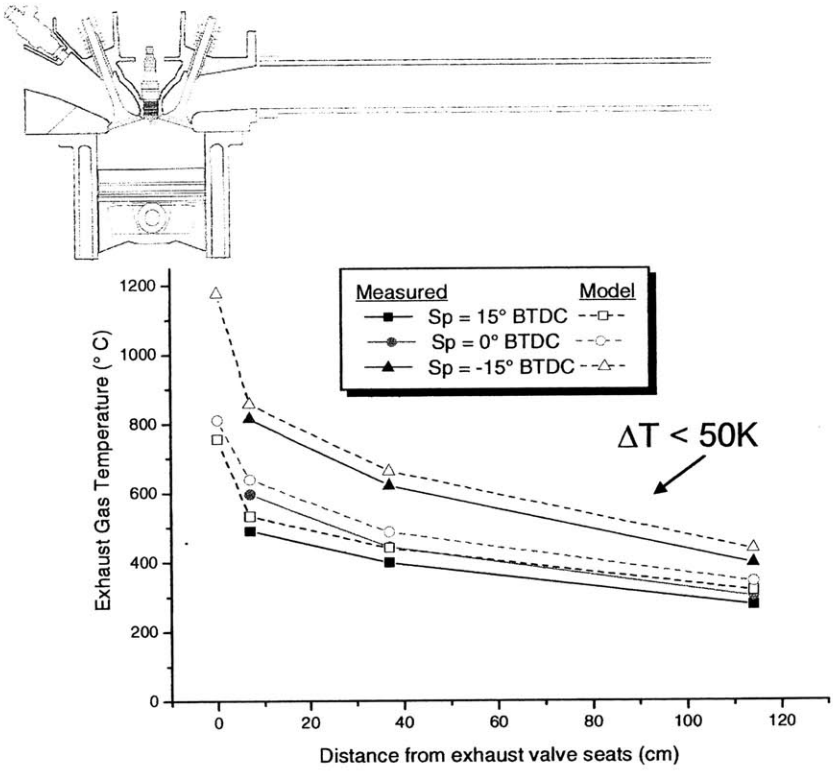

Figure 5.11 Thermocouple exhaust gas temperatures, measured versus modeled, for various spark timings. Comparison includes heat released due to exhaust system HC burn-up.

5.4 HYDROCARBON OXIDATION SUB-MODEL

5.4.1 OVERVIEW

During the combustion process in a spark-ignition engine, a small fraction of the fuel is not burned during flame propagation and is stored in cold wall layers (crevices, deposits, oil films and quench layer). These hydrocarbons emerge from different sources and mix with burned gases during the expansion and exhaust process. Throughout the cold-start phase, over 100 HC species of various molecular size, have been identified in exhaust gas. Speciated HC emissions for the first 63 seconds following a cold-start from a SI engine fueled with Japanese domestic gasoline is shown in Fig. 5.12.

Exact HC composition depends highly upon the fuel composition, air/fuel ratio, and engine coolant temperature, but cold-start emissions have generally observed a higher weight percentage of methane during the initial period following startup [16,17]. Weight percentages of various hydrocarbons (methane, acetylene, and C_2 and C_4 olefins) were also observed to vary throughout the engine warm-up period, Fig. 5.13. Kaiser *et al.* suggested that paraffins, olefins, and naphthalenes fuel species were converted to low molecular weight, C_2 - C_4, olefins by C-C bond scission via thermal decomposition and/or H-atom abstraction during the blowdown exhaust process [17,18]. These olefins were found to be highly reactive, thus exhaust gas reactivity increases as the warm-up progresses [17]. Additional HC variations have been attributed to changes in air/fuel ratio during startup, with insufficient oxygen levels promoting the formation of methane and acetylene [18].

5.4.2 HYDROCARBON SPECIES

Previous investigations have reported that cold-start engine exhaust gas HC species can be represented as mixture of 10 wt-% methane (CH_4), 30 wt-% n-pentane (C_5H_{12}), 30 wt-% ethylene (C_2H_4), 20 wt-% toluene (C_7H_8), and 10 wt-% other species [16-18]. Therefore, a reactive mixture of these HC was selected to represent the unburned composition with the following mole fractions: 44 mol-%, C_2H_4, 26 mol-% CH_4, 17 mol-% C_5H_{12}, 9 mol-% C_7H_8, and 4 mol-% of iso-octane (2,2,4-trimethylpentane, C_8H_{18}).

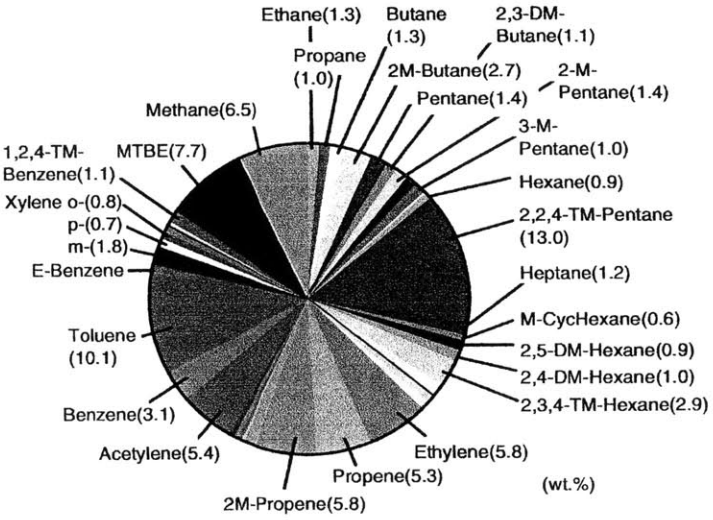

Figure 5.12 Cold-start SI engine-out speciated HC emissions for initial 63 seconds of engine operation using Japanese domestic fuel. Source: Yamamoto *et al.* [16].

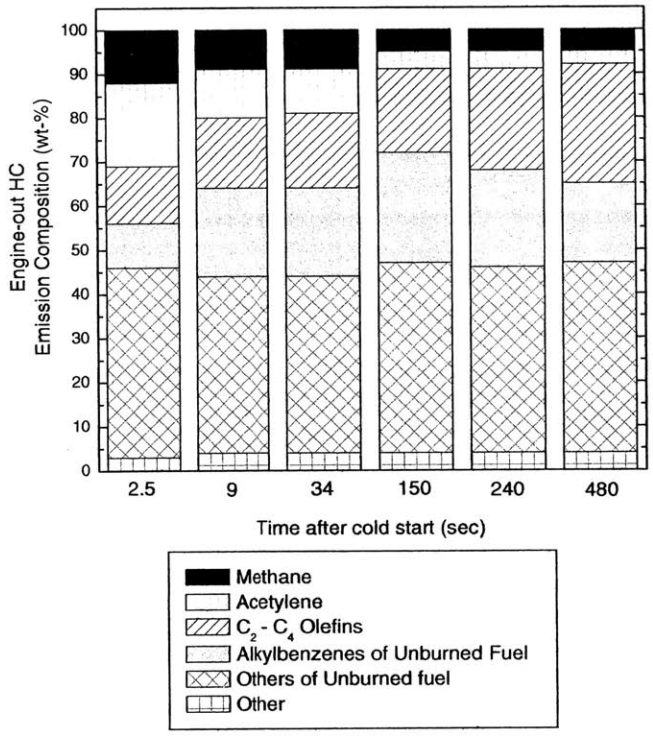

Figure 5.13 Variation in engine-out hydrocarbon composition as a function of time during warm-up. Source: Kubo *et al.* [17].

5.4.3 CHEMICAL KINETIC MECHANISM

A detailed chemical kinetic mechanism with elementary reactions was selected to model the hydrocarbon oxidation process. Comprehensive reaction mechanisms for toluene and iso-octane were obtained from literature and combined to simulate hydrocarbon oxidation [24,25]. Each mechanism was validated with experimental data over a wide range premixed and non-premixed conditions with initial pressures, temperatures, and equivalence ratios similar to those observed in an engine exhaust system (1-45 bar, 550 - 1700K, and ϕ = 0.3 - 1.5). The combined mechanisms contained 973 species and 3849 reactions and was used to model the highly diluted autoignition chemistry.

The autoignition mechanisms contained low and high temperature pathways for the oxidation of hydrocarbons. The low temperature mechanism was more complex than the high temperature pathway Fig. 5.14. Low temperature ignition was initiated by H-atom abstraction or decomposition of the parent fuel (RH) and forms alkyl radicals (R) which react with O_2 to form alkyloperoxy radicals (ROO). These radicals underwent isomerization (internal H-atom transfer) forming hydroperoxy alkyl radicals (QOOH). Another O_2 addition step led to the formation of hydroperoxyalkylperoxy radicals (OOQOOH). Chain branching was initiated as an additional isomerization led to the formation of carbonyl hydroperoxides (O=R'OOH) and OH radicals. Further decomposition of carbonyl hydroperoxides yields carbonyl radicals (O=R'O) and OH radicals. At higher temperatures, ROO decomposed back into O_2 and R. Hydroperoxy radicals (HOO) were formed by O_2 addition to H-atoms resulting from hydrogen abstraction. Recombination of HOO radicals resulted in the formation of hydrogen peroxides (HOOH). At high temperatures, the pool of hydrogen peroxide (HOOH) decomposes yielding two OH radicals. The relatively large concentration of OH radicals was response for the first autoignition stage of hydrocarbons.

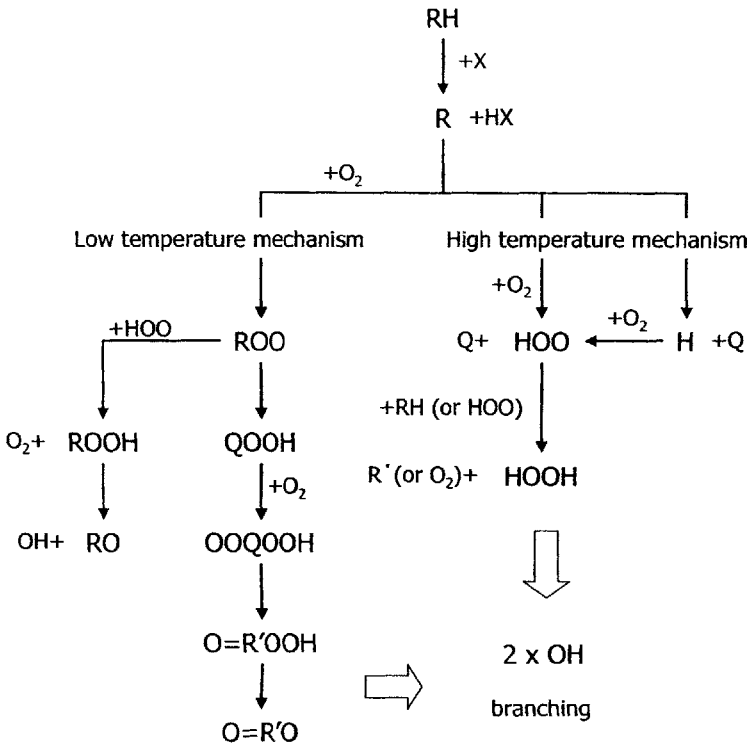

Figure 5.14 Hydrocarbon oxidation pathways.

5.4.4 CHEMICAL KINETIC MODEL

Combustion simulations were conducted with Chemkin-II software package. Chemkin is composed of the interpreter, the thermodynamic database, the linking file, and reaction mechanism, Fig. F.3.1. The forward and reverse reaction rates for each reaction and thermodynamic database for the species were taken from the toluene and iso-octane literature. [24,25]. The plug flow model used a zero-dimensional program called Senkin. The Senkin application of Chemkin-II predicted homogenous gas-phase chemical kinetic by solving a system of time dependent energy and species conservation ordinary differential equations [23]. The program computed the time evolution of the homogenous gas mixture in a closed system at constant pressure (~1.013 bar). The adiabatic treatment of the gas mixture (energy equation, Eq. F.3.1) was modified in Fortran to include the heat transfer sub-routine outlined in Sec. 5.3.4.

5.4.5 BURNT GAS RADICAL CONCENTRATION

Burnt gases contained radicals that were critical in the attack of hydrocarbons. Key radicals such as hydroxyl (OH) radical, hydrogen atom (H), oxygen atom (O), hydroperoxy radical (HOO), and hydrogen peroxide (HOOH) are responsible for chain branching, chain propagating, and initiating steps as outlined in Sec. 5.4.3. Therefore, the mass exiting the cylinder was assumed to contain a homogeneous mixture of unburned and burned gas, with burned gas contained radical that underwent the time temperature and pressure histories during the expansion stroke, Fig. F.3.4. Cylinder volume as a function of time during the expansion stroke was used to estimate the initial super-equilibrium radical concentrations present in burnt gases. Initial pressure and temperature were obtained at the end of the combustion process and the simulation provide an order of magnitude estimate for the initial radical concentrations in the exhaust gas at the time of exhaust valve openening (EVO).

CHAPTER 6

MODELING RESULTS

6.1 SINGLE-CYLINDER ENGINE

6.1.1 EXHAUST PORT AND RUNNER OXIDATION

A summary of results from single-cylinder HC tracking and exhaust gas temperatures measurements for various spark timings and relative air/fuel ratios is shown in Figs. 6.1 and 6.2. These results were compared to the oxidation model predictions for various spark timings and relative air/fuel ratios, Figs. 6.3-6.6. The unburned mixture from HC sources, crevice volumes, wall quenching, deposits, and oil layer, were assumed to contain the oxygen and nitrogen characteristic of the overall relative air/fuel ratio. The reactive mixture was highly dilute with burned gases containing super-equilibrium concentration of radicals formed during the expansion process.The computation starts at exhaust valve openening with a specified initial composition and temperature of the homogeneous mixture at constant pressure. The chemistry sub-model contained detailed chemical reactions and evolution of all species were tracked. Total HC concentrations (ppm_{C1}) was obtained by summing the total mole fraction of species containing carbon (C_1) excluding carbon monoxide (CO) and carbon dioxide (CO_2) and is reported as the fraction of hydrocarbon oxidized (R) in the port or runner. Generally, agreement between the port and runner oxidation observed in the experiments and oxidation predicted by the model was better than 30%.

Measured and mass averaged (enthalpic) predicted temperatures for the exhaust port oxidation are also shown in Fig. 6.3-6.6. Previous investigations have indicated that mass-averaged (enthalpic) temperatures are generally 10-15% higher than the time averaged temperatures obtained with thermocouple sensors [31]. Agreement was achieved between the model and experiments. Coupling of gas temperature (governed by the heat transfer sub-routine) and the rate of gas-phase chemical kinetics will be investigated in the sensitivity section. However, high gas temperatures ensured the low temperature mechanism pathway and the negative temperature coefficient (NTC) region were avoided.

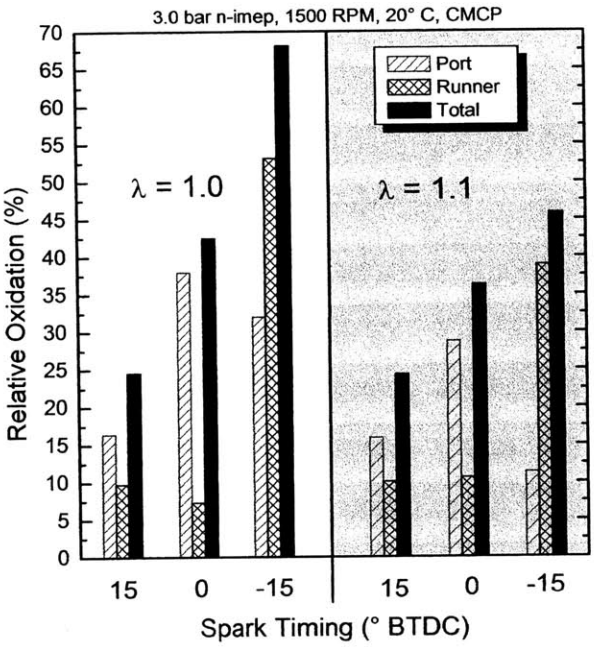

Figure 6.1 Relative port, runner, and total exhaust system HC oxidation as a function of spark timing and relative air/fuel ratio. Data shown for 3.0 bar Net-IMEP, 1500 RPM, 20° C fluids, with intake charge motion (CMCP).

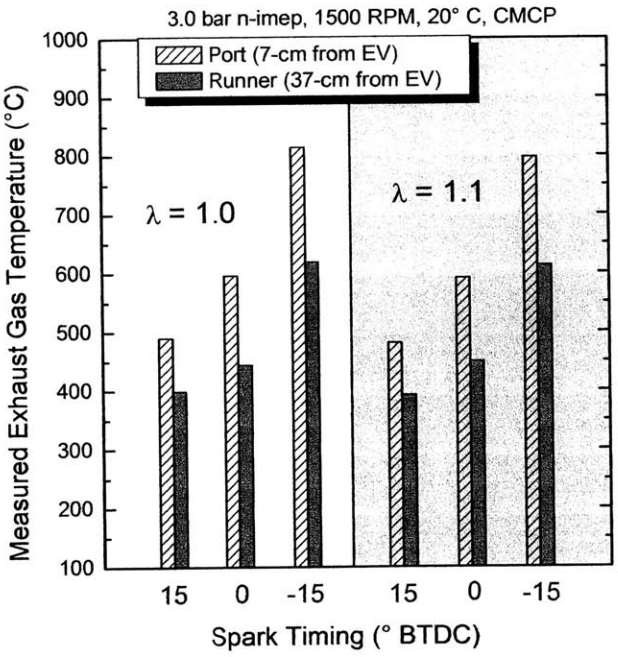

Figure 6.2 Measured port and runner exhaust gas temperature as a function of spark timing and relative air/fuel ratio. Data shown for 3.0 bar Net-IMEP, 1500 RPM, 20° C fluids, with intake charge motion (CMCP).

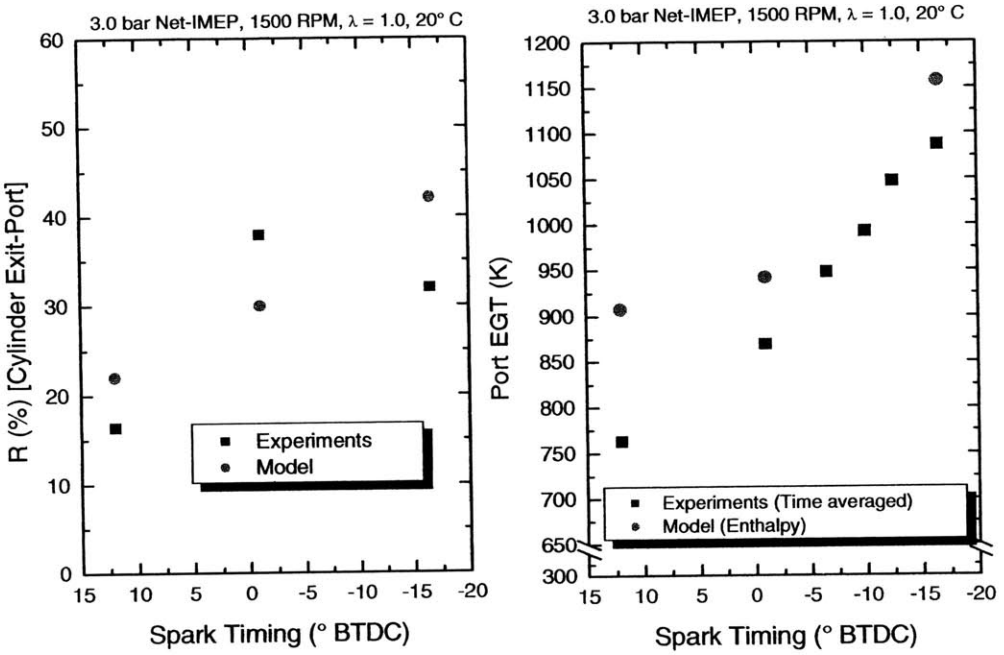

Figure 6.3 Measured and predicted fraction of port reacted hydrocarbons (left) and exhaust port time averaged and enthalpic gas temperatures (right) as a function of spark timing. Data shown for $\lambda = 1.0$, 3.0 bar Net-IMEP, and 1500 RPM.

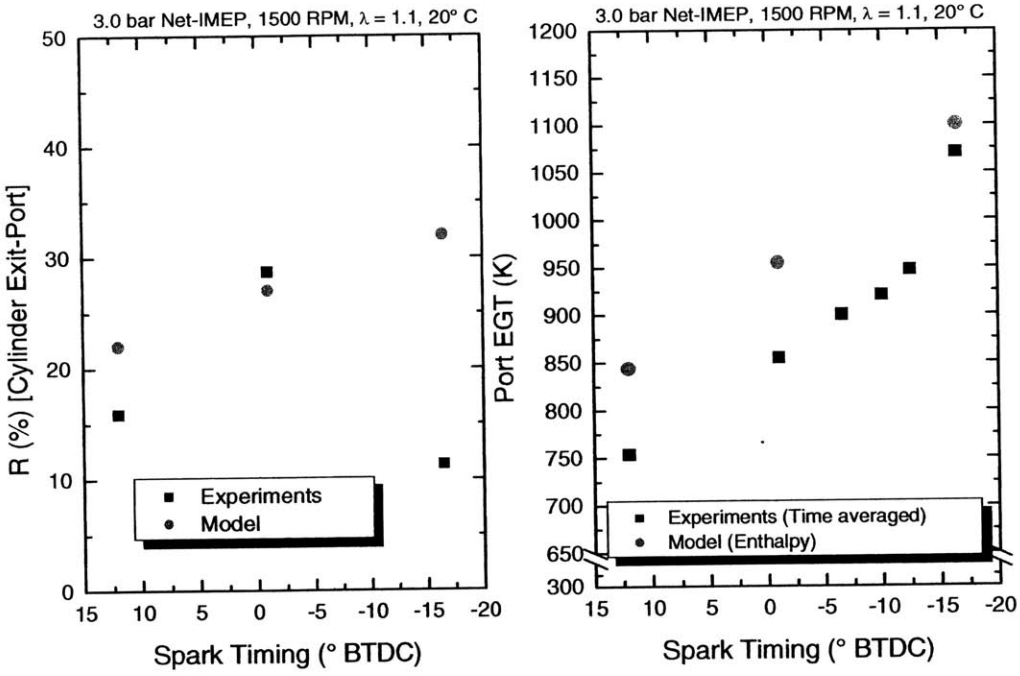

Figure 6.4 Measured and predicted fraction of port reacted hydrocarbons (left) and exhaust port time averaged and enthalpic gas temperatures (right) as a function of spark timing. Data shown for $\lambda = 1.1$, 3.0 bar Net-IMEP, and 1500 RPM.

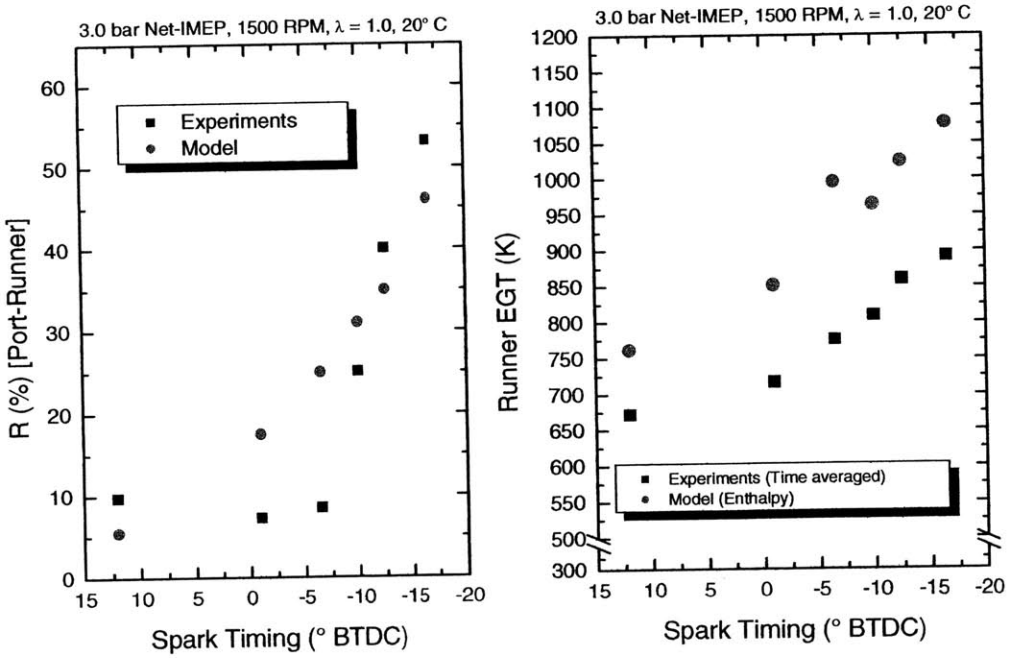

Figure 6.5 Measured and predicted fraction of runner reacted hydrocarbons (left) and exhaust runner time averaged and enthalpic gas temperatures (right) as a function of spark timing. Data shown for $\lambda = 1.0$, 3.0 bar Net-IMEP, and 1500 RPM.

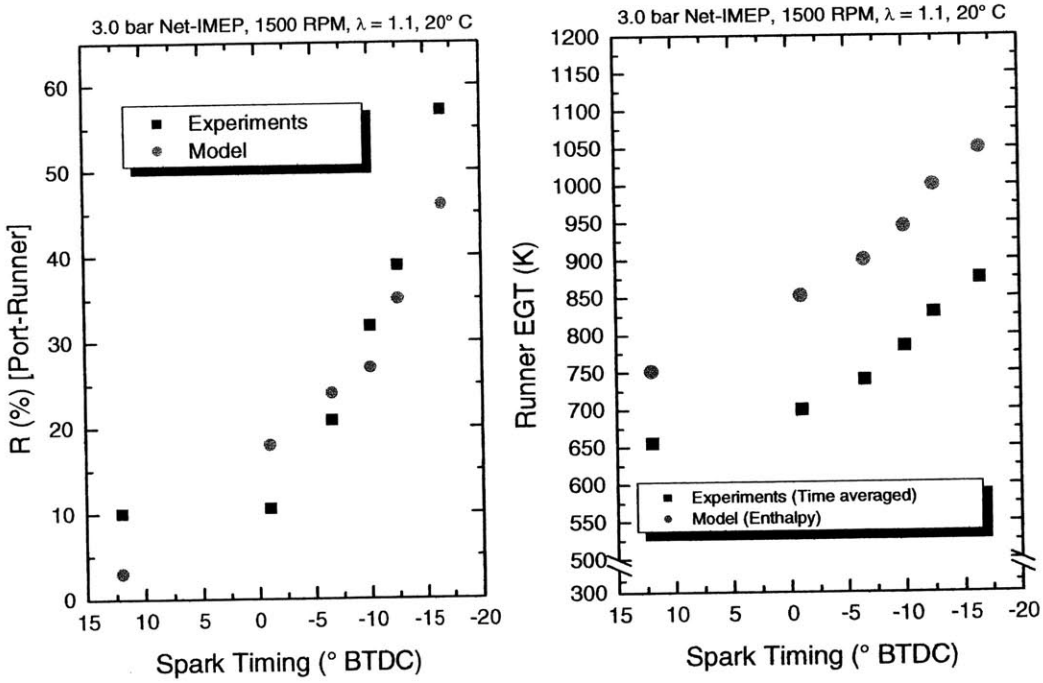

Figure 6.6 Measured and predicted fraction of runner reacted hydrocarbons (left) and exhaust runner time averaged and enthalpic gas temperatures (right) as a function of spark timing. Data shown for $\lambda = 1.1$, 3.0 bar Net-IMEP, and 1500 RPM.

6.2 MODEL SENSITIVITY

6.2.1 GAS TEMPERATURE

Model predictions of the average enthalpic temperatures were investigated to insure the model adequately predicted the heat transfer processes in exhaust port and runner. Cylinder-exit conditions drove the heat transfer sub-routine with correlations based upon empirical data. The model assumes that the wall boundary layer and core gases are well mixed, homogeneous in temperature and composition. A sensitivity analysis was conducted with $\Delta T \pm 100$ K gas element temperatures and the impact on the predicted HC burn up was evaluated, Fig. 6.7.

When temperatures were above 1400 K, hydrocarbon oxidation were consumed in approximately 1 to 2 millisecond. Kinetic time scales were observed to be much faster than the exhaust system residence times, that were on the order of tens of milliseconds. At the most advanced ignition time (Sp = 15° BTDC) a 100 K increase in gas temperature promoted an addition 25% burn up compared to the baseline condition. Likewise, a reduction of temperature below 1100 K, resulted in longer carbon conversion times of HC to CO. These times were observed to be longer than the exhaust port residence time of 2 ms and resulted in a 15% reduction in HC oxidation. With aggressive spark retarded (Sp = -15° BTDC), temperature in excess of 1400 K showed modest burn up sensitivity (less than 10%) to temperature variations.

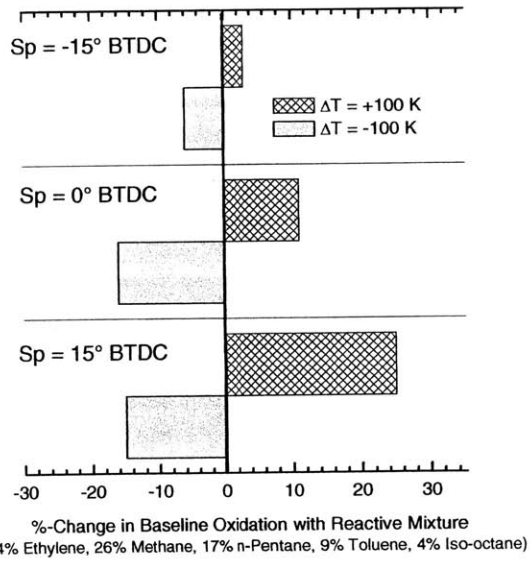

Figure 6.7 Effect of gas temperature on exhaust HC oxidation predictions. Data shown with respect to baseline gas temperatures.

6.2.2 EXHAUST SYSTEM TEMPERATURE

All experiments were conducted with 20° C fluids and hot stabilized exhaust temperatures. Depending upon air/fuel ratio and ignition timing, the hot exhaust component temperatures ranged from 300 - 500° C. An analysis was performed to investigate cold (20° C) wall temperatures and the impact on the predicted HC burn-up, Fig. 6.8. Cold exhaust component temperatures increased heat transfer rates 18 - 23%, and were found to have the most significant (20%) impact on HC burn up for TDC spark timings. Exhaust residence times remained constant, but reduced temperatures increased the chemical kinetic time scales for the reactions.

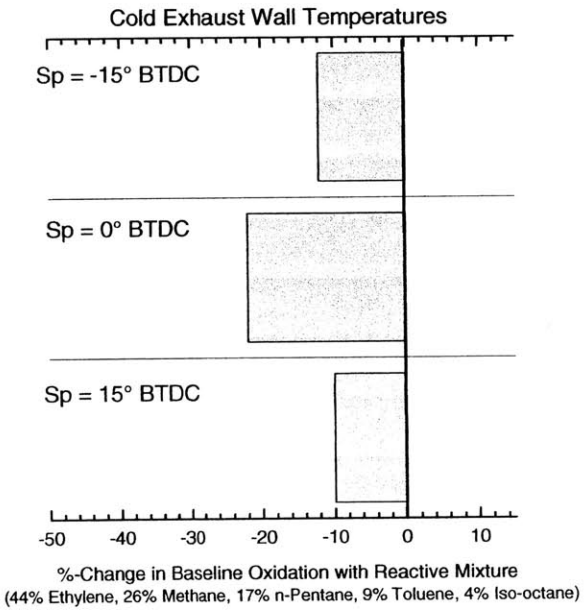

Figure 6.8 Effect of cold (20° C) exhaust component temperature on predicted HC oxidation. Data shown for different ignition timings (Sp) with respect to baseline HC mixture and hot stabilized component temperatures.

6.2.3 MASS ELEMENTS

The mass expelled during the exhaust period was discretized into 5 and 10 independent mass elements distributed as a function of time and compared to the baseline case of 2 elements, Fig 6.9. An increase in the number of mass elements was observed to have no significant impact (less than 4%) on the model's prediction of exhaust oxidation. However, the increase in the number mass elements was found to dramatically increase the required computational time.

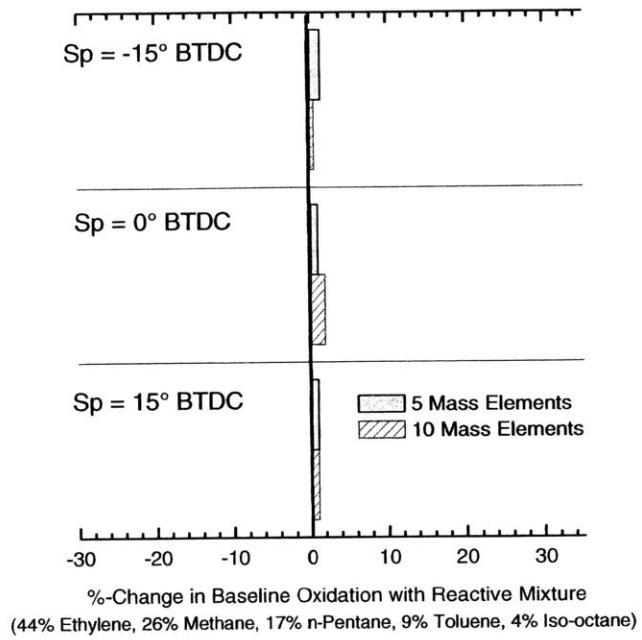

Figure 6.9 Effect of the number exhaust mass elements on predicted exhaust HC oxidation. Data shown with respect to 2 mass element baseline condition.

6.2.4 MIXTURE OF HYDROCARBONS

Three different mixtures of hydrocarbon species representing exhaust emissions were investigated; the baseline mole fraction mixture (case 1) of 44% ethylene, 26% methane, 17% pentane, 9% toluene, and 4% iso-octane. Case 2 contained 100% iso-octane and case 3 was a mixture of 55% ethylene, 35% pentane, and 10% methane, Fig. 6.10. The time for the 50% conversion of hydrocarbons to either CO or CO_2 was calculated for each of the three cases, Fig. 6.11.

The fastest rate of fuel to carbon conversion was observed for the mixture containing the highest concentration of ethylene and n-pentane, case 3. The paraffin (n-pentane) was found to be less stable than the olefins (ethylene), resulting in shorter ignition delay period. Case 3 also had a reduced mole fraction of methane, 10% compared to the baseline case of 26%. High concentrations of methane have been observed to retard autoignition [30]. Case 2, neat iso-octane, a branched paraffin, had the longest fuel destruction time and was attributed to the cracking pattern. Iso-octane breaks up into iso-butene and other species that form relatively stable radicals,

whereas, n-alkanes fragment into ethylene which reacts very rapidly to form highly reactive radicals such as HCO and HCHO.

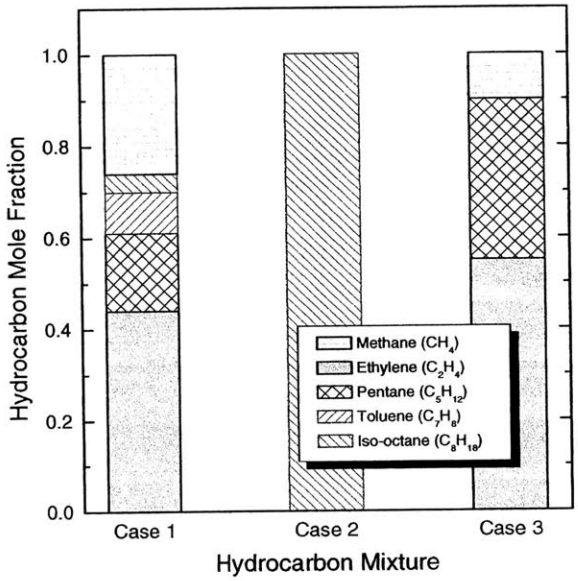

Figure 6.10 Hydrocarbon mole fraction composition for three cases. Data shown for case 1 with the baseline HC mixture, case 2 is 100% iso-octane, and case 3 contains 55% ethylene, 35% pentane, and 10% methane.

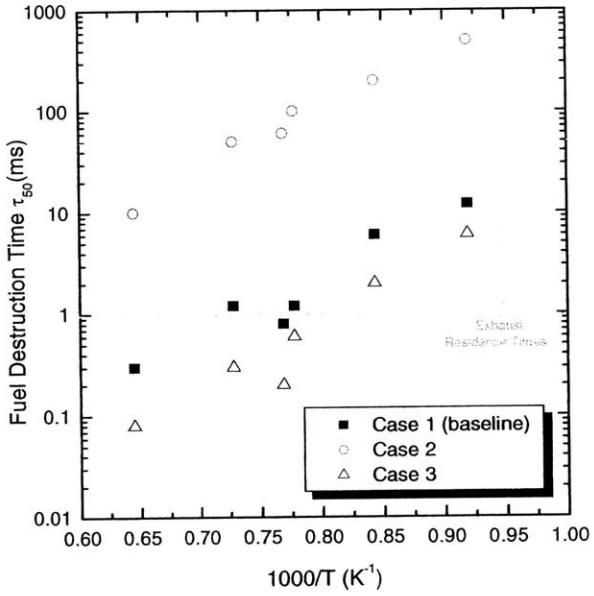

Figure 6.11 Calculated half-lives (τ_{50}) of various hydrocarbon mixtures as a function of temperature for exhaust residence times. Data shown for λ = 1.0, 1% HC gas mixture.

The initial HC species selected for the modeling investigation was shown to have a significant impact on the predicted HC burn up Fig. 6.12. The iso-octane mechanism was found to impede HC burn-up significantly (60 - 90%) compared to the baseline HC reactive mixture, worsening as exhaust port residence decreased with additional spark retard. The reactive mixture of ethylene, n-pentane, and methane was observed to increase the total carbon conversion to CO or CO_2 by 15 - 35%.

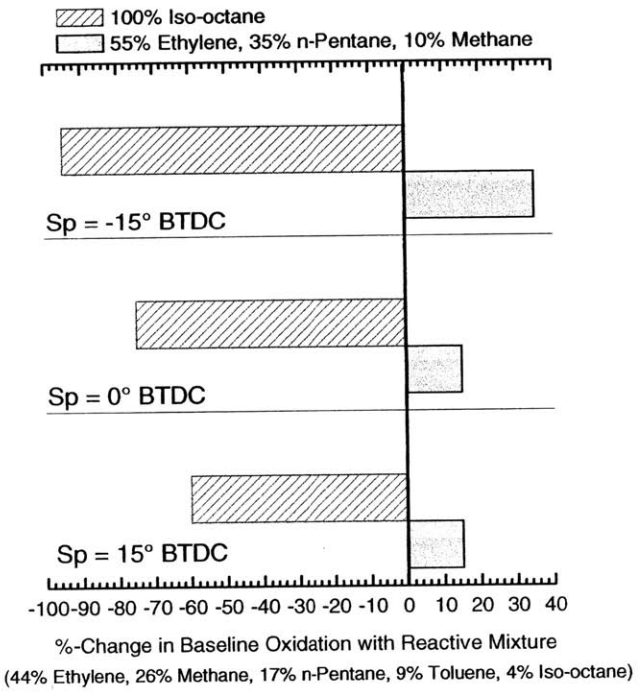

Figure 6.12 Effect of HC mixture on predicted exhaust HC oxidation. Data shown with respect to baseline mixture: 44% ethylene, 26% methane, 17% n-pentane, 9% toluene, and 4% iso-octane.

6.3 Carbon Monoxide Oxidation

6.3.1 Secondary Air Injection

The oxidation of CO into CO_2 occurs relatively late in the chemical reaction scheme after all fuel and HC intermediates are consumed. There are several mechanisms responsible for the oxidation of CO to CO_2, Fig. 6.13. The major pathway (CO + OH <=> CO_2 + H) for oxidation occurs once all HC are consumed and the concentration of hydroxyl (OH) radicals increase and converts CO into CO_2. The characteristic times for CO oxidation computed for various exhaust

relative air/fuel ratios and temperatures (spark timings) are shown in Fig. 6.14. With aggressive TDC and after ignition timings, the characteristic times for CO to CO_2 conversion were found to be less than the exhaust residence times. The CO oxidation model was also used to predict runner exhaust gas temperatures for secondary air injection (SAI) experiments, Fig. 6.15. The calculated adiabatic enthalpic temperatures were within range of measured time-averaged temperatures.

$$O + CO(+M) \leftrightarrow CO_2(+M)$$
$$O_2 + CO \leftrightarrow O + CO_2$$
$$CO + OH \leftrightarrow CO_2 + H$$
$$HO_2 + CO \leftrightarrow OH + CO_2$$

Figure 6.13 CO oxidation reaction mechanisms.

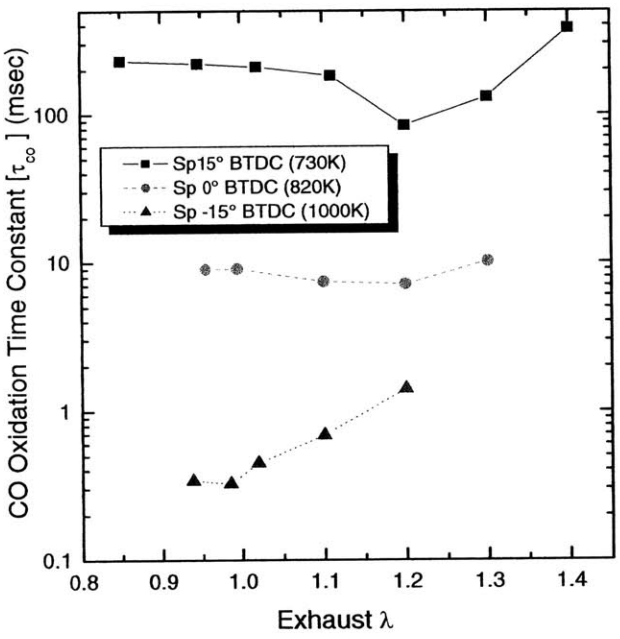

Figure 6.14 CO oxidation time constant as a function of exhaust relative air/fuel ratio (λ) Data shown for three different spark timings (exhaust gas temperatures).

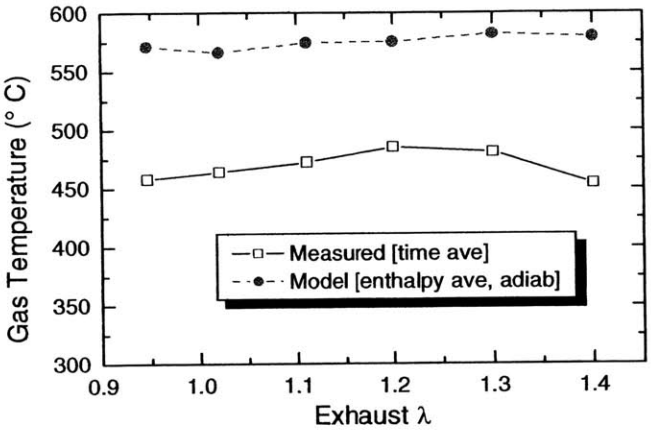

Figure 6.15 Measured time averaged and predicted adiabatic enthalpic runner gas temperatures as a function of exhaust relative air/fuel ratio (λ).

6.4 Extension to Multi-Cylinder Engine

6.4.1 Exhaust Flow and Heat Transfer

The single-cylinder oxidation model was extended to a four-cylinder engine configuration in order to investigate port exit to converter-in HC burn-up. An engine simulation provided exhaust port exit and converter inlet mass flow rates, Figs. 6.16 and 6.17. The ambient exhaust system employed the same single-cylinder heat transfer correlations. However, the exhaust event phasing order (1-3-4-2) resulted in overlap of the displacement and the blowdown process noted in Fig. 6.16. Therefore, the mass elements expelled by adjacent firing cylinders were combined and well-mixed at the runner collector, a distance halfway between the exhaust port and the inlet to the catalytic converter, Fig. 6.18. The single lumped element was taken to have averaged properties and was homogeneous in temperature and composition.

6.4.2 Exhaust Composition

Cylinder-to-cylinder CO, HC, and air/fuel ratio variations were noted in the experimental investigation of cylinder nos. 3 and 4 (Sec. 4.3.3). Exhaust gas CO and HC measurements provided initial composition required for cylinders nos. 3 and 4. The remaining cylinders were assumed to contain an average concentration of the measured emission levels. In order to establish stoichiometric exhaust conditions, each cylinder was assumed to have an equivalent air flow. A

relative air/fuel ratio (λ) of 0.94 was recorded for cylinder no. 3, 1.0 for cylinder no. 4, and 1.03 was assigned to cylinder nos. 1 and 2. Mass elements from different cylinders were lumped, well-mixed, and subjected to a step change in air/fuel ratio at the runner collector before reaching the converter inlet, Fig. 6.19.

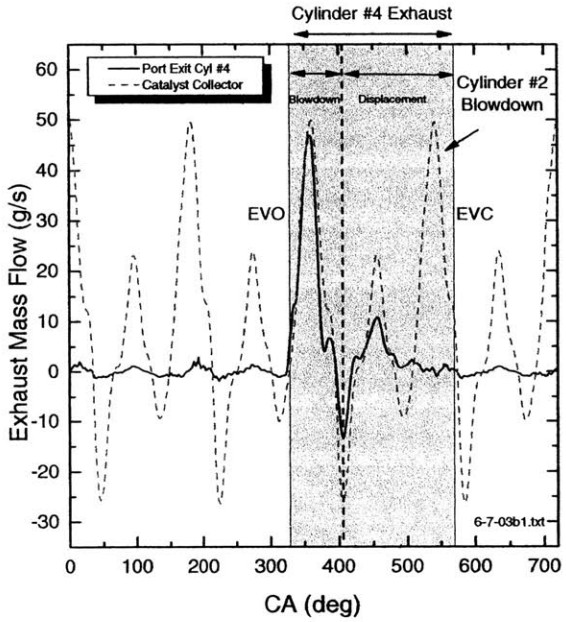

Figure 6.16 Cylinder no. 4 port exit and collector-in exhaust mass flow rate as a function of crank angle.

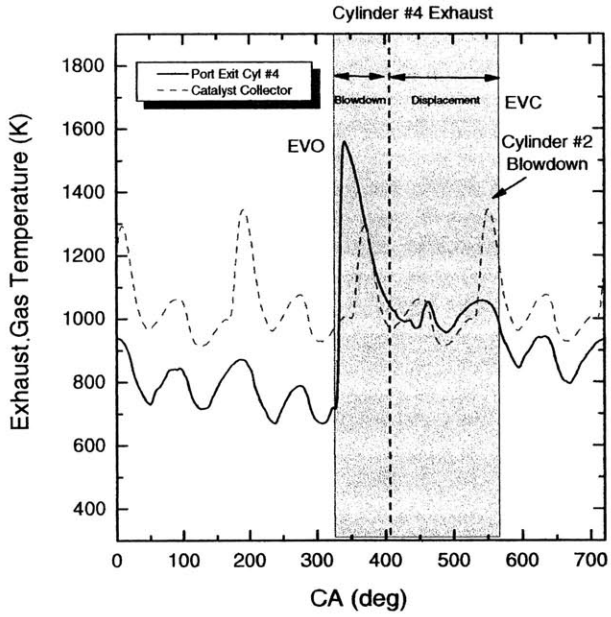

Figure 6.17 Cylinder no. 4 port exit and collector-in exhaust gas temperature as a function of crank angle.

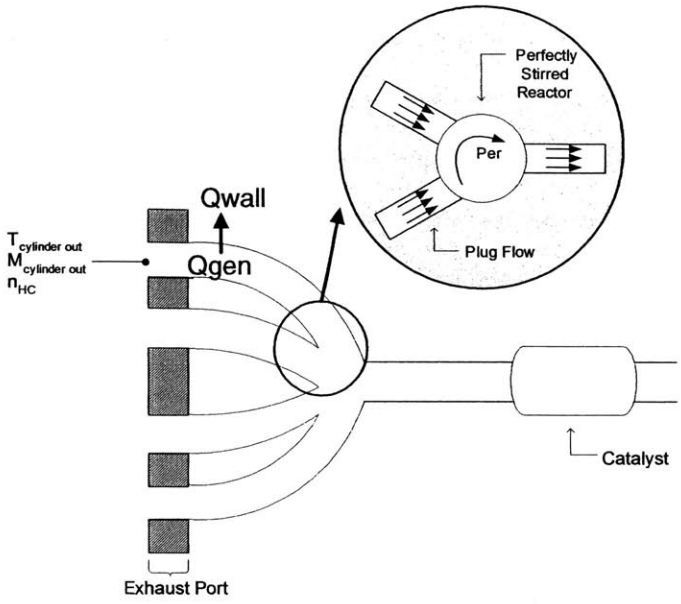

Figure 6.18 Diagram of multi-cylinder exhaust system with runner collector mixing.

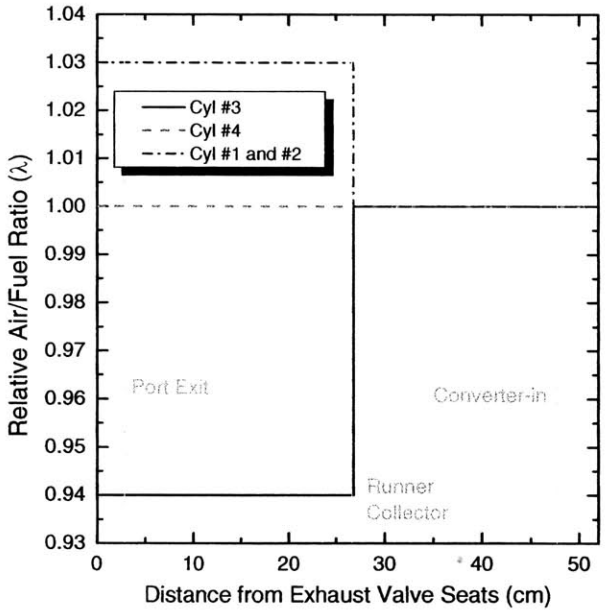

Figure 6.19 Cylinder relative air/fuel ratio as a function of distance from exhaust valve seats.

6.4.3 EXHAUST SYSTEM OXIDATION

The model predicted port exit to converter-in HC oxidation as a function of spark modification for two cases, Fig. 6.20. The first case used a constant relative air/fuel ratio ($\lambda = 1.0$) for all cylinders and an exhaust gas composition based on HC and CO levels measured from cylinder no. 4. Hydrocarbon species were represented by the baseline reactive mixture (ethylene, methane, n-pentane, toluene, iso-octane). Exhaust mass elements were phased according to the multi-cylinder firing order and allowed to combine and mix at the runner inlet before continuing to the converter inlet. The second case accounted for cylinder-to-cylinder exhaust gas compositional variations. Each mass element was had a specified relative air/fuel ratio, Fig. 6.19, that was a function of time (distance) in the plug flow model. The reactive mixture of HC was also used to model the species present in the exhaust gas. Converter-in enthalpic exhaust gas temperatures were computed for both cases and compared to time averaged thermocouple measurements, Fig. 6.20.

Agreement between the experiments and model was improved from 30% to 15%. using the change in air/fuel ratio as a function of time (distance). Additional unburned fuel from cylinder no 3. and excess oxygen from cylinder nos. 1 and 2 increased the exhaust system oxidation and exhaust gas temperatures.

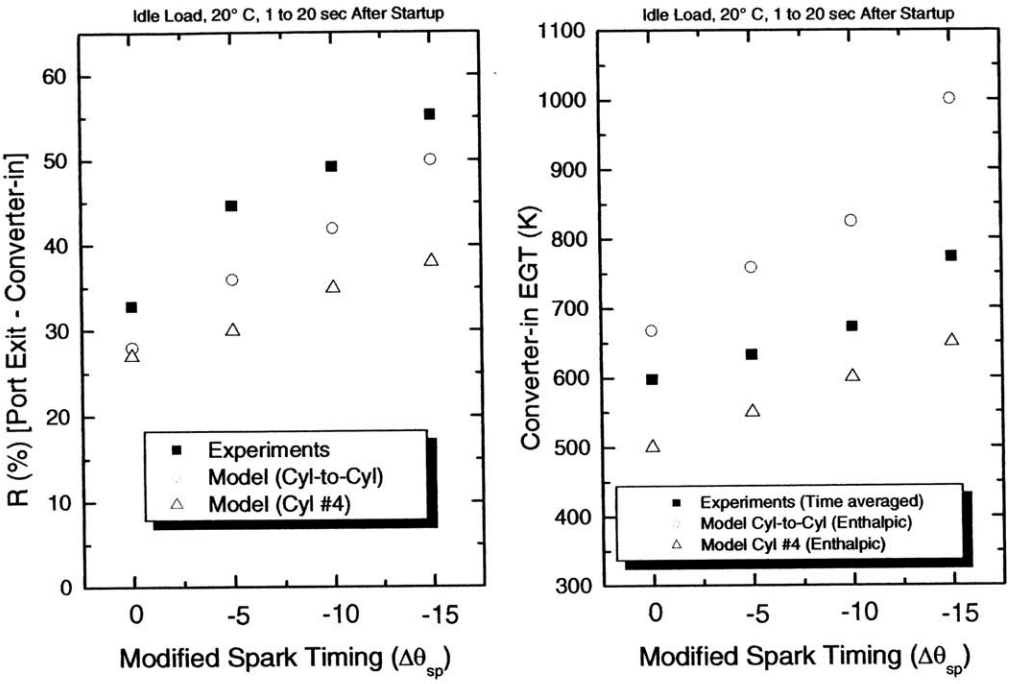

Figure 6.20 Measured and predicted fraction of runner reacted hydrocarbons (left) and exhaust runner time averaged and enthalpic gas temperatures (right) as a function of spark timing. Data shown for idle speed and load conditions, 1 to 20 seconds after 20° C startup. Model initial conditions based upon air/fuel ratio data from cylinder nos. 3 and 4.

CHAPTER 7

SUMMARY AND CONCLUSIONS

7.1 EXPERIMENTS

Experiments were performed to determine the effect of substantial ignition retard on engine combustion, HC emissions, exhaust feed gas enthalpy, and catalyst light-off. A variety of experimental techniques quantified hydrocarbon emissions at several exhaust locations, from cylinder-exit to the catalytic converter inlet, for various spark timings, air/fuel ratios, and fluid temperatures. The results from the investigations were used to develop a phenomenological model of exhaust system oxidation.

7.1.1 SINGLE-CYLINDER ENGINE

Single-cylinder experiments were conducted to provide additional insight into combustion characteristics and HC emission behavior with late spark timings. Detailed mapping of the combustion process and exhaust composition were performed under fixed engine operation and cold (20° C) fluid conditions. The following conclusions were based on the results from those experiments.

1. A single-zone thermodynamic burn rate analysis indicated combustion was complete by exhaust valve opening with spark timings as late as -20° before top dead center (BTDC). Cycle-to-cycle variations increased (up to a maximum COV of 15%) with aggressive spark retard and were attributed to late phasing of the combustion event in a rapidly expanding volume (50% mass fraction burned located 73° after top-dead-center (ATDC)).

2. For an equivalent combustion stability the use of an intake charge motion control plate (CMCP) increased the ignition timing limit increasing feed gas enthalpy rates to the catalyst by more than 60%.

3. A relative air/fuel ratio 10% lean (λ = 1.1) yielded 19% lower tailpipe-out HC emissions than stoichiometric at the same retarded spark timing. Additional molecular oxygen and high burnt gas temperatures increased the rate of post-flame HC oxidation.

4. Exhaust quenching experiments, using CO_2, were conducted to evaluate HC levels exiting the engine at the valve seats. Significant (35%) HC oxidation occurred in the exhaust port with 0° BTDC spark timings.

4. Mass based HC levels calculated from time-resolved HC concentrations and quenching experiments agreed quantitatively with time-averaged HC results. Substantial HC runner burn-up (40 - 50%) and total exhaust system oxidation (47-68%) was observed with -15° BTDC spark timings.

5. Fuel rich engine operation (λ_{engine} = 0.85) with secondary air injection yielded the highest catalyst feed-gas temperature, lowest HC emission, and improved combustion stability compared to stoichiometric and lean operation. At an equivalent exhaust relative air/fuel ratio ($\lambda_{exhaust}$ = 1.2), continuous air injected into the exhaust system was also observed to be more effective in achieving low tailpipe-out HC emissions and high exhaust gas temperatures than phased air injection.

7.1.2 MULTI-CYLINDER ENGINE

Multi-cylinder startup experiments were conducted with cold metal exhaust system temperatures. Combustion stability, feed gas enthalpy, and catalyst light-off was evaluated for multi-cylinder engine following an ambient startup for four different spark timing modifications.

1. Late spark timings were found to reduce cumulative feed gas HC emissions up to 22% and converter-in sensible enthalpy by a factor of 3 for the engine idle period (1 to 20 seconds) following ambient start-up.

2. Engine operation with the most aggressive ignition timing strategy, reduced the time for catalyst light-off ($\eta_{HC=50\%}$) by 5 seconds (17%) and reduced cumulative converter-in HC mass emissions prior to light-off by 44%.

3. Cylinder-to-cylinder air/fuel ratio variations, measured by time-resolved CO and HC concentrations, were observed to increased as combustion was phased later in the cycle.

7.2 Exhaust Oxidation Model

Exhaust system behavior was investigated with a detailed chemical kinetic mechanism coupled with exhaust fluid flow and exhaust heat transfer. Hydrocarbon tracking and exhaust gas quenching experiments provided quantitative information that was used in a reacting plug flow model. Exhaust gas parameters were obtained from an engine cycle simulation and drove the oxidation model.

1. Exhaust oxidation was observed to be strongly coupled with exhaust gas temperature and hydrocarbon fuel species used to represent the unburned fuel in the chemical mechanism. Fuel destruction times for the conversion of fuel bound carbon to CO or CO_2 varied by two orders of magnitude depending upon the highly diluted mixture of hydrocarbons selected.

2. The mass during the blowdown process had the highest observed gas temperatures and was observed to contain 60 - 80% of the total hydrocarbon emissions.

3. Oxidation was observed to transition from the exhaust port to the exhaust runner as ignition timings were phased after top-dead-center. As spark timing was retarded, the increase in engine flow rate reduced the blowdown element residence time in the exhaust port from 2 to 0.5 ms. Exhaust gas temperatures in excess of 1300 K resulted in chemical kinetic time scales of approximately 1 ms and HC oxidation was observed to occur in the runner.

4. Cold exhaust component and wall temperatures, compared to hot stabilized temperatures, were found to increase heat transfer rates by 18 - 25% and reduce total exhaust system oxidation between 10 - 20%.

5. The single-cylinder model was extended to a multi-cylinder exhaust system to investigate port-exit to converter-in HC burn-up. Overlapping port-exit exhaust flows from adjacent firing cylinders required the model to combine mass elements in a well-mixed region located at the runner collector.

6. Agreement between the model and experiments was significantly improved (30% to 15%) by including cylinder-to-cylinder variations in air/fuel ratio, HC, and CO exhaust gas concentrations. A step change in the air/fuel ratio occurred at a distance halfway between the exhaust port and inlet to the catalyst converter. Additional available oxygen was introduced into fuel rich mass elements resulting in exothermic reactions. HC burn-up was constrained to a reduced volume, minimizing heat transfer losses and increasing reaction rates.

REFERENCES

1. Eastwood, P., Critical Topics in Exhaust Gas Aftertreatment, Research Studies Press Ltd., UK 2000.

2. Kollmann K., Abthoff J., and Zahn W., "Secondary Air Injection with a New Developed Electrical Blower for Reduced Exhaust Emissions," SAE Paper 940472, 1994.

3. Caton, J. A. and Heywood, J. B., "Models for heat transfer, mixing and hydrocarbon oxidation in an exhaust port of a spark-ignited engine," SAE Paper 800290, 1980.

4. Russ, S., Lavoie, G., and Dai, W., "SI Engine Operation with Retarded Ignition: Part 1 - Cyclic Variations," SAE Paper 1999-01-3506, 1999.

5. Russ, S., Thiel, M., and Lavoie, G., "SI Engine Operation with Retarded Ignition: Part 2 - HC Emissions and Oxidation," SAE Paper 1999-01-3507, 1999.

6. Goldwitz, J. "Combustion Optimization in a Hydrogen-Enhanced Lean Burn SI Engine," S.M. Thesis, MIT Department of Mechanical Engineering, 2002.

7. UTG-96 Fuel Properties, Chevron Phillips Chemical Company LLC, October 2004 <http://www.cpchem.com/tds_unsecured/UTG96.pdf>.

8. Cambustion NDIR-500, October 2004 <http://www.cambustion.co.uk>.

9. Cheung, H. M. and Heywood, J. B., "Evaluation of a One-Zone Burn-Rate Analysis Procedure Using Production SI Engine Pressure Data," SAE Paper 932749, 1993.

10. Cheng, W.K., Summers, T., and Collings, N., "The Fast-Response Flame Ionization Detector," Progress in Energy and Combustion Science, Volume 24, Issue 2, 1998, Pages 89-124.

11. Herrin, R.J., "The Importance of Secondary Air Mixing in Exhaust Thermal Reactor Systems," SAE Paper 750174, 1975.

12. Borland, M. and Zhao, F., "Application of Secondary Air Injection for Simultaneously Reducing Converter-In Emissions and Improving Catalyst Light-Off Performance," SAE Paper 2002-01-2803, 2002.

13. Koehlen, C., Holder, E., and Vent, G., "Investigation of Post Oxidation and Its Dependency on Engine Combustion and Exhaust Manifold Desing," SAE Paper 2002-01-0744, 2002.

14. Heywood, J. B., Internal Combustion Engine Fundementals, McGraw-Hill, New York, 1998.

15. Alkidas, A., "Indication of Fuel Maldistribution in Spark-Ignition Engines," American Society of Mechanical Engineers Internal Combustion Engine Division, Vol. 24-4, 1995.

16. Yamamoto, S., Matsushita, K., Etoh, S., and Takaya, M., "In-line Hydrocarbon (HC) Absorber System for Reducing Cold-Start Emissions," SAE Paper 2000-01-0892, 2000.

17. Kubo, S., Yamamoto, Kizaki, Y., Yamazaki, S., Tanaka, T., and Nakanishi, K., "Speciated Hydrocarobn Emissions of SI Engine During Cold Start and Warm-up," SAE Paper 932706, 1993.

18. Kaiser E., Siegl, W., Cotton, D., and Anderson, R., "Effect of Fuel Structure on Emissions from a Spark-Ignited Engine," Environ. Sci. Technol., Vol. 25 (1991) pgs. 2005-2012.

19. Kaiser, E., Siegl, W., Trinker, F., Cotton, D., Cheng, W., and Drobot, K., "Effect of Engine Operating Parameters on Hydrocarbon Oxidation in the Exhaust Port and Runner of a Spark-Ignited Engine," SAE Paper 950159, 1995.

20. Takahashi, H., Ishizuka, Y., Tomita, M., and Nishizawa, K., "Engine-Out and Tail-Pipe Emission Reduction Technologies of V-6 LEVs," SAE Paper 980674, 1998.

21. Landsberg, G., Heywood, J., and Cheng, W., "Contribution of Liquid Fuel to Hydrocarbon Emissions in Spark-Ignition Engines," SAE Paper 2001-01-3587, 2001.

22. Nakayama, Y., Maruya, T., Oikawa, T. Kawamata, M., Fujiwara, M., "Reduction on HC Emission from VTEC Engine During Cold-Start Condition," SAE Paper 940481, 1994.

23. Chemkin Collection Release 3.6, "Senkin: A Program for Predicting Homogenneous Gas-Phas Chemical Kinetics in a Closed System with Sensitivity Analysis", October 2004 <http://www.chemkin.com>.

24. Curran, H. J., Gaffuri, P., Pitz, W. J., and Westbrook, C. K. "A Comprehensive Modeling Study of iso-Octane Oxidation," Combustion and Flame 129:253-280 (2002).

25. Pitz, W., Seiser, R., Bozzelii, J., Seshadri, K., Chen, C., Da Costa, I., Fournet, R., Billaud, F., Battin-Lecler, F., and Westbrook, C., "Chemical Kinetic Study of Toluene Oxidation Under Premixed and Nonpremiexed Conditiions," Manuscript Draft.

26. Caton, J., "Heat Transfer, Mixing and Hydrocarbon Oxidation in an Engine Exhaust Port," Ph.D. Thesis, MIT Department of Mechanical Engineering, 1979.

27. Chan,S. and Hoang, D., "Modeling of Catalytic Conversion of CO/HC in Gasoline Exhaust at Engine Cold-Start," SAE Paper 1999-01-0452, 1999.

28. Fox, J., Cheng, W., and Heywood, J., "A Model for Predicting Residucal Gas Fraction in Spark-Ignition Engines," SAE Paper 931025, 1993.

29. Wu, K., "Chemical Kinetic Modeling of Oxidation of Hydrocarbon Emissions in Spark Ignition Engines," S.M. Thesis, MIT Department of Mechanical Engineering, 1994.

30. Glassman, I., Combustion, 3rd edition, Academic Press, San Diego, 1996.

31. Caton, J., "Comparisons of Thermocouple,Time-averaged and Mass-Averaged Exhaust Gas Temperatures for a Spark-Ignited Engine," SAE Paper 820050, 1982.

APPENDIX A

BURN RATE ANALYSIS PROGRAM

A.1 ENERGY EQUATION

Energy Equation (A.1.1)

$$\frac{\partial Q_{Chemical}}{\partial \theta} = \frac{\gamma - 1}{\gamma} p \frac{\partial V}{\partial \theta} + \frac{1}{\gamma - 1} V \frac{\partial p}{\partial \theta} + \frac{\partial Q_{Crevice}}{\partial \theta} + \frac{\partial Q_{HT}}{\partial \theta}$$

where:

$Q_{Chemical}$	*fuel chemical energy*
θ	*crank angle*
γ	*ratio of specific heat*
p	*cylinder pressure*
V	*cylinder volume*
$Q_{Crevice}$	*energy in crevices*
Q_{HT}	*heat transfer*

A.2 RESIDUAL GAS ESTIMATION

Fox Correlation (modified for a 4-valve engine) [28] (A.2.1)

$$X_{residual} = 1.266 * \frac{O.F.}{N} * \left(\frac{P_{in}}{P_{exh}}\right)^{-0.87} * \sqrt{\left|P_{exh} - P_{in}\right|} + 0.632 * \frac{\Phi}{r_c}\left(\frac{P_{in}}{P_{exh}}\right)^{-0.74}$$

$$O.F. = \frac{1.45}{B} * (107 + 7.8 * \Delta\Theta + \Delta\Theta^2) * \left(\frac{L_{v,\max} * D_v}{B}\right)$$

$\Delta\Theta$ = Deg. of Valve Overlap

A.3 IN-CYLINDER HEAT TRANSFER

Woschni Correlation (A.3.1)

$$\frac{dQ_{ht}}{dt} = A * h_c * (T - T_{wall})$$

A = Heat Transfer Area

h_c = Convective Heat Transfer Coefficient

$$h_c = 3.56 * C_1 * B^{-2} P^{.8} T^{-0.546} w^{.8}$$

$$w = 2.28(\bar{s}_p + u_{swirl}) + 3.25 * 10^{-3} * c_2 * T_{IVC} * \left(\frac{V_d}{V_{IVC}}\right) * \left(\frac{P_{firing} - P_{motoring}}{P_{IVC}}\right)$$

A.4 EXHAUST GAS PROPERTIES

Exhaust gas properties as a function of temperature [3] (A.4.1)

$$x(T) = \alpha + \beta T + \eta T^2$$

where:

T is degrees Kelvin (K)

Table A.4.1: Viscosity (μ), thermoconductiveity (k), and ratio of specific heat capacities (γ) coefficients (pressure of 1 bar and temperatures 600 - 2000K) used for Eq. A.4.1.

x	α	β	η
μ_{exh} (g/cm*s)	7.280E-05	3.553E-07	-4.399E-11
k_{exh} (J/m*s*K)	2.326E-03	7.577E-05	-6.797E-09
γ_{exh}	1.424E+00	-1.833E-04	5.024E-08

APPENDIX B

MDS SYSTEM INSTRUCTIONS

B.1 MDS FILE BOOT AND DOWNLOAD

1. Run the Delco Electronics ITS software, when prompted, keep the system "off-line". Select "File" then "Unpack and Open" from the main menu, open the baseline default "ColdriveR3182088.PnG" file.

2. Select "Open" and the required engine software, boot file, and MDS file will be copied onto the hard drive in a new directory called "C:\s19files\r_03_182" manually copy the baseline engine calibration file "a3m182d1.s19" to the "C:\s19files\r_03_182" directory. Now select: "File", "Open" and select the "ColdriveR3182088.prj" project file which will be located in the "C:\s19files\r_03_182\mds" directory. Select "OK"

3. Make sure that ignition power is off to the ECM harness and disconnect power to the MDS system. Verify that the MDS XPOD is connected to the ECM and reconnect power to the MDS and hit the reset button on the MDS display unit. The MDS system must be powered for the next step.

4. Select: "Launch", "Instrument Controller Tool" and select the "Boot" button and select "Open". This will start the Boot procedure for the MDS system. The Boot procedure will load the MDS system with the required configuration files, engine software, and boot files. Note, when the boot procedure completes the display unit (DU) should contain variable names and when the ignition power is applied to the ECM the values for the variable should be displayed.

5. The engine calibration file will have to be downloaded next by selecting the "Download" button on the "Instrument Controller Tool". Select the "a3m182d1.s19" calibration file and make sure that "Dave A File" is selected for the Destination and "Port A" is selected for the Device. Select "OK" when the file is selected and the file will be downloaded. Now, one can start the engine and view and slew the variables on the MDS display unit update.

B.2 AIR/FUEL RATIO CALIBRATION MODIFICATION

1. Using "Caltools", open the calibration file named "A3M182D1.S19" along with the database file "C3182088.dbf". Linear interpolation between points is done, never edit the length of the hex file, MS Excel can be used to modify the table. Any modifications and changes to the calibration file should be saved under a different file name and should be fully document by the user. The file then should be download via the ITS shell as outlined earlier in Appendix B.1.

2. The air/fuel ratio during a start is called with the F54C, F51D and F65A tables, Fig. B.2.1. Table F54C determines the beginning cranking A/F ratio as a function of start-up coolant temperature. Tables F51D and F65A are the slow and fast "chokes" subtracted from the desired running A/F ratio (KAFSTCN). They are also looked up as a function of start-up coolant and decrement from there as a function of time. The fast "choke" decrements 0.1 of an A/F ratio every 200 ms and the slow "choke" decrements 0.1 of an A/F ratio every 1.4 seconds. The A/F ratio is controlled by start-up coolant temp and time, there is no firing event-to-event control.

3. Closed loop A/F control is achieved after 20 seconds of engine operation and is controlled by the F124C table which commands an A/F = 14.4 in

order to burn an A/F = 14.6. Feed back control can be accelerated by externally heating the exhaust gas oxygen (EGO) sensor. However, the threshold voltage output for rich (600 mV) and lean (300 mV) excursions much be changed by editing the KO2AMAXA table and the EGO timer table KO2ATIME. Tables KT1A and KT2A must also be changed in order to achieve a maximum feedback of approximately 5 seconds, Fig. B.2.1.

4. The engine using a "6x" encoder system and is synchronized off a TDC marker (cylinders no. 1 and no. 4) and all injectors fire upon engine cranking. Paired cylinders are sparked (nos. 1 & 4 and nos. 2 & 3) the cycle position is determined from spark discharge times differences between the two fired cylinders.

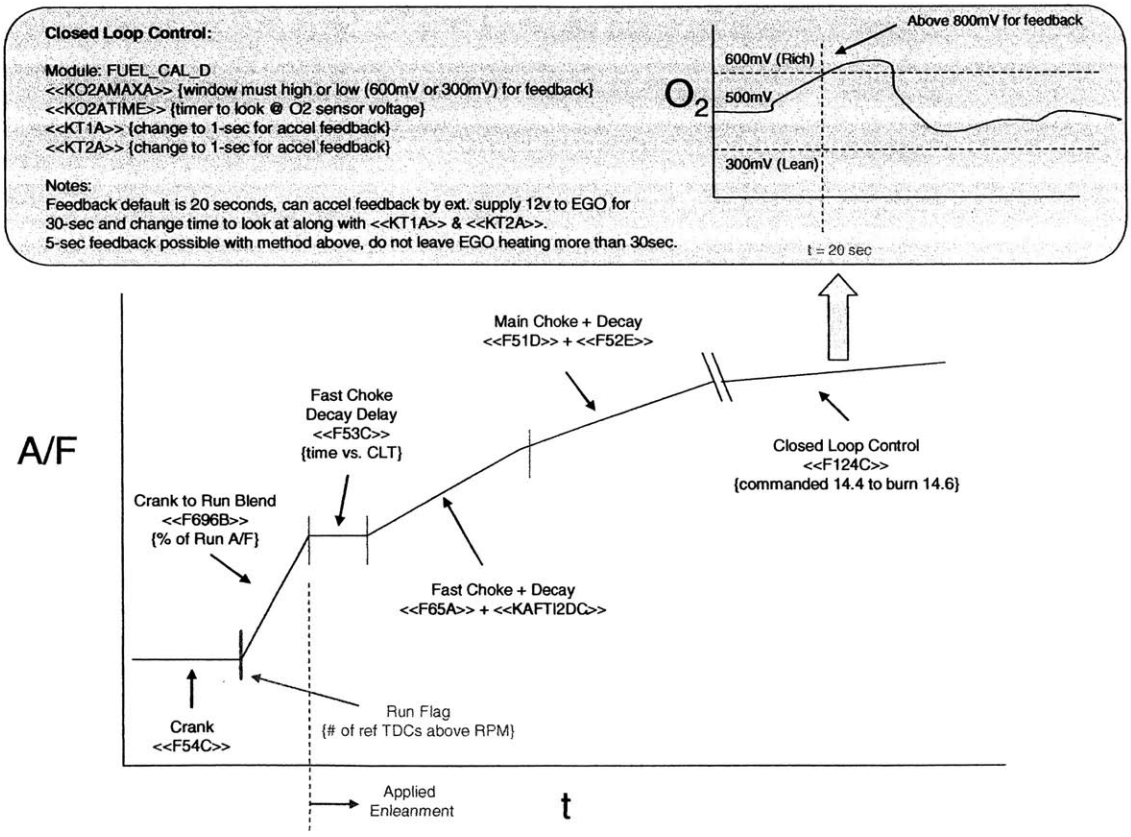

Figure B.2.1 Air/fuel ratio as a function time with noted calibration tables controlling A/F ratio. Closed loop operation with the exhaust gas oxygen sensor (O_2) noted in top of figure.

B.3 SPARK, RPM, AND IAC CALIBRATION MODIFICATIONS

1. Spark timing control works same way, a base value will come from F1 (latercalledKtSPRK_phi_F1SparkAdvance) and F1EXTA tables. It is a function of engine speed and load. During a start some catalytic converter light off retard will be applied and it is not a function of cylinder events, Fig B.3.1.

2. Cranking spark is fixed by the "calsKwSPRK_phi_FTSMAdvance", KwSPRK_n_FTSMLowerLimit, KwSPRK_n_FTSMUpperLimit, KRPMUPS, and KRPMDNS. These five calibration variables are a spark value, a lower window hysteresis pair and an upper window hysteresis is pair. The window refers to where FTSM (fixed targeted spark mode) will operate as opposed to runs spark mode. The hardware will not be able to provide firing event-to-event control.

3. Idle RPM is controlled by table F13 and is a function of coolant temperature

4. Idle air control (IAC) uses the INPTCALD module and is controlled by two tables. Table F17A controls the IAC stepper position as a function of coolant temperature during engine cranking and table F10B governs the position based upon the offset to learned position. Module IDLECALD sets the stepper stop position (maximum position is 255 counts). Note that the engine much reach warmed-up (90° C) to learn a position.

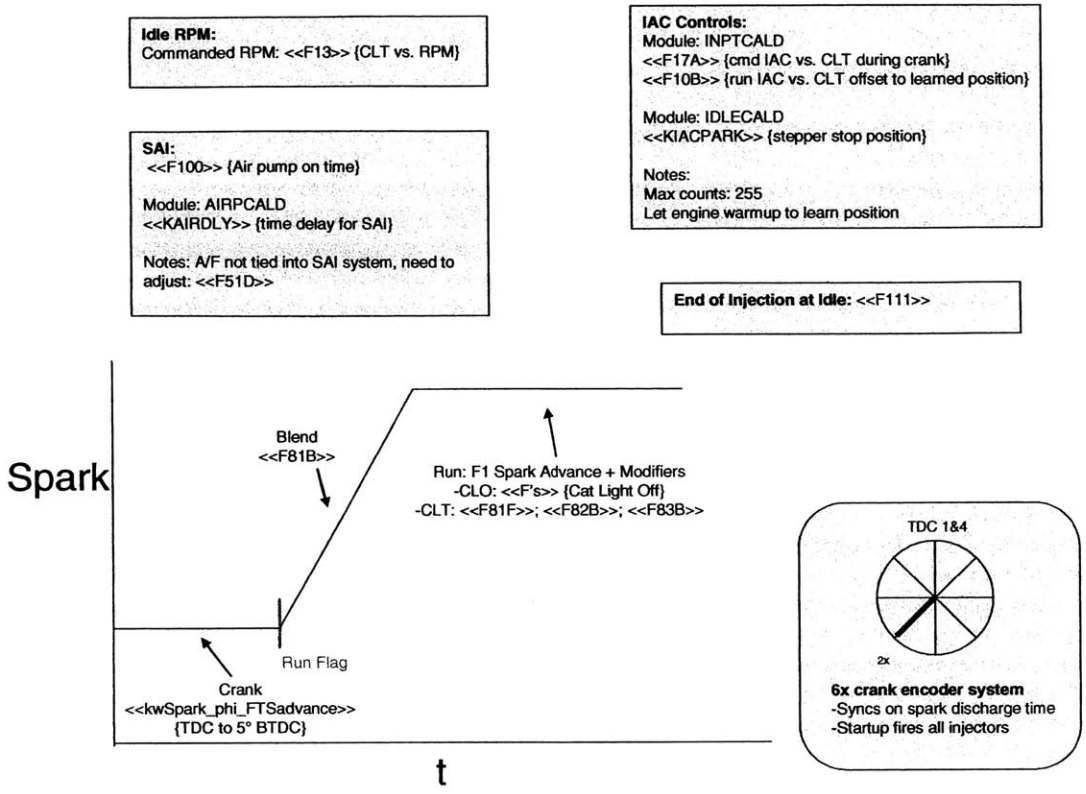

Figure B.3.1 Spark timing as a function of time after crank. Tables noted

APPENDIX C

SINGLE-CYLINDER DATA

C.1 DATA TABLES

C.1.1 Steady-State, 20° C Fluids, 3.0 bar Net-IMEP, 1500 RPM, with intake CMCP

Lambda (λ)	Spark (°BTDC)	MAP (bar)	Mair (g/sec)	Mfuel (g/sec)	Runner wall skin (°C)	Runner EGT (°C)	Port EGT (°C)	Tailpipe-out HC (ppm C1)	ssHC (mg/sec)	eiHC (g/kg)	COV of Net-IMEP (%)	Loc. 50% MFB (°ATDC)	0-10% Dur (deg)	10-90% Dur (deg)
1.0	12	0.465	2.86	0.196	250	399	490	3816	5.64	28.8	1.1	16	19	17
1.0	-1	0.558	3.33	0.228	267	444	596	2700	4.65	20.4	4.9	37	24	24
1.0	-7	0.660	3.87	0.265	305	503	675	2031	4.06	15.3	7.0	49	29	28
1.0	-10	0.751	4.34	0.298	325	537	719	1830	4.10	13.8	8.0	56	31	29
1.0	-13	0.849	4.79	0.328	390	587	774	1710	4.23	12.9	9.4	63	33	31
1.0	-17	0.950	5.45	0.373	415	619	814	1632	4.59	12.3	12.0	73	38	33
1.1	16	0.467	3.00	0.187	258	393	481	3621	5.57	29.9	1.1	12	20	17
1.1	3	0.555	3.41	0.212	302	449	591	2496	4.37	20.6	5.7	34	25	25
1.1	-3	0.656	3.87	0.241	335	496	656	1812	3.60	14.9	9.3	46	29	30
1.1	-6	0.748	4.34	0.270	354	529	696	1536	3.42	12.7	9.4	53	31	32
1.1	-9	0.846	4.86	0.302	387	568	747	1329	3.31	11.0	12.0	61	34	35
1.1	-12	0.950	5.53	0.344	412	608	794	1224	3.47	10.1	13.0	69	38	37
1.2	9	0.552	3.44	0.196	284	423	544	3066	5.38	27.4	4.9	27	24	25
1.2	2	0.655	4.00	0.228	317	473	619	2430	4.97	21.7	9.8	42	28	32
1.2	-1	0.744	4.40	0.251	344	499	656	2055	4.61	18.4	13.0	50	32	37
1.2	-4	0.847	4.96	0.283	370	538	715	1611	4.08	14.4	15.0	58	35	40

C.1.2 Steady-State, 90° C Fluids, 3.0 bar Net-IMEP, 1500 RPM, with intake CMCP

Lambda (λ)	Spark (°BTDC)	MAP (bar)	Mair (g/sec)	Mfuel (g/sec)	Runner wall skin (°C)	Runner EGT (°C)	Port EGT (°C)	Tailpipe-out HC (ppm C1)	ssHC (mg/sec)	eiHC (g/kg)	COV of Net-IMEP (%)	Loc. 50% MFB (°ATDC)	0-10% Dur (deg)	10-90% Dur (deg)
1.0	10	0.463	2.63	0.180	282	533	605	2226	3.02	16.8	1.4	18	19	18
1.0	-3	0.557	3.05	0.209	326	636	700	996	1.57	7.5	4.1	39	24	25
1.0	-8	0.661	3.55	0.243	355	687	752	576	1.06	4.3	5.5	50	36	27
1.0	-13	0.755	3.99	0.273	381	739	794	423	0.87	3.2	7.3	59	44	29
1.0	-16	0.855	4.46	0.306	393	788	826	303	0.70	2.3	7.9	66	50	30
1.0	-20	0.944	5.07	0.347	382	820	860	286.5	0.75	2.2	9.2	74	58	31
1.1	19	0.462	2.69	0.167	267	487	569	2442	3.37	20.1	1.0	9	19	17
1.1	2	0.557	3.10	0.193	319	608	662	1002	1.59	8.3	4.5	34	24	25
1.1	-4	0.660	3.56	0.222	350	669	715	540	0.99	4.5	7.3	47	32	30
1.1	-8	0.755	4.00	0.249	375	716	757	352.5	0.72	2.9	8.6	56	39	33
1.1	-12	0.852	4.49	0.280	382	753	794	288	0.66	2.4	11.0	65	47	34
1.1	-16	0.944	5.11	0.318	391	794	826	219	0.58	1.8	11.0	73	54	35
1.2	8	0.554	3.16	0.180	300	558	610	1545	2.49	13.8	4.0	28	24	25
1.2	1	0.657	3.58	0.204	327	620	666	855	1.56	7.7	7.7	42	28	31
1.2	-3	0.754	4.00	0.228	360	672	710	534	1.09	4.8	10.0	52	34	36
1.2	-7	0.853	4.54	0.259	353	715	748	382.5	0.89	3.4	12.0	61	41	39
1.2	-10	0.944	5.13	0.293	385	753	776	295.5	0.77	2.6	15.0	69	49	40

C.2 EXHAUST TEMPERATURES

C.2.1 With Charge Motion Control Plate (CMCP)

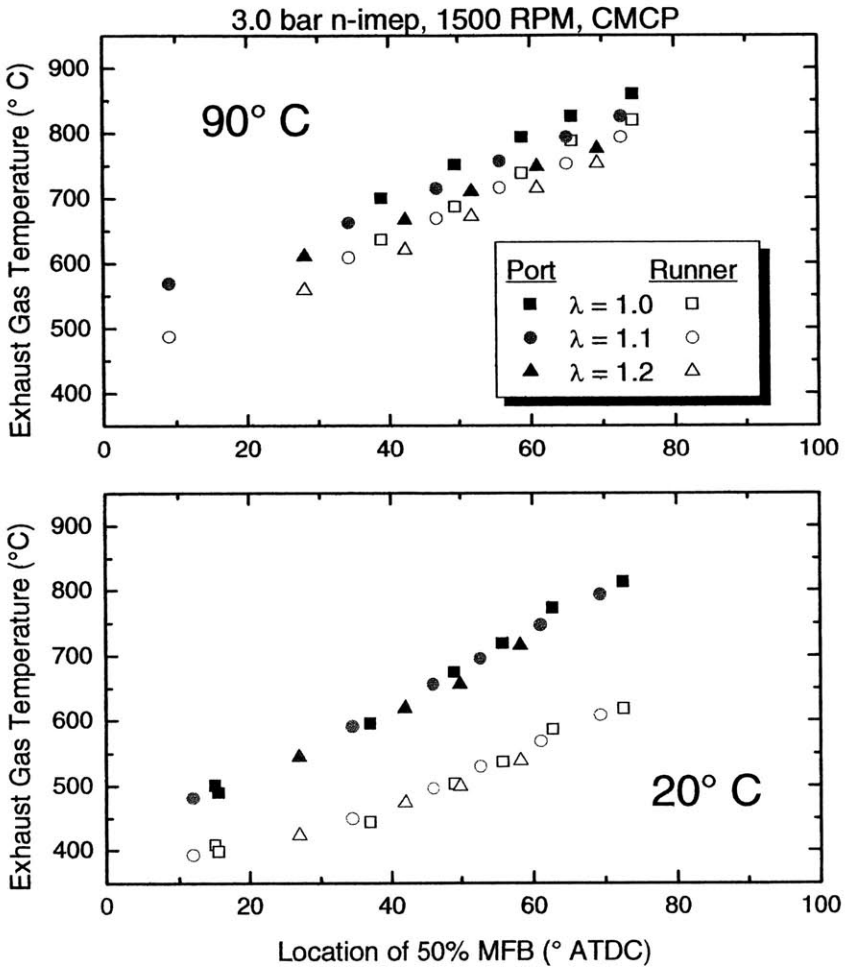

Figure C.2.1 Port exit and runner exhaust gas temperatures as function of the location of the 50% mass fraction burned (MFB) for 20° C and 90° C fluid temperatures and various relative air/fuel ratios. Data shown for 3.0 bar Net-IMEP, 1500 RPM, with intake charge motion control plate (CMCP).

C.2.2 Without Charge Motion Control Plate (CMCP)

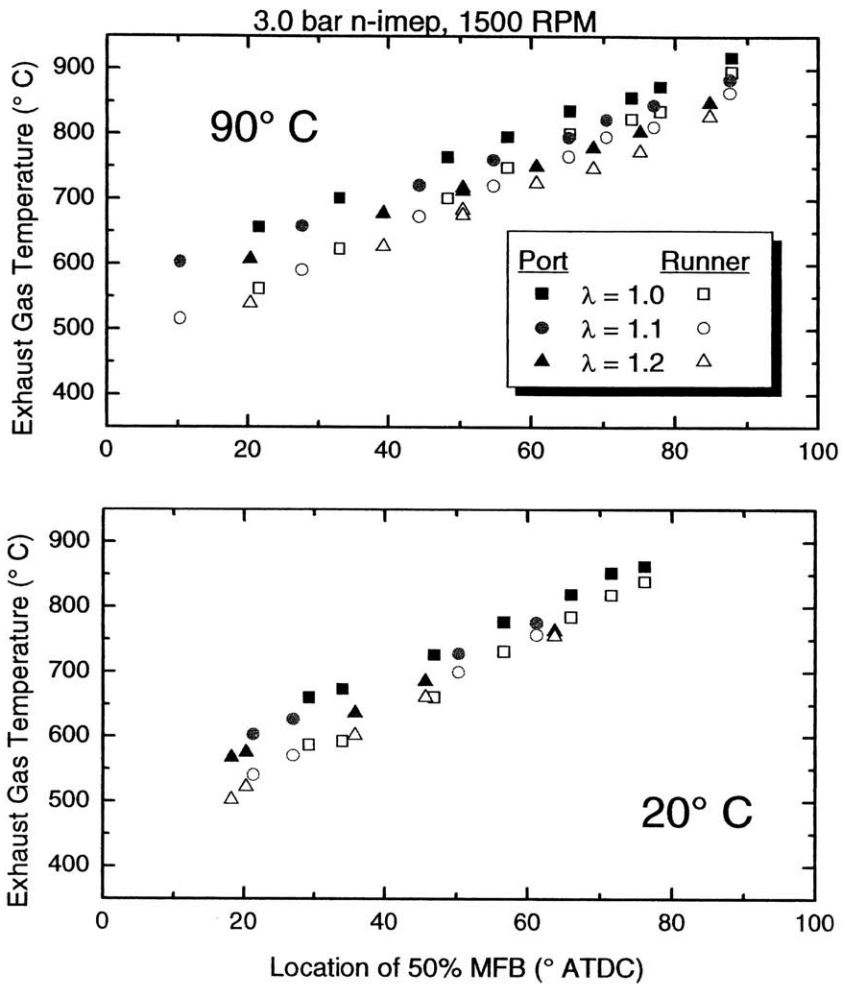

Figure C.2.2 Port exit and runner exhaust gas temperatures as function of the location of the 50% mass fraction burned (MFB) for 20° C and 90° C fluid temperatures and various relative air/fuel ratios. Data shown for 3.0 bar Net-IMEP, 1500 RPM, without intake charge motion control plate (CMCP).

C.3 BURN RATE ANALYSIS: 90°, 40°, AND 20° C

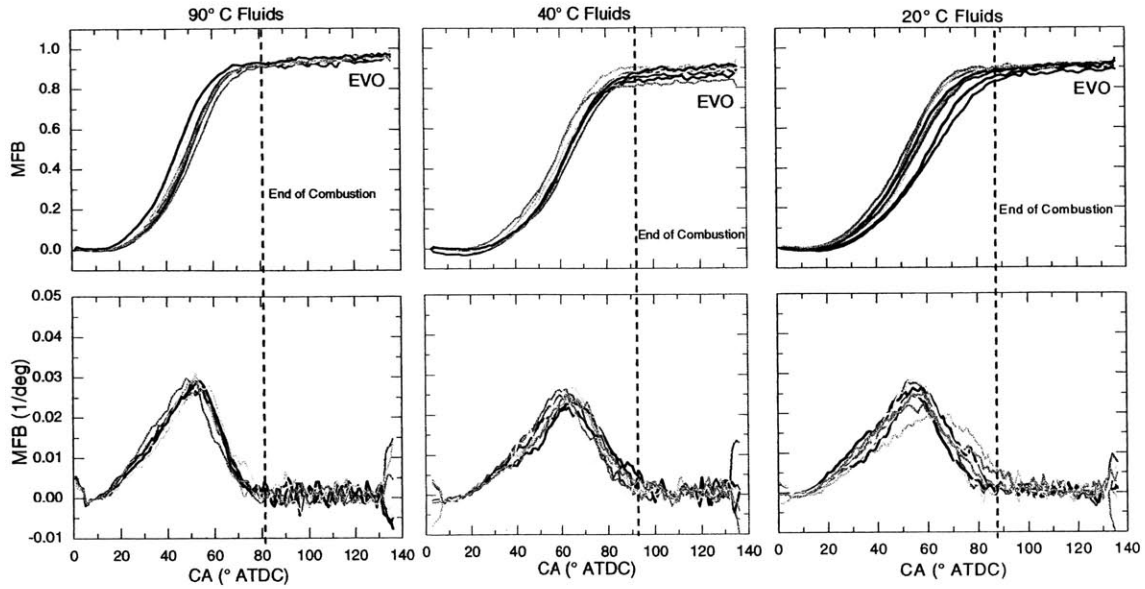

Figure C.3.1 Cumulative mass fraction burned (MFB) and instantaneous MFB rate as a function of crank angle for 90°, 40°, and 20° C fluids. Operating conditions: 3.0 bar Net-IMEP, 1500 RPM, λ = 1.0, spark timing = -1° BTDC, without charge motion (CMCP).

C.4 TIME-RESOLVED HC MEASUREMENTS: 90° C FLUIDS

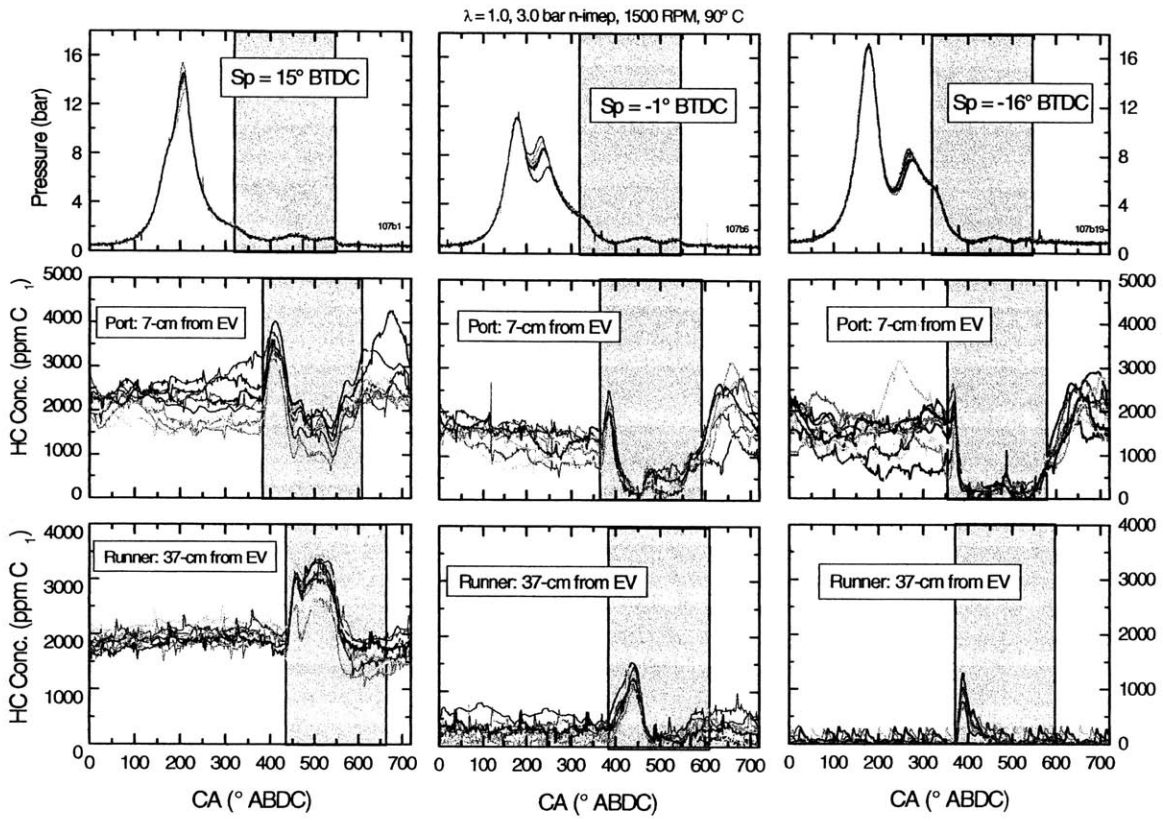

Figure C.4.1 In-cylinder pressure and exhaust port and runner time-resolved HC concentration measurements for three different spark timings (Sp = 15°, -1°, -16° BTDC) at 3.0 bar Net-IMEP, λ = 1.0, CMCP, and 90° C fluids.

C.5 HYDROCARBON MASS FLOW RATES

C.5.1 Port and Runner Emission: Spark Timing = 15° BTDC

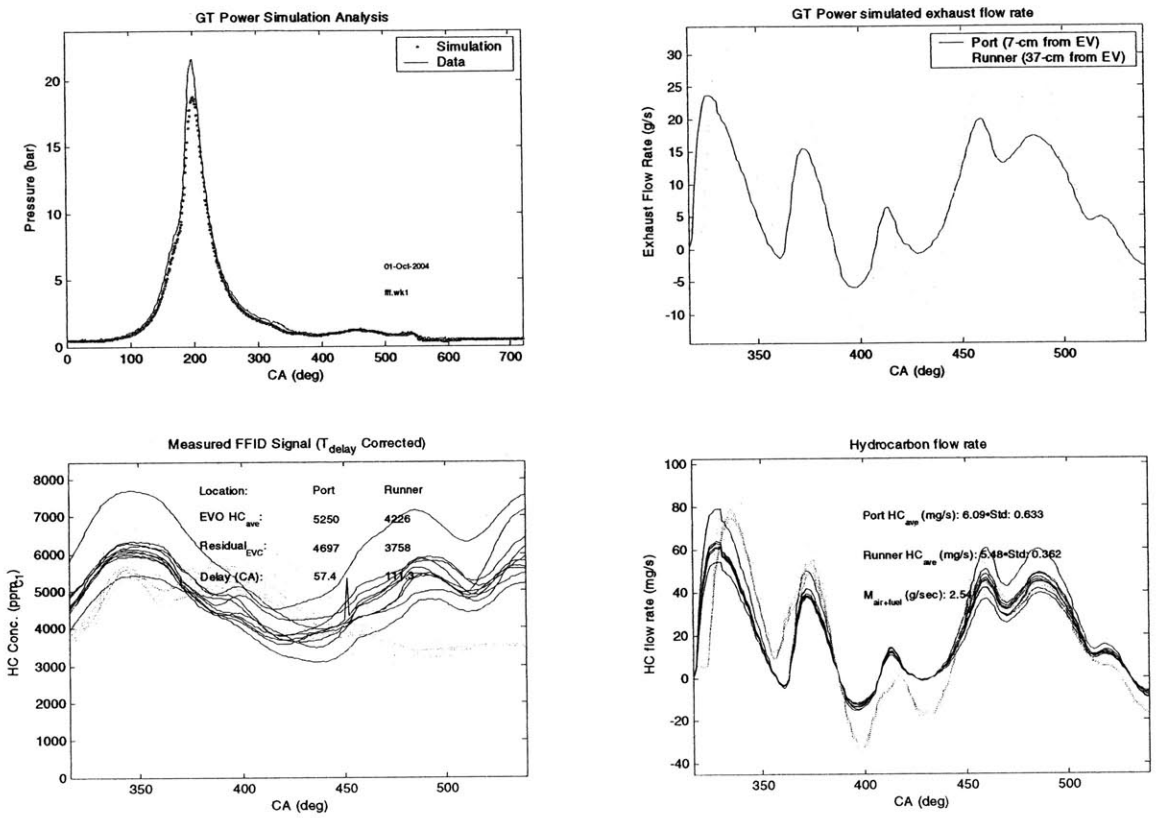

Figure C.5.1 Model results from analysis of time-resolved HC measurements. GT-Power simulation results of in-cylinder pressure (upper left) and exhaust mass flow rate at the port exit and runner.(upper right). Measured HC concentrations (lower left) and predicted HC mass flow rate (lower right). Data shown for 3.0 bar Net-IMEP, 1500 RPM., 15° BTDC spark timing, $\lambda = 1.0$, and 20° C fluids.

C.5.2 Port and Runner Emission: Spark Timing = -1° BTDC

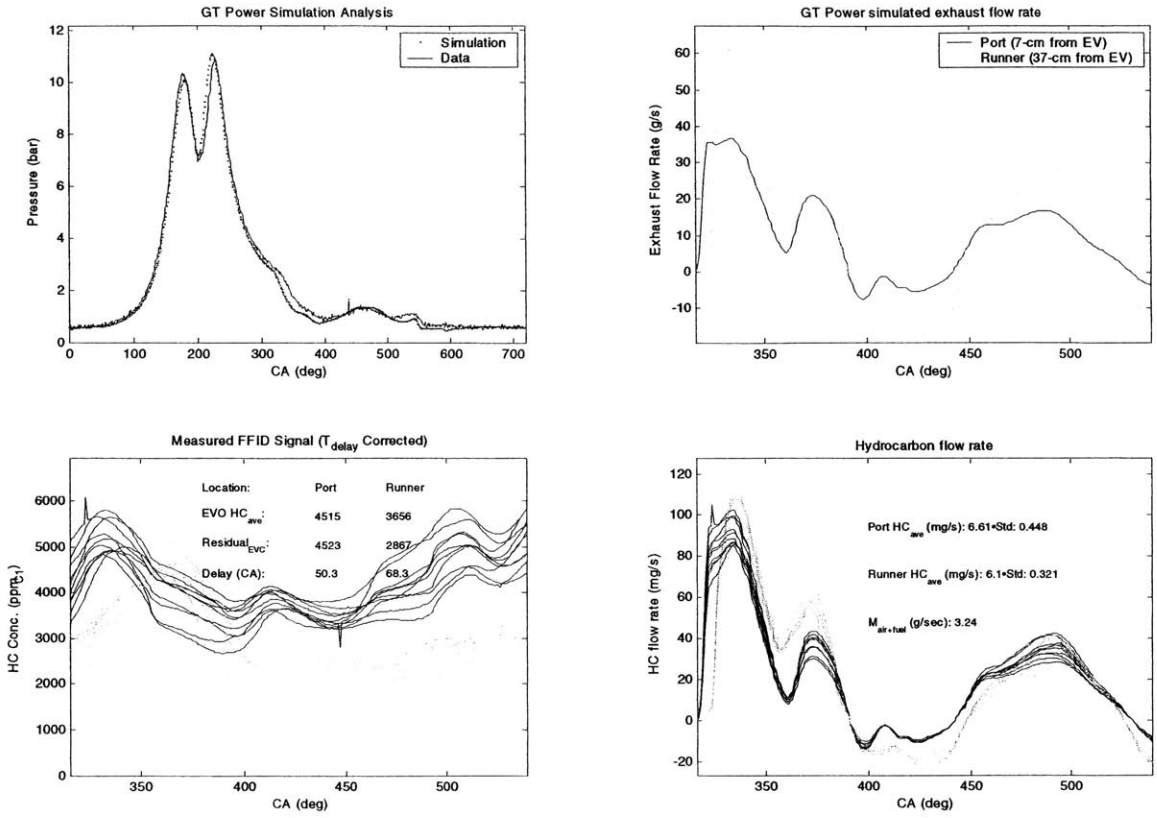

Figure C.5.2 Model results from analysis of time-resolved HC measurements. GT-Power simulation results of in-cylinder pressure (upper left) and exhaust mass flow rate at the port exit and runner.(upper right). Measured HC concentrations (lower left) and predicted HC mass flow rate (lower right). Data shown for 3.0 bar Net-IMEP, 1500 RPM., -1° BTDC spark timing, $\lambda = 1.0$, and 20° C fluids.

C.5.3 Port and Runner Emission: Spark Timing = -10° BTDC

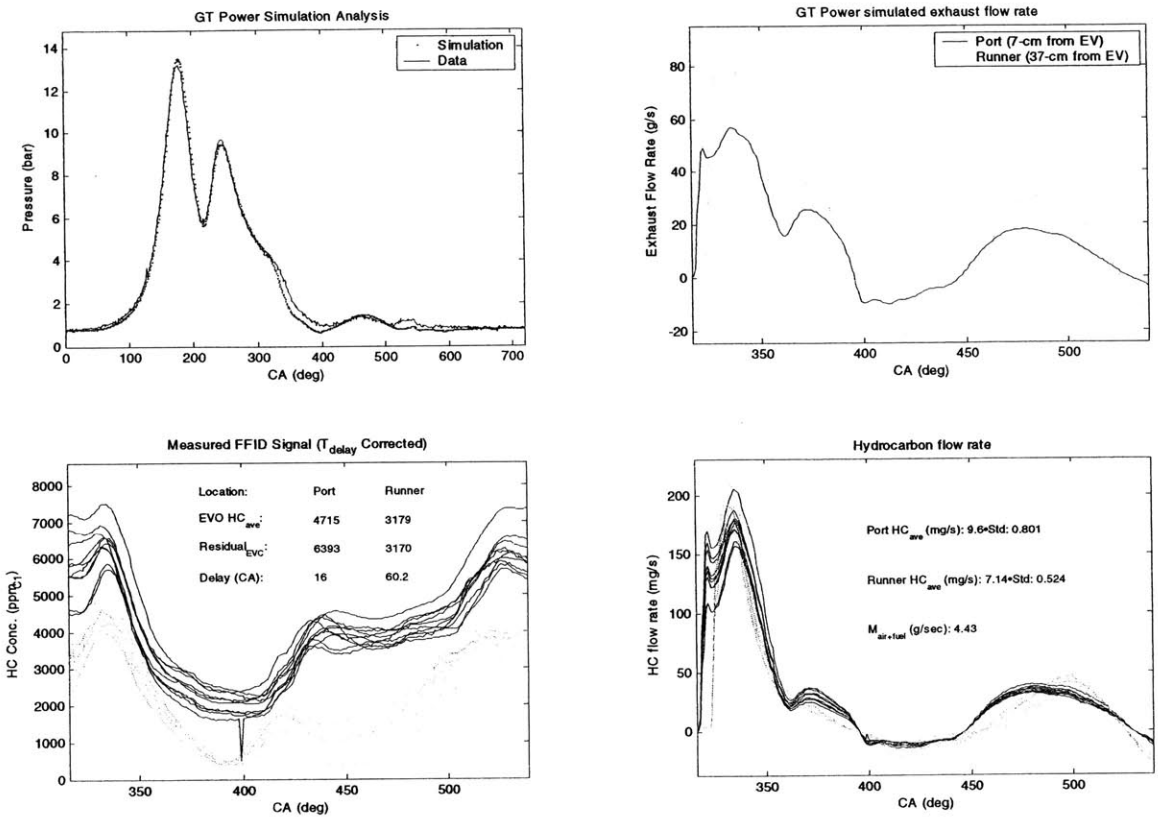

Figure C.5.3 Model results from analysis of time-resolved HC measurements. GT-Power simulation results of in-cylinder pressure (upper left) and exhaust mass flow rate at the port exit and runner.(upper right). Measured HC concentrations (lower left) and predicted HC mass flow rate (lower right). Data shown for 3.0 bar Net-IMEP, 1500 RPM., -10° BTDC spark timing, $\lambda = 1.0$, and 20° C fluids.

C.5.4 Port and Runner Emission: Spark Timing = -15° BTDC

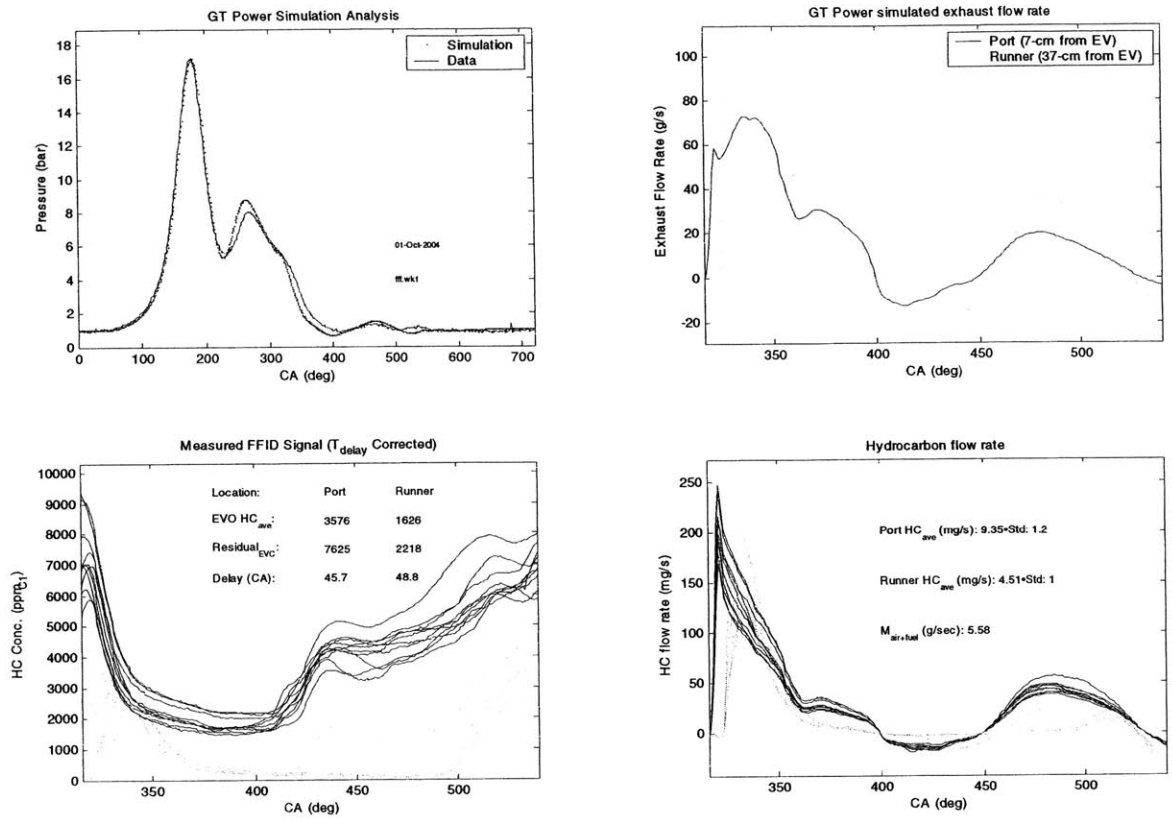

Figure C.5.4 Model results from analysis of time-resolved HC measurements. GT-Power simulation results of in-cylinder pressure (upper left) and exhaust mass flow rate at the port exit and runner.(upper right). Measured HC concentrations (lower left) and predicted HC mass flow rate (lower right). Data shown for 3.0 bar Net-IMEP, 1500 RPM., -15° BTDC spark timing, $\lambda = 1.0$, and 20° C fluids.

C.6 CYLINDER-EXIT QUENCHING

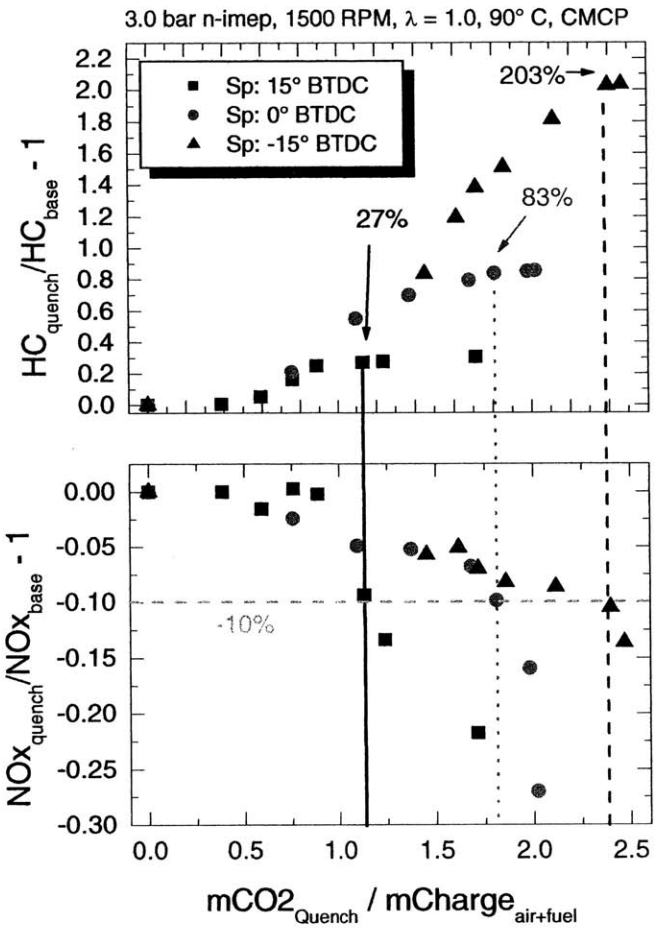

Figure C.6.1 Change in HC and NO_x emissions as a function of the ratio of mass of quench gas to mass of charge ($mCO2_{Quench}/mCharge_{air+fuel}$) for three spark timings with $\lambda = 1.0$ and 90° C fluids.

C.7 SECONDARY AIR EXPERIMENTS

C.7.1 HC Flow Rate and EGTs: Spark Timing 15° BTDC

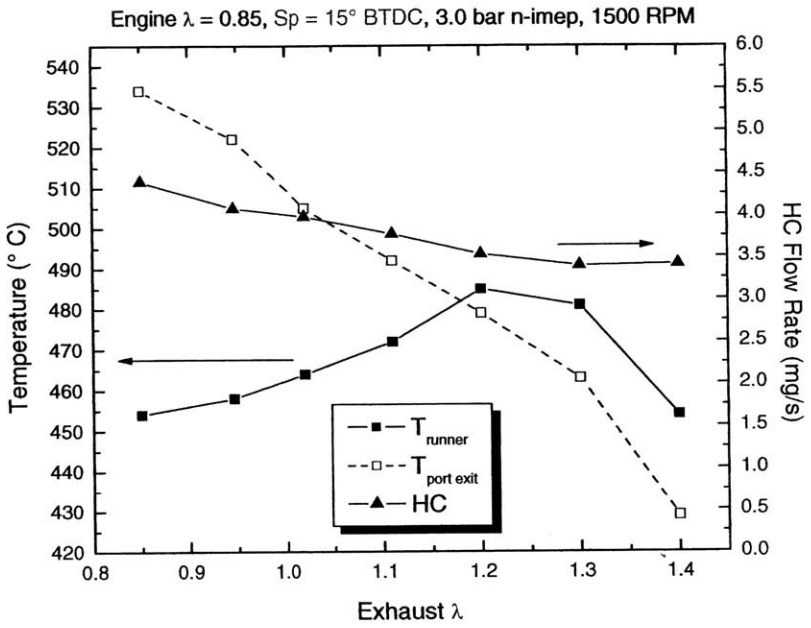

Figure C.7.1 Port exit and runner EGTs and tailpipe-out HC flow rate as a function of exhaust relative air/fuel ratio. Data shown for continuos secondary air injection at a fixed engine relative air/fuel ratio (λ_{engine} = 0.85) and 15° BTDC spark timing.

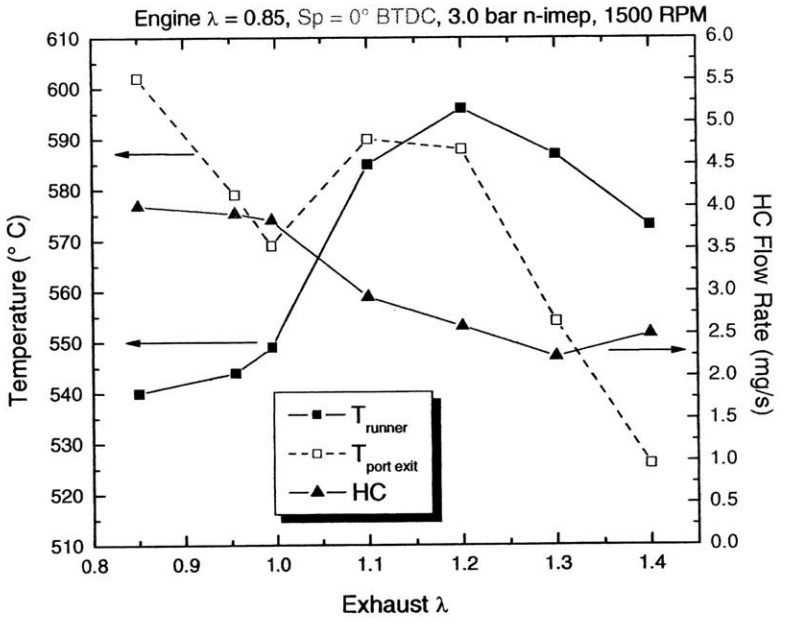

Figure C.7.2 Port exit and runner EGTs and tailpipe-out HC flow rate as a function of exhaust relative air/fuel ratio. Data shown for continuos secondary air injection at a fixed engine relative air/fuel ratio (λ_{engine} = 0.85) and 0° BTDC spark timing.

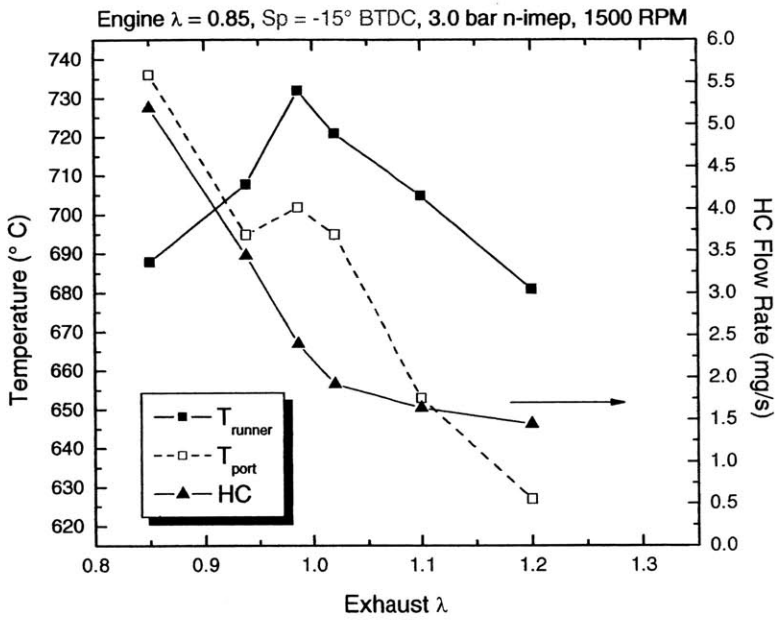

Figure C.7.3 Port exit and runner EGTs and tailpipe-out HC flow rate as a function of exhaust relative air/fuel ratio. Data shown for continuos secondary air injection at a fixed engine relative air/fuel ratio ($\lambda_{engine} = 0.85$) and -15° BTDC spark timing.

APPENDIX D

MULTI-CYLINDER STARTUP DATA: 1 TO 20 SECONDS

D.1 BASELINE CALIBRATION: 0° ($\Delta\theta_{SPARK}$ = 0°)

D.1.1 In-cylinder Pressure, RPM, MAP, Spark Timing, and Relative Air/Fuel Ratio

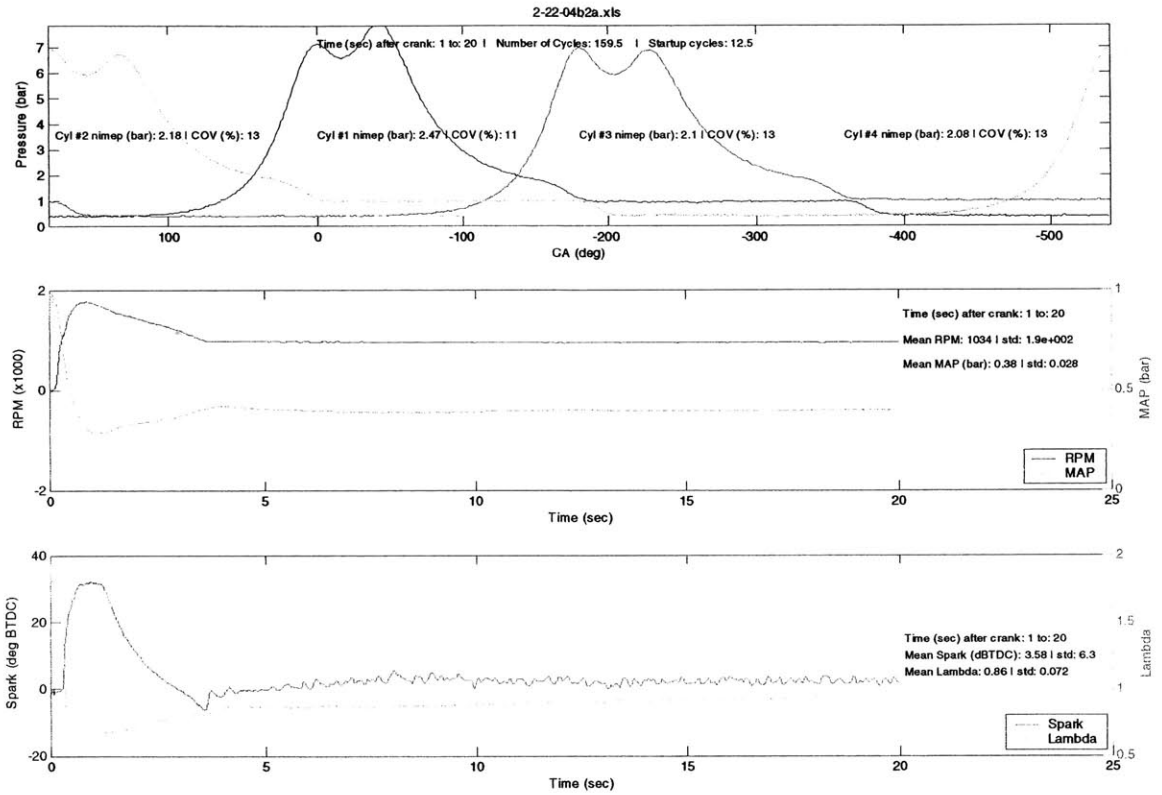

Figure D.1.1 In-cylinder pressure, RPM, MAP, spark timing, and lambda (λ) as a function of time after ambient startup. Data shown for baseline spark and fuel calibration ($\Delta\theta_{spark}$ = 0°). Calculated Net-IMEP and COV of Net-IMEP, averaged RPM, MAP, spark timing, and λ, for 1 to 20 seconds after crank.

D.1.2 Hydrocarbon Concentrations, Exhaust Gas and Component Temperatures

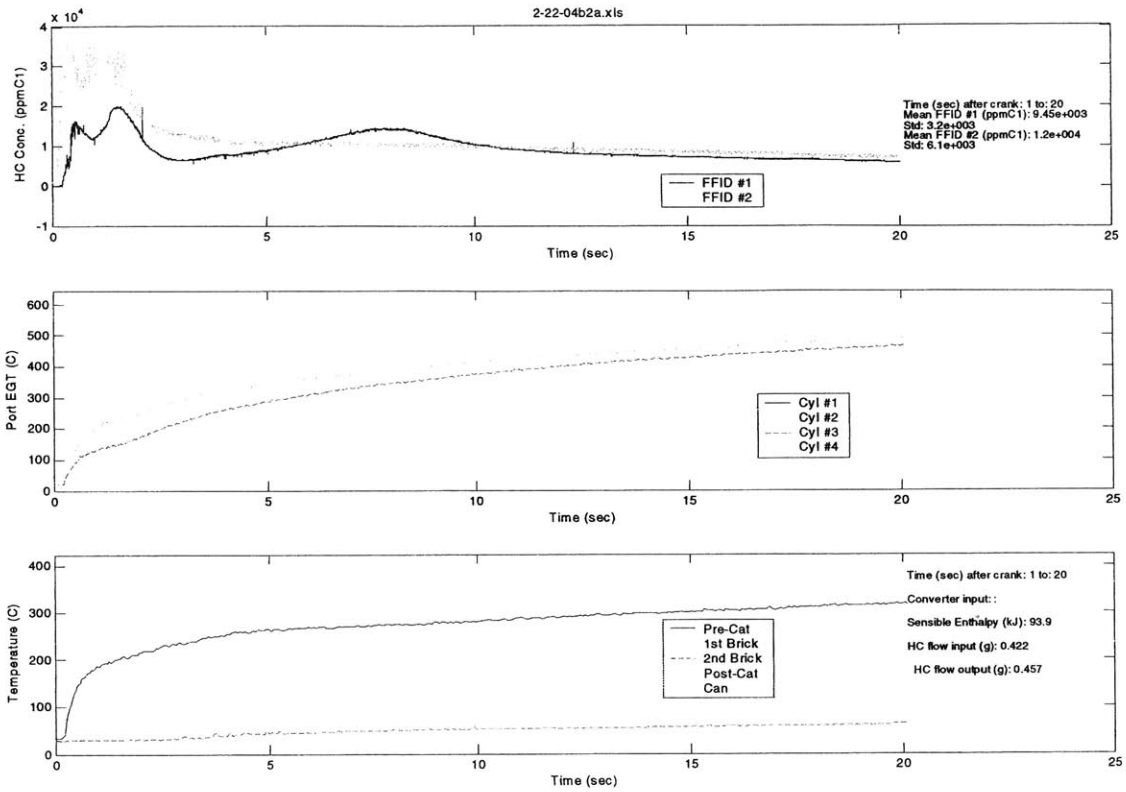

Figure D.1.2 Time-resolved port exit (FFID #1) and converter-in (FFID #2) HC concentrations, port exhaust gas temperature (EGT), and exhaust component temperatures as a function of time after ambient startup. Data shown for baseline spark and fuel calibration ($\Delta\theta_{spark}$ = 0°). Calculated sensible enthalpy and averaged HC concentrations for 1 to 20 seconds after crank.

D.2 SPARK TIMING MODIFICATION: -5° ($\Delta\theta_{SPARK}$ = -5°)

D.2.1 In-cylinder Pressure, RPM, MAP, Spark Timing, and Relative Air/Fuel Ratio

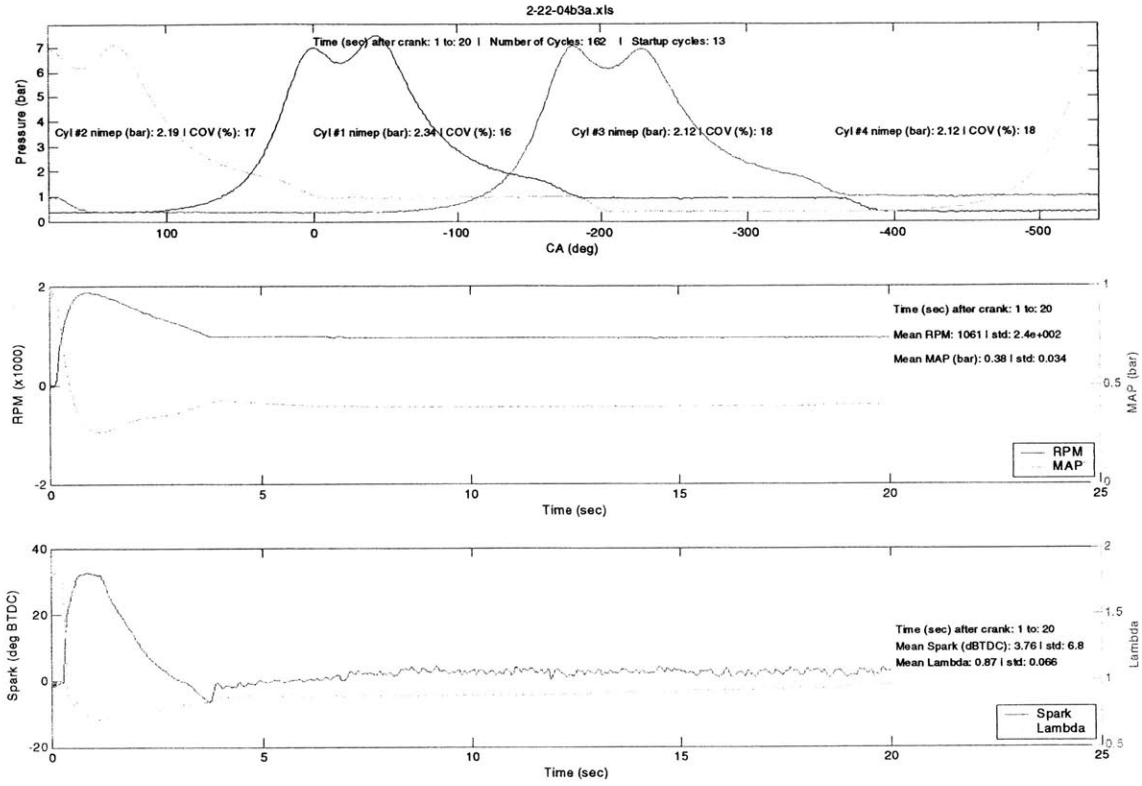

Figure D.2.1 In-cylinder pressure, RPM, MAP, spark timing, and lambda (λ) as a function of time after ambient startup. Data shown for -5° spark timing modification ($\Delta\theta_{spark}$ = -5°). Calculated Net-IMEP and COV of Net-IMEP, averaged RPM, MAP, spark timing, and λ, for 1 to 20 seconds after crank.

D.2.2 Hydrocarbon Concentrations, Exhaust Gas and Component Temperatures

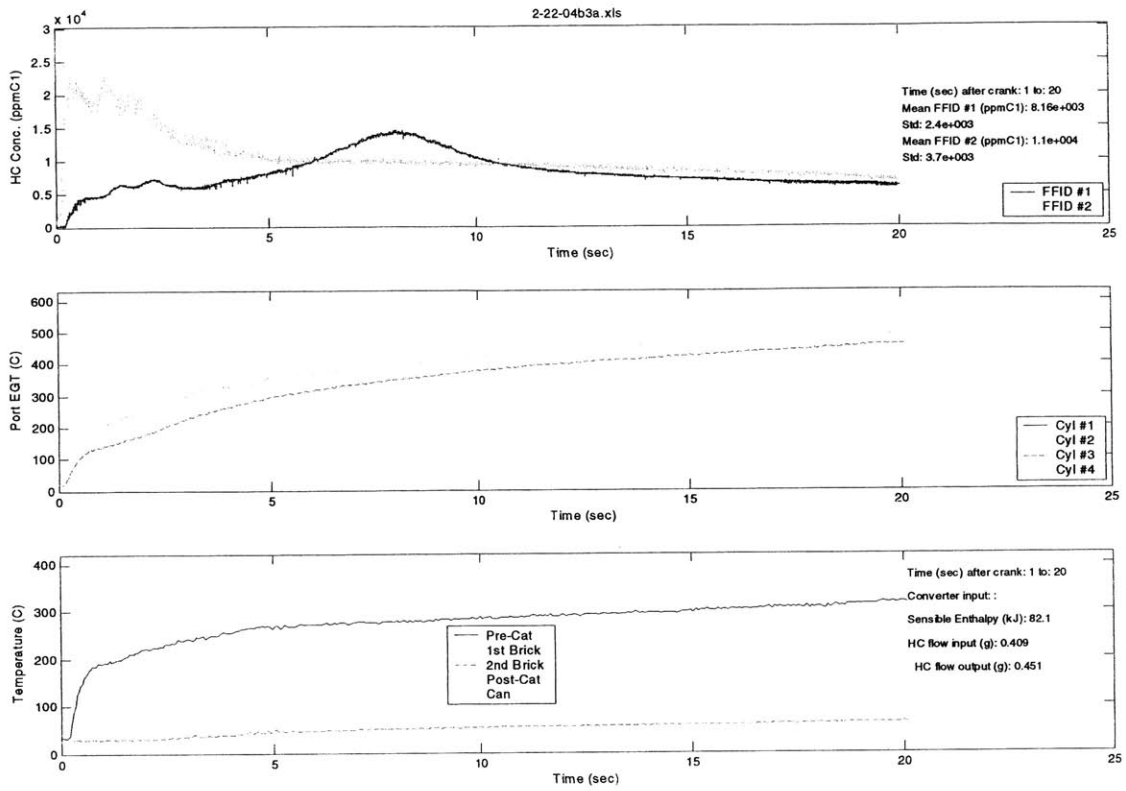

Figure D.2.2 Time-resolved port exit (FFID #1) and converter-in (FFID #2) HC concentrations, port exhaust gas temperature (EGT), and exhaust component temperatures as a function of time after ambient startup. Data shown -5° spark modification ($\Delta\theta_{spark}$ = -5°). Calculated sensible enthalpy and averaged HC concentrations for 1 to 20 seconds after crank.

D.3 SPARK TIMING MODIFICATION: -10° ($\Delta\theta_{SPARK}$ = -10°)

D.3.1 In-cylinder Pressure, RPM, MAP, Spark Timing, and Relative Air/Fuel Ratio

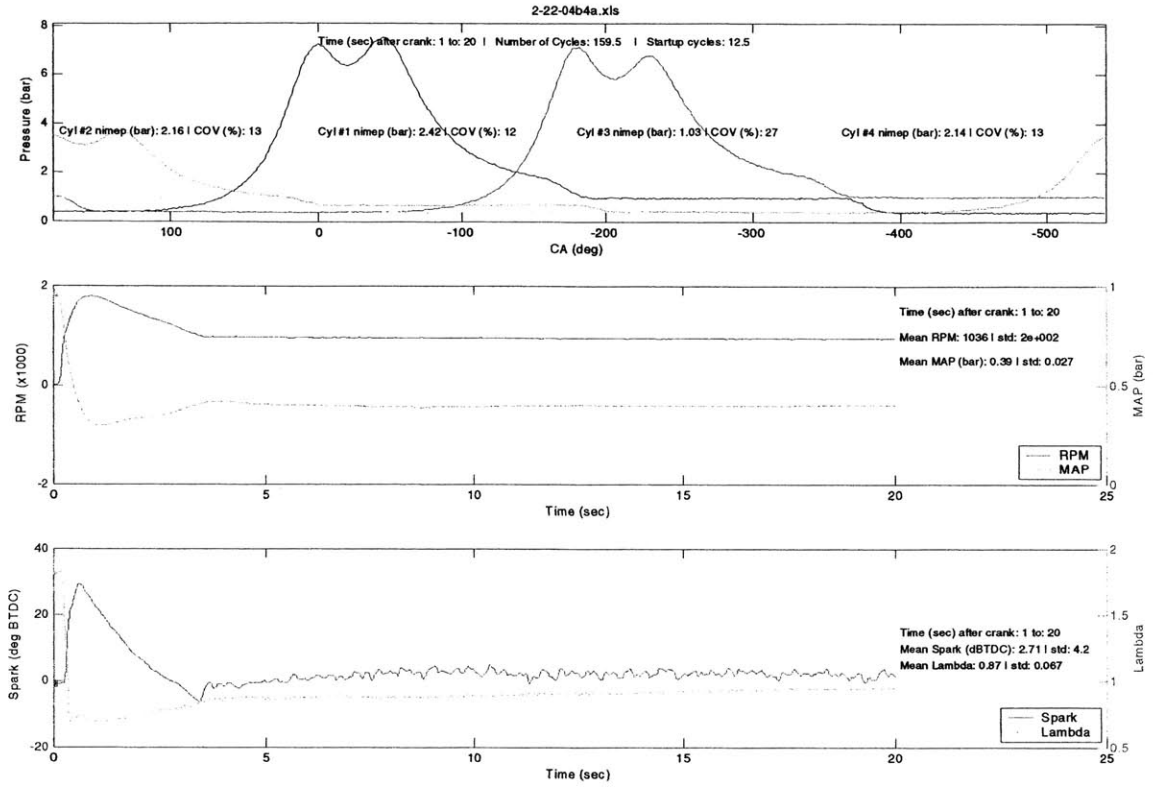

Figure D.3.1 In-cylinder pressure, RPM, MAP, spark timing, and lambda (λ) as a function of time after ambient startup. Data shown for -10° spark timing modification ($\Delta\theta_{spark}$ = -10°). Calculated Net-IMEP and COV of Net-IMEP, averaged RPM, MAP, spark timing, and λ, for 1 to 20 seconds after crank.

D.3.2 Hydrocarbon Concentrations, Exhaust Gas and Component Temperatures

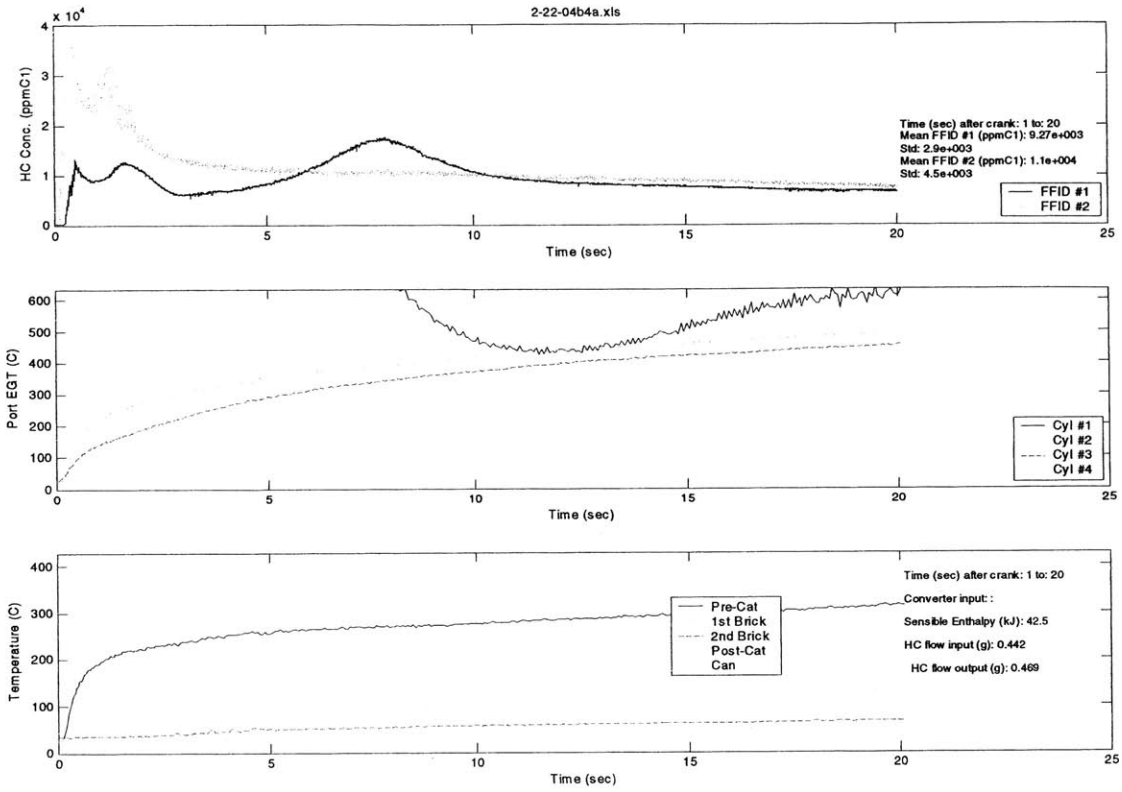

Figure D.3.2 Time-resolved port exit (FFID #1) and converter-in (FFID #2) HC concentrations, port exhaust gas temperature (EGT), and exhaust component temperatures as a function of time after ambient startup. Data shown -10° spark modification ($\Delta\theta_{spark}$ = -10°). Calculated sensible enthalpy and averaged HC concentrations for 1 to 20 seconds after crank.

D.4 SPARK TIMING MODIFICATION: -15° ($\Delta\theta_{SPARK}$ = -15°)

D.4.1 In-cylinder Pressure, RPM, MAP, Spark Timing, and Relative Air/Fuel Ratio

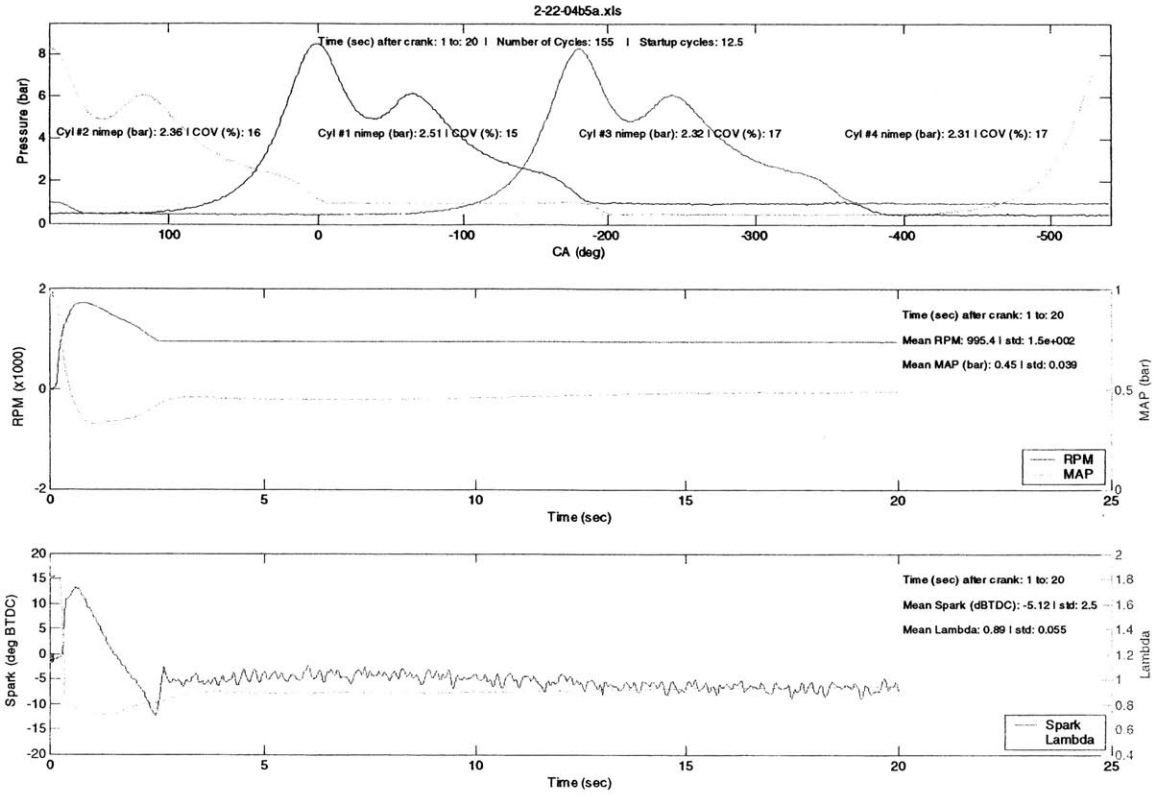

Figure D.4.1 In-cylinder pressure, RPM, MAP, spark timing, and lambda (λ) as a function of time after ambient startup. Data shown for -15° spark timing modification ($\Delta\theta_{spark}$ = -15°). Calculated Net-IMEP and COV of Net-IMEP, averaged RPM, MAP, spark timing, and λ, for 1 to 20 seconds after crank.

D.4.2 Hydrocarbon Concentrations, Exhaust Gas and Component Temperatures

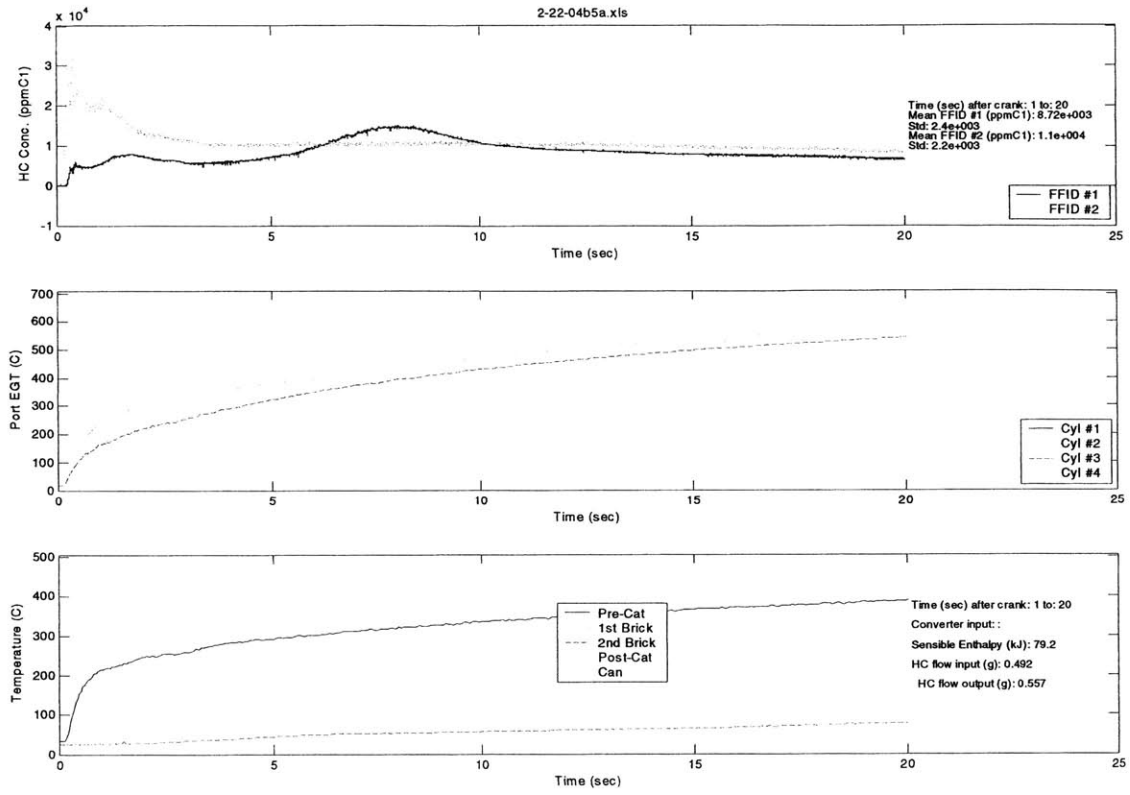

Figure D.4.2 Time-resolved port exit (FFID #1) and converter-in (FFID #2) HC concentrations, port exhaust gas temperature (EGT), and exhaust component temperatures as a function of time after ambient startup. Data shown -15° spark modification ($\Delta\theta_{spark}$ = -15°). Calculated sensible enthalpy and averaged HC concentrations for 1 to 20 seconds after crank.

APPENDIX E

ENGINE SIMULATION

E.1 SINGLE-CYLINDER ENGINE

E.1.1 Valve Lift and Discharge Coefficients

Volvo Valve Data

Intake: 31 mm dia				Exhaust: 28 mm dia				Intake: 31 mm dia		Exhaust: 28 mm dia	
CA	Lift (mm)	CA	Lift (mm)	CA	Lift (mm)	CA	Lift (mm)	Lift/Diameter	Cd	L/D	Cd
360	0	480	8.45	100	0	220	8.43	0	0.684	0	0.706
362	0.25	482	8.43	102	0.3	222	8.41	0.023	0.729	0.0106	0.733
364	0.4	484	8.41	104	0.7	224	8.39	0.067	0.752	0.025	0.697
366	0.55	486	8.39	106	0.95	226	8.35	0.101	0.778	0.051	0.668
368	0.7	488	8.36	108	1.03	228	8.32	0.134	0.745	0.077	0.688
370	0.86	490	8.32	110	1.19	230	8.29	0.168	0.699	0.102	0.708
372	1.02	492	8.29	112	1.36	232	8.23	0.201	0.655	0.128	0.701
374	1.19	494	8.23	114	1.53	234	8.17	0.235	0.615	0.154	0.704
376	1.36	496	8.17	116	1.71	236	8.1	0.268	0.552	0.205	0.687
378	1.53	498	8.1	118	1.89	238	8.1	0.302	0.519	0.231	0.636
380	1.71	500	8.02	120	1.98	240	8.02	0.336	0.479	0.257	0.589
382	1.88	502	7.94	122	2.07	242	7.94				
384	2.07	504	7.89	124	2.25	244	7.85				
386	2.25	506	7.8	126	2.43	246	7.75				
388	2.43	508	7.75	128	2.51	248	7.65				
390	2.61	510	7.65	130	2.8	250	7.54				
392	2.8	512	7.54	132	2.99	252	7.42				
394	2.99	514	7.42	134	3.17	254	7.3				
396	3.17	516	7.3	136	3.36	256	7.17				
398	3.36	518	7.17	138	3.55	258	7.04				
400	3.55	520	7.04	140	3.74	260	6.9				
402	3.74	522	6.9	142	3.93	262	6.75				
404	3.93	524	6.75	144	4.11	264	6.61				
406	4.11	526	6.61	146	4.3	266	6.46				
408	4.3	528	6.46	148	4.48	268	6.3				
410	4.48	530	6.3	150	4.67	270	6.14				
412	4.67	532	6.14	152	4.85	272	5.99				
414	4.85	534	5.99	154	5.03	274	5.81				
416	5.03	536	5.81	156	5.21	276	5.65				
418	5.21	538	5.65	158	5.39	278	5.47				
420	5.39	540	5.47	160	5.56	280	5.3				
422	5.56	542	5.3	162	5.73	282	5.12				
424	5.73	544	5.12	164	5.9	284	4.94				
426	5.9	546	4.94	166	6.06	286	4.76				
428	6.06	548	4.76	168	6.22	288	4.58				
430	6.22	550	4.58	170	6.38	290	4.39				
432	6.38	552	4.39	172	6.46	292	4.21				
434	6.54	554	4.21	174	6.61	294	4.02				
436	6.66	556	4.11	176	6.76	296	3.93				
438	6.83	558	3.93	178	6.9	298	3.84				
440	6.97	560	3.74	180	7.04	300	3.46				
442	7.11	562	3.55	182	7.17	302	3.27				
444	7.24	564	3.36	184	7.3	304	3.08				
446	7.36	566	3.17	186	7.42	306	2.89				
448	7.48	568	2.99	188	7.54	308	2.71				
450	7.56	570	2.8	190	7.65	310	2.52				
452	7.7	572	2.61	192	7.75	312	2.34				
454	7.8	574	2.43	194	7.85	314	2.15				
456	7.88	576	2.25	196	7.94	316	2.07				
458	7.98	578	2.07	198	8.02	318	1.99				
460	8.06	580	1.99	200	8.1	320	1.71				
462	8.13	582	1.71	202	8.17	322	1.53				
464	8.23	584	1.53	204	8.23	324	1.36				
466	8.28	586	1.36	206	8.32	326	1.19				
468	8.32	588	1.19	208	8.35	328	1.03				
470	8.36	590	1.03	210	8.39	330	0.86				
472	8.39	592	0.86	212	8.41	332	0.7				
474	8.41	594	0.7	214	8.43	334	0.55				
476	8.43	596	0.55	216	8.45	336	0.4				
478	8.45	598	0.3	218	8.45	338	0.25				
						340	0				

E.2 MULTI-CYLINDER ENGINE

E.2.1 GT-Power Engine Simulation

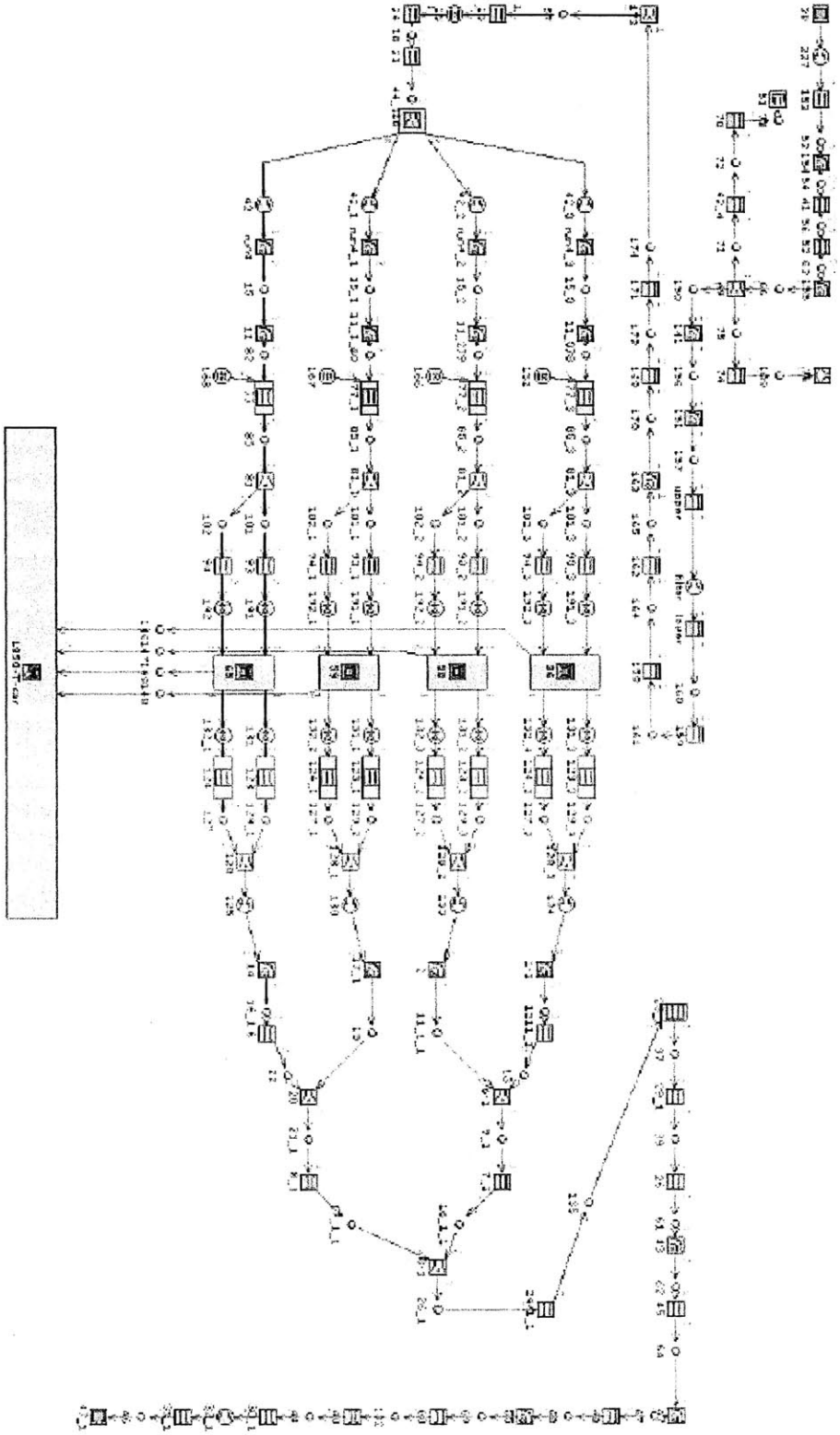

E.2.2 Valve Lift and Discharge Coefficients

Ecotec Valve Data

Intake: 35.2 mm dia				Exhaust: 30.2 mm dia				Intake: 35.2 mm dia		Exhaust: 30.2 mm dia	
CA	Lift (mm)	CA	Lift (mm)	CA	Lift (mm)	CA	Lift (mm)	Lift/Diameter	Cd	L/D	Cd
173	0.001513	229	10.0324	97.5	0.000863	152.5	9.95959	0.028	0.075	0.033	0.062595
174	0.007223	240	10.0152	98.5	0.005585	153.5	9.91550	0.057	0.15	0.066	0.168230
175	0.016995	241	9.99739	99.5	0.014426	154.5	9.86175	0.085	0.224	0.099	0.283430
176	0.03093	242	9.96990	70.5	0.027266	155.5	9.79818	0.114	0.297	0.132	0.379372
177	0.047477	243	9.92718	71.5	0.043527	156.5	9.72462	0.142	0.368	0.166	0.466599
178	0.066831	244	9.87937	72.5	0.061824	157.5	9.64223	0.17	0.436	0.199	0.484030
179	0.089662	245	9.82235	73.5	0.080757	158.5	9.54866	0.199	0.484	0.232	0.502582
180	0.131497	246	9.75524	74.5	0.122751	159.5	9.44830	0.227	0.513	0.265	0.542885
181	0.163285	247	9.68159	75.5	0.173683	160.5	9.33713	0.256	0.54	0.298	0.576333
182	0.200239	248	9.59971	76.5	0.241064	161.5	9.21079	0.284	0.556	0.331	0.623000
183	0.332763	249	9.50594	77.5	0.329667	162.5	9.08723	0.313	0.57	0.364	0.625351
184	0.431057	250	9.40518	78.5	0.438173	163.5	8.94862	0.341	0.576	0.397	0.627594
185	0.54531	251	9.29591	79.5	0.569366	164.5	8.80060				
186	0.675559	252	9.17899	80.5	0.724338	165.5	8.64436				
187	0.82209	253	9.05239	81.5	0.903378	166.5	8.47921				
188	0.985039	254	8.91739	82.5	1.109330	167.5	8.30535				
189	1.16447	255	8.77325	83.5	1.331710	168.5	8.12293				
190	1.366*4	256	8.62092	84.5	1.577000	169.5	7.93228				
191	1.5716	257	8.45974	85.5	1.841670	170.5	7.73340				
192	1.79607	258	8.29016	86.5	2.121150	171.5	7.52645				
193	2.03822	259	8.11237	87.5	2.412240	172.5	7.31161				
194	2.29064	260	7.92547	88.5	2.713960	173.5	7.08914				
195	2.55377	261	7.73036	89.5	3.021100	174.5	6.85912				
196	2.82572	262	7.52693	90.5	3.331640	175.5	6.62176				
197	3.10467	263	7.31501	91.5	3.643350	176.5	6.37747				
198	3.38881	264	7.09457	92.5	3.954140	177.5	6.12666				
199	3.67625	265	6.86599	93.5	4.262420	178.5	5.86982				
200	3.96502	266	6.62897	94.5	4.566070	179.5	5.60753				
201	4.2534	267	6.38373	95.5	4.860050	180.5	5.34054				
202	4.54013	268	6.13019	96.5	5.156430	181.5	5.06943				
203	4.8238	269	5.86858	97.5	5.449130	182.5	4.79508				
204	5.10211	270	5.59925	98.5	5.725740	183.5	4.51822				
205	5.37759	271	5.32238	99.5	5.997660	184.5	4.23984				
206	5.64819	272	5.03818	*00.5	6.262290	185.5	3.96053				
207	5.90835	273	4.74791	*01.5	6.518080	186.5	3.68146				
208	6.16367	274	4.45129	*02.5	6.767000	187.5	3.40376				
209	6.41155	275	4.15027	*03.5	7.007000	188.5	3.12885				
210	6.65219	276	3.84554	*04.5	7.238660	189.5	2.85828				
211	6.88469	277	3.53872	*05.5	7.461970	170.5	2.59378				
212	7.11042	278	3.23141	*06.5	7.676170	171.5	2.33720				
213	7.32739	279	2.92591	*07.5	7.881020	172.5	2.09029				
214	7.53644	280	2.62455	*08.5	8.076000	173.5	1.85455				
215	7.73757	281	2.33011	*09.5	8.260670	174.5	1.63159				
216	7.93064	282	2.04575	*10.5	8.445860	175.5	1.42264				
217	8.11551	283	1.77454	*11.5	8.615710	176.5	1.22874				
218	8.29224	284	1.51947	*12.5	8.770250	177.5	1.05046				
219	8.46069	285	1.28320	*13.5	8.907030	178.5	0.88809				
220	8.62079	286	1.06791	*14.5	9.026640	179.5	0.74136				
221	8.77257	287	0.875478	*15.5	9.201970	180.5	0.61036				
222	8.916	288	0.706999	*16.5	9.324800	181.5	0.49529				
223	9.05084	289	0.562528	*17.5	9.436130	182.5	0.39569				
224	9.17724	290	0.441693	*18.5	9.541840	183.5	0.31237				
225	9.29511	291	0.342798	*19.5	9.636800	184.5	0.24464				
226	9.40429	292	0.264413	*20.5	9.720000	185.5	0.192*9				
227	9.50489	293	0.205004	*21.5	9.7945*0	186.5	0.15358				
228	9.59695	294	0.16187	*22.5	9.856030	187.5	0.12603				
229	9.68039	295	0.131534	*23.5	9.913680	188.5	0.1055*				
230	9.7549	296	0.110148	*24.5	9.956630	180.5	0.08082				
231	9.82079	297	0.092034	*25.5	9.993430	190.5	0.06825				
232	9.87795	298	0.073592	*26.5	*0.018400	191.5	0.04068				
233	9.92643	299	0.055540	*27.5	*0.033200	192.5	0.03151				
234	9.96607	300	0.037855	*28.5	*0.038300	193.5	0.01675				
235	9.99689	30*	0.021550	*29.5	*0.033200	194.5	0.0065*				
236	10.015	302	0.009997	*30.5	*0.018600	195.5	0.00115				
237	10.0223	303	0.002803	*31.5	9.994000						
238	10.0307	304	4.40E-05								

APPENDIX F

EXHAUST OXIDATION MODEL

F.1 INITIAL MODEL INPUT CONDITIONS

Mass of Hydrocarbons (F.1.1)

$$m_{HC} = \int_{EVO}^{EVC} \dot{m}_{HC}\, d\theta$$

Enthalpic Average Temperature (F.1.2)

$$\overline{T_{bulk}} = \frac{\int_{EVO}^{EVC} \dot{m} C_p T_g d\theta}{\int_{EVO}^{EVC} \dot{m} C_p d\theta}$$

Average Bulk Velocity (F.1.3)

$$\overline{V_{bulk}} = \frac{\int_{EVO}^{EVC} \dot{m} V d\theta}{\int_{EVO}^{EVC} \dot{m}\, d\theta}$$

Exhaust Gas Mass (F.1.4)

$$m_{exhaust} = \int_{EVO}^{EVC} \dot{m}_{exhaust}\, d\theta$$

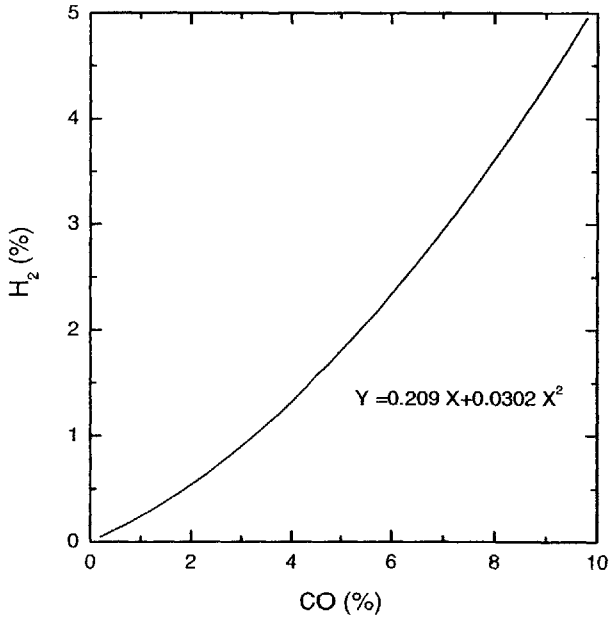

Figure F.1.1 Exhaust gas hydrogen (H_2) concentration as a function of CO concentration [14].

F.2 HEAT TRANSFER MODEL

Prandtl Number (Pr) (F.2.1)

$$\mathrm{Pr} = \frac{\upsilon}{k / \rho Cp} = 0.65$$

Nusselt Number (Nu) (F.2.2)

$$Nu_D = \frac{h_D D}{k}$$

Reynolds Number (Re) (F.2.3)

$$\mathrm{Re}_D = \frac{\rho V D}{\mu}$$

where:

Re_D	*Reynolds number*
ρ	*density*
V	*velocity*
D	*diameter*
Cp	*specific heat at constant pressure*
μ	*dynamic viscosity*
Nu_D	*Nusselt number*
k	*thermal conductivity*
h	*convective heat transfer coefficient*
w_i	*mass reaction rate*
ν	*kinematic viscosity*

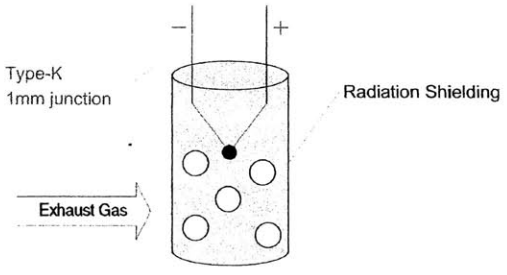

Figure F.2.1 Schematic of type-k thermocouple and radiation shielding for measuring exhaust gas temperature.

Energy Equation for Thermocouple Sensor (F.2.4)

$$m_{TC} C \frac{dT_{TC}}{dt} = hA\left(T_{fluid} - T_{TC}\right) + \varepsilon\sigma A\left(T_{fluid}{}^4 - T_{TC}{}^4\right)$$

where:

m	*thermocouple mass*
C	*thermocouple specific heat*
h	*convective heat transfer coefficient*
A	*thermocouple heat transfer area*
ε	*emissivity*
σ	*Stefan-Boltzman constant (5.67e-8 W/m^2K^4)*
Ts	*thermocouple temperature*
Tf	*fluid temperature*
Tw	*wall temperature*

Convective Heat Transfer from Gas to Inner Pipe Layer (F.2.5)

$$q_{gp} = h\pi d\Delta x\left(T_g - T_p\right)$$

where:

q_{gp}	*heat flux from gas to inner wall*
h	*convective heat transfer coefficient*
T_g	*gas temperature*
T_p	*inner wall temperature*

Heat Conduction from Inner Pipe Layer to Outer Pipe Layer (F.2.6)

$$q_{io} = \frac{2\pi k}{\ln(d_2 / d_1)}(T_{ip} - T_{op})$$

where:

q_{io}	*heat flux from inner to outer wall*
k	*convective heat transfer coefficient*
d_2	*outer wall diameter*
d_1	*inner wall diameter*
T_{ip}	*inner wall temperature*
T_{op}	*outer wall temperature*

F.3 CHEMKIN SOFTWARE

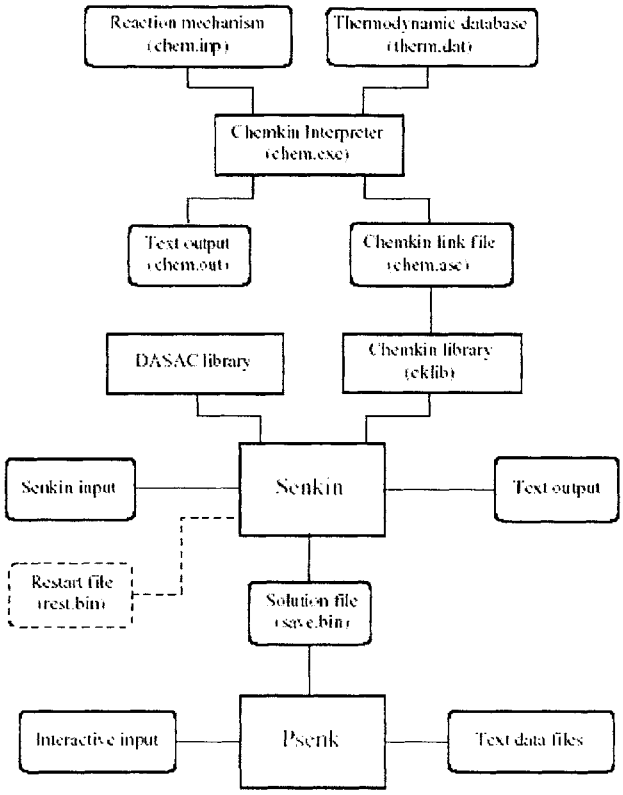

Figure F.3.1 SENKIN sub-model flowchart overview.

Energy Equation (F.3.1)

$$c_v \frac{dT}{dt} + p\frac{dv}{dt} + v\sum_{k=1}^{K} e_k \dot{\omega}_k W_k = 0$$

where:

Cv	*specific heat at constant volume*
T	*temperature of mixture*
t	*time*
p	*pressure*
v	*specific volume*
e_k	*internal energy of k^{th} species*
ω	*molar production rate of k^{th} species*
W_k	*molecular weight of k^{th} species*

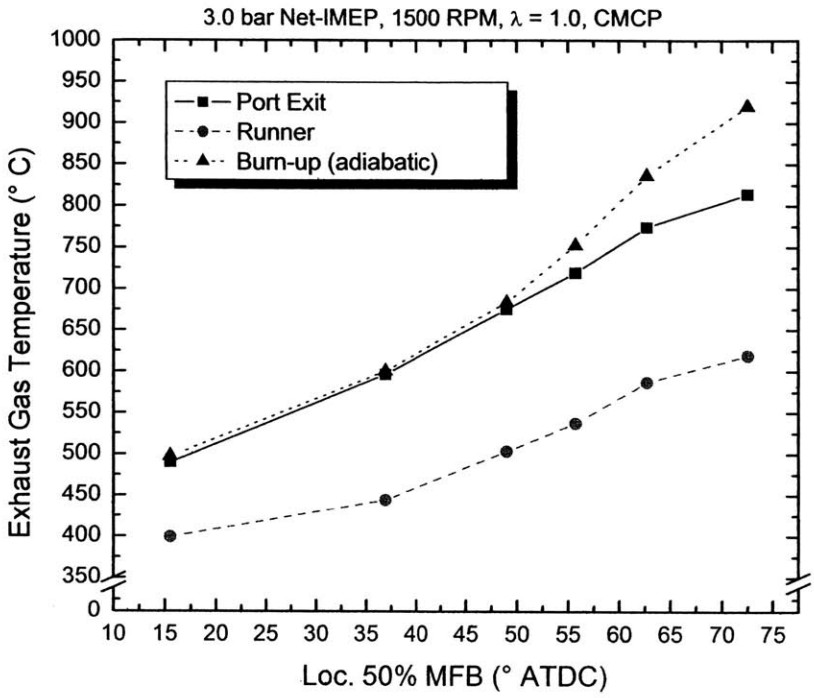

Figure F.3.2 Port, runner, and calculated burn-up exhaust gas temperature as a function of combustion phasing (location of 50% MFB). Burn-up temperatures are based upon complete oxidation of HC without the effects of heat transfer in the runner. Data shown for 3.0 bar Net-IMEP, 1500 RPM, 20° fluids, λ = 1.0 with charge motion (CMCP).

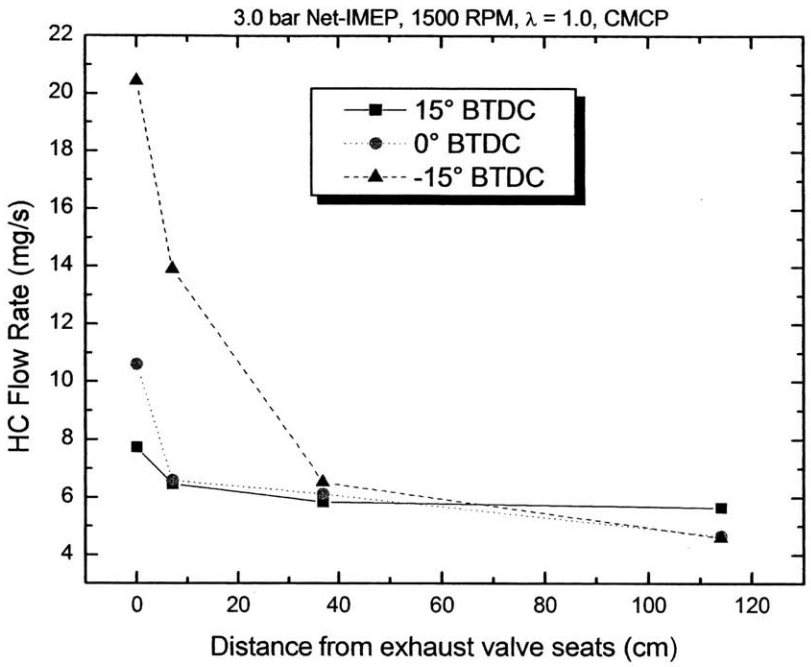

Figure F.3.3 Hydrocarbon mass flow rate as a function of distance from exhaust valve seats for three spark timings. Data shown for 3.0 bar Net-IMEP, 1500 RPM, $\lambda = 1.0$, with charge motion (CMCP).

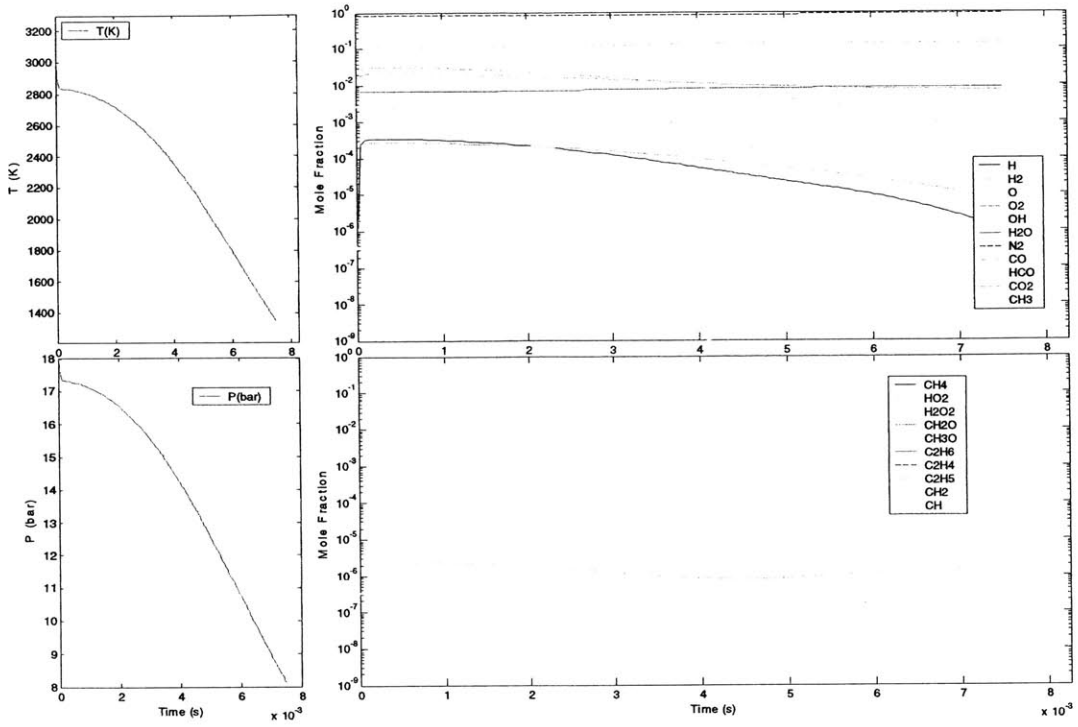

Figure F.3.4 Super-equilibrium exhaust gas radical concentrations. Volume-time dependent Senkin calculation from end of combustion to exhaust valve opening.

F.4 SINGLE-CYLINDER ENGINE

F.4.1 Spark Timing = 15° BTDC and $\lambda = 1.0$

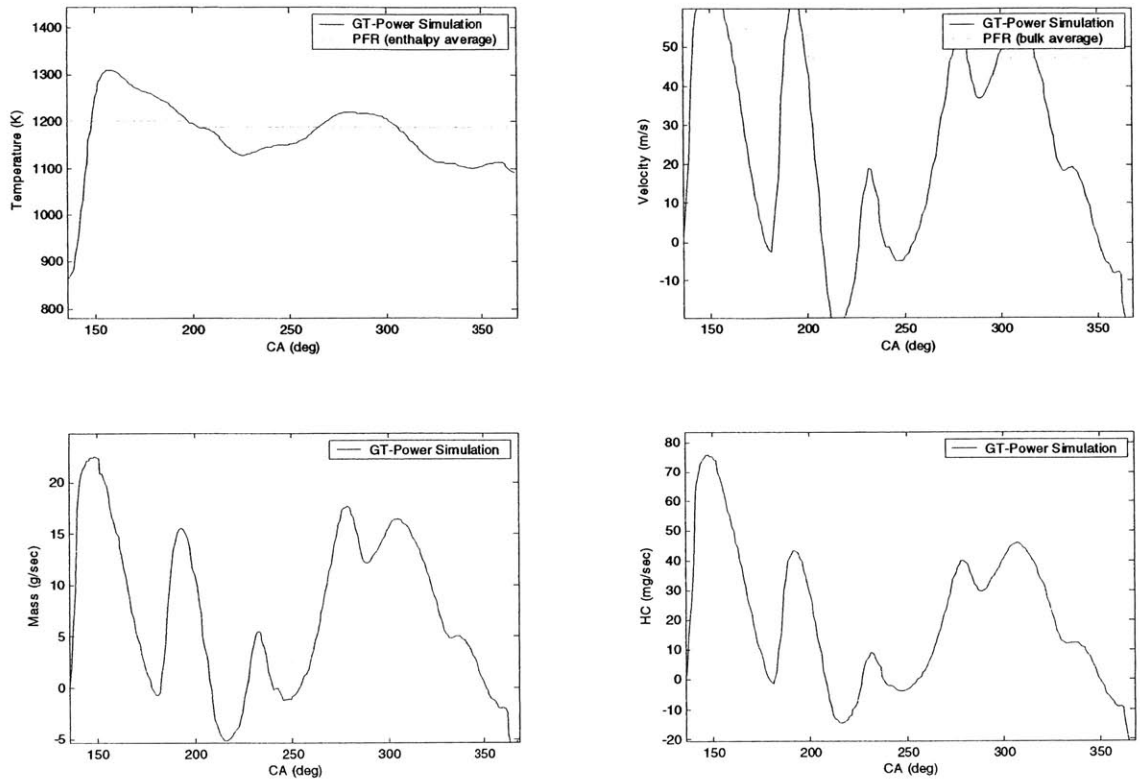

Figure F.4.1 Time histories of cylinder-exit temperature, velocity, mass flow, and hydrocarbon mass emissions as a function of crank angle. Data shown for $\lambda = 1.0$ and spark timing = 15° BTDC.

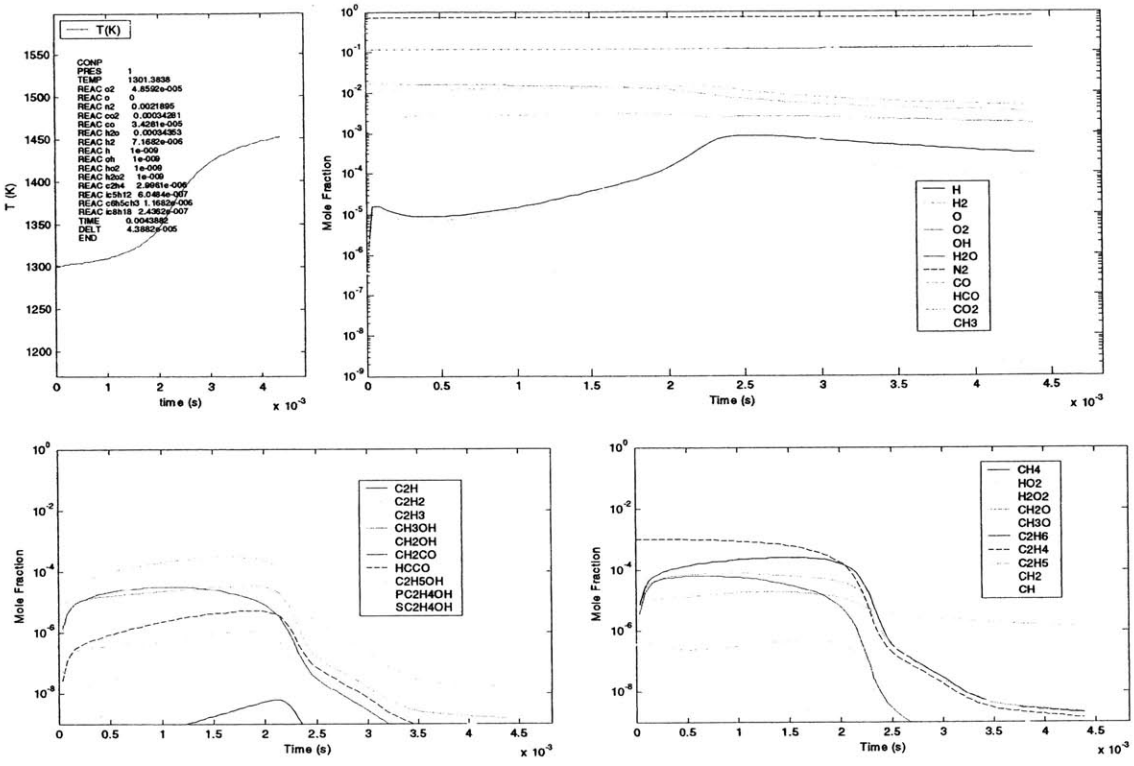

Figure F.4.2 Mass element temperature and exhaust gas mole fraction histories as a function of time for a highly diluted reactive mixture. Data shown for $\lambda = 1.0$ and spark timing = 15° BTDC.

F.4.2 : Spark Timing = 0° BTDC and λ = 1.0

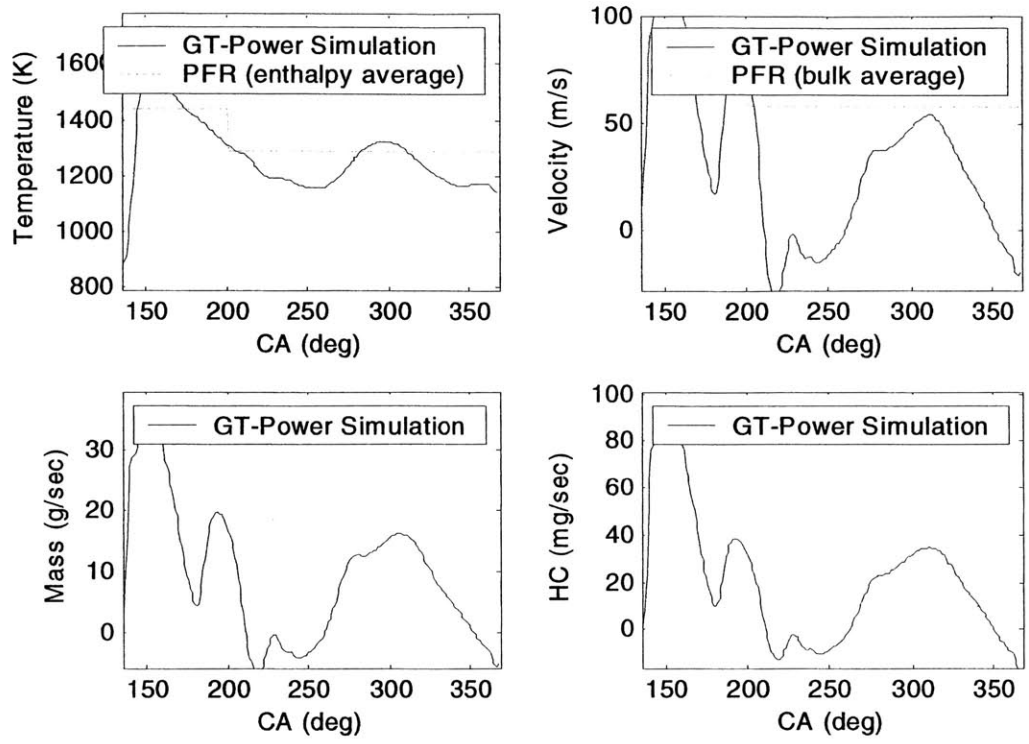

Figure F.4.3 Time histories of cylinder-exit temperature, velocity, mass flow, and hydrocarbon mass emissions as a function of crank angle. Data shown for λ = 1.0 and spark timing = 0° BTDC.

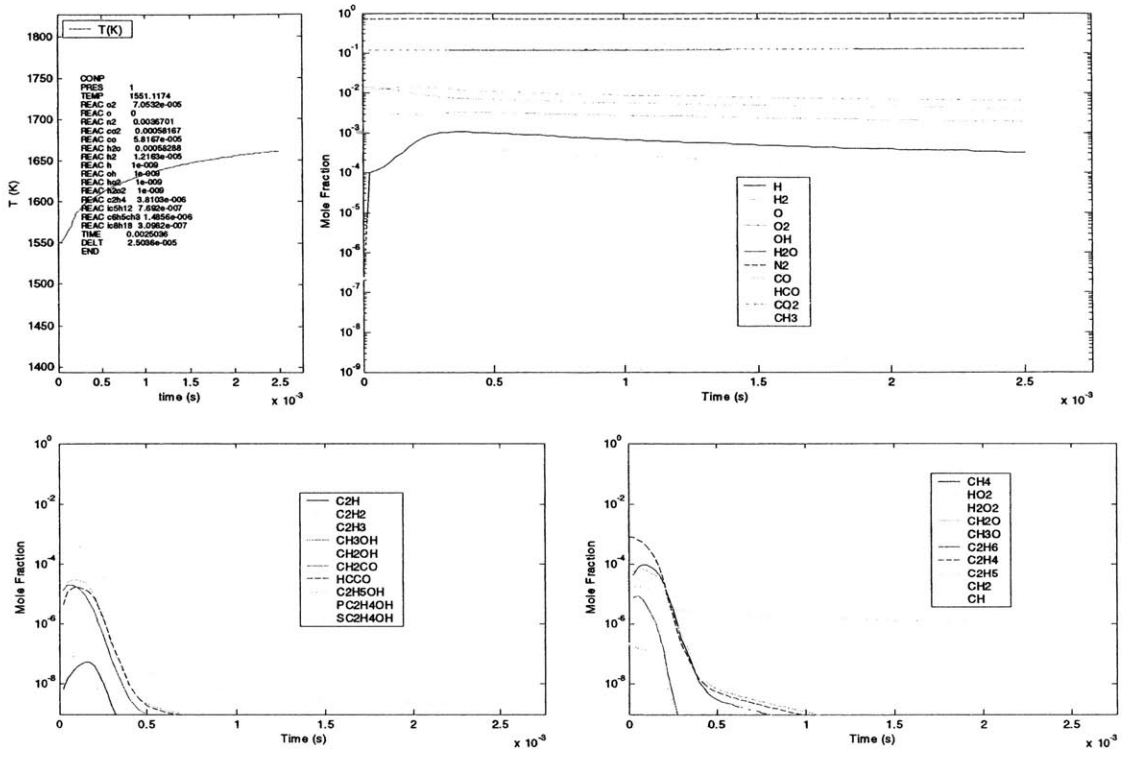

Figure F.4.4 Mass element temperature and exhaust gas mole fraction histories as a function of time for a highly diluted reactive mixture. Data shown for $\lambda = 1.0$ and spark timing = 0° BTDC.

F.4.3 Spark Timing = -15° BTDC and λ = 1.0

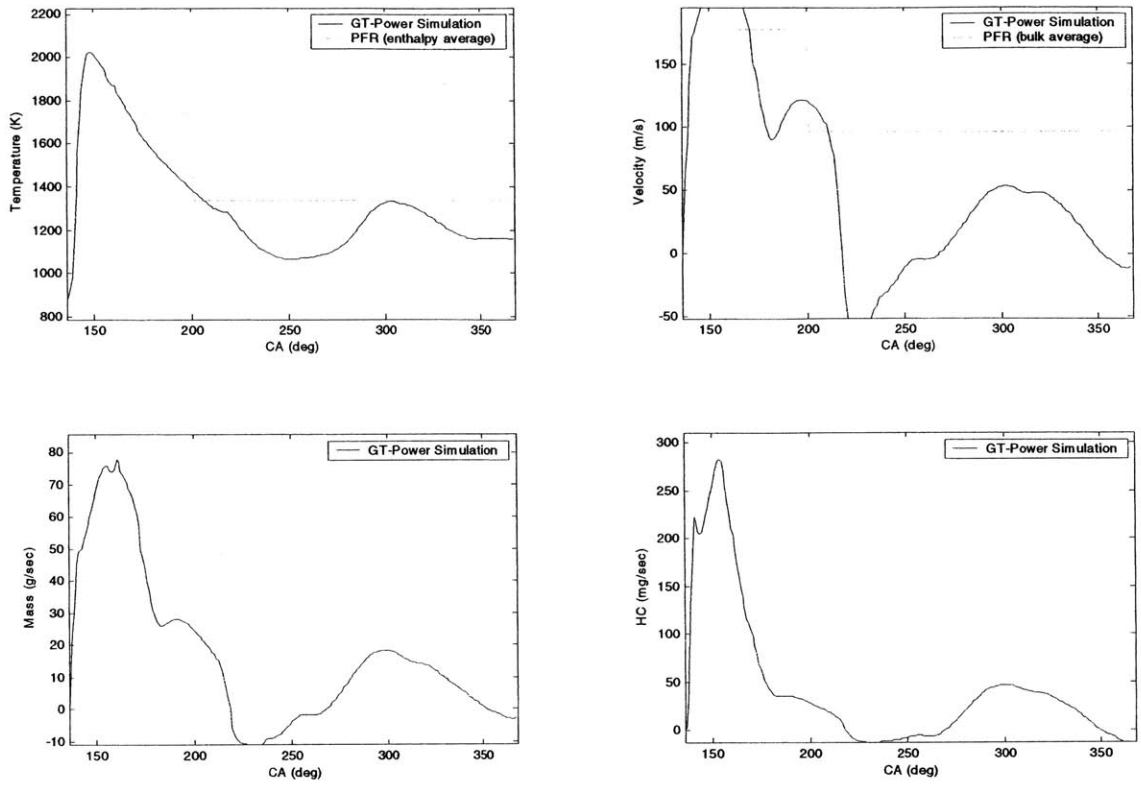

Figure F.4.5 Time histories of cylinder-exit temperature, velocity, mass flow, and hydrocarbon mass emissions as a function of crank angle. Data shown for λ = 1.0 and spark timing = -15° BTDC.

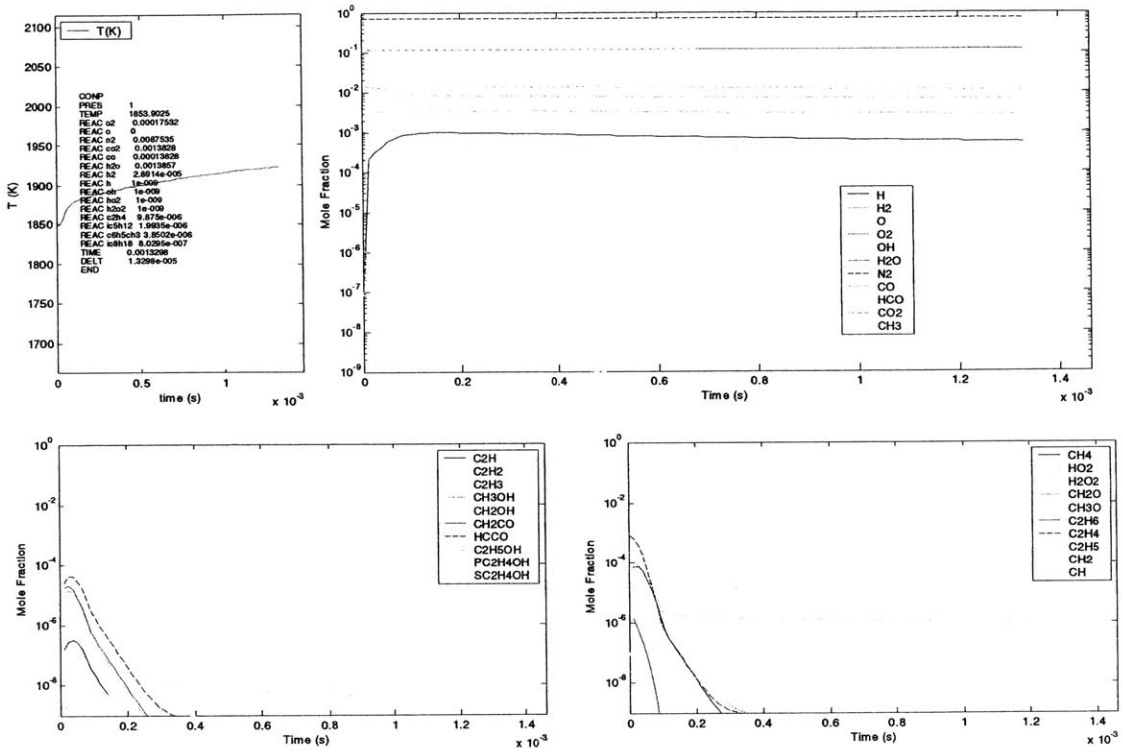

Figure F.4.6 Mass element temperature and exhaust gas mole fraction histories as a function of time for a highly diluted reactive mixture. Data shown for $\lambda = 1.0$ and spark timing = -15° BTDC.